The metabolism of the developing brain:

How large neutral amino acids modulate perinatal neuronal excitability and survival

by

Lisa S. Knaus

May, 2023

A thesis submitted to the
Graduate School of the
Institute of Science and Technology Austria
in partial fulfillment of the requirements
for the degree of
Doctor of Philosophy

Committee in charge:
Mario De Bono, Chair
Gaia Novarino
Johann Danzl
Laura Cancedda

Institute of
Science and
Technology
Austria

The thesis of Lisa S. Knaus, titled *The metabolism of the developing brain: How large neutral amino acids modulate perinatal neuronal excitability and survival*, is approved by:

Supervisor: Gaia Novarino, ISTA, Klosterneuburg, Austria

Signature: ___________________________________

Committee Member: Johann Danzl, ISTA, Klosterneuburg, Austria

Signature: ___________________________________

Committee Member: Laura Cancedda, IIT, Genova, Italy

Signature: ___________________________________

Defense Chair: Mario De Bono, ISTA, Klosterneuburg, Austria

Signature: ___________________________________

signed page is on file

ISTA Thesis, ISSN: 2663-337X

I hereby declare that this thesis is my own work and that it does not contain other people's work without this being so stated; this thesis does not contain my previous work without this being stated, and the bibliography contains all the literature that I used in writing the dissertation.

I declare that this is a true copy of my thesis, including any final revisions, as approved by my thesis committee, and that this thesis has not been submitted for a higher degree to any other university or institution.

I certify that any republication of materials presented in this thesis has been approved by the relevant publishers and co-authors.

Signature: ______________________

Lisa S. Knaus

May, 2023

signed page is on file

Abstract

Within the human body, the brain exhibits the highest rate of energy consumption amongst all organs, with the majority of generated ATP being utilized to sustain neuronal activity. Therefore, the metabolism of the mature cerebral cortex is geared towards preserving metabolic homeostasis whilst generating significant amounts of energy. This requires a precise interplay between diverse metabolic pathways, spanning from a tissue-wide scale to the level of individual neurons. Disturbances to this delicate metabolic equilibrium, such as those resulting from maternal malnutrition or mutations affecting metabolic enzymes, often result in neuropathological variants of neurodevelopment. For instance, mutations in *SLC7A5*, a transporter of metabolically essential large neutral amino acids (LNAAs), have been associated with autism and microcephaly. However, despite recent progress in the field, the extent of metabolic restructuring that occurs within the developing brain and the corresponding alterations in nutrient demands during various critical periods remain largely unknown.

To investigate this, we performed metabolomic profiling of the murine cerebral cortex to characterize the metabolic state of the forebrain at different developmental stages. We found that the developing cortex undergoes substantial metabolic reprogramming, with specific sets of metabolites displaying stage-specific changes. According to our observations, we determined a distinct temporal period in postnatal development during which the cortex displays heightened reliance on LNAAs. Hence, using a conditional knock-out mouse model, we deleted *Slc7a5* in neural cells, allowing us to monitor the impact of a perturbed neuronal metabolic state across multiple developmental stages of corticogenesis. We found that manipulating the levels of essential LNAAs in cortical neurons *in vivo* affects one particular perinatal developmental period critical for cortical network refinement. Abnormally low intracellular LNAA levels result in cell-autonomous alterations in neuronal lipid metabolism, excitability, and survival during this particular time window. Although most of the effects of Slc7a5 deletion on neuronal physiology are transient, derailment of these processes during this brief but crucial window leads to long-term circuit dysfunction in mice.

In conclusion, out data indicate that the cerebral cortex undergoes significant metabolic reorganization during development. This process involves the intricate integration of multiple metabolic pathways to ensure optimal neuronal function throughout different developmental stages. Our findings offer a paradigm for understanding how neurons synchronize the expression of nutrient-related genes with their activity to allow proper brain maturation. Further, our results demonstrate that disruptions in these precisely calibrated metabolic processes during critical periods of brain development may result in neuropathological outcomes in mice and in humans.

Acknowledgments

The work presented in this thesis was performed at the Institute of Science and Technology Austria (ISTA) and was financially supported by an European Union's Horizon 2020 research and innovation program (ERC) grant and the Austrian Science Fund (FWF) to Gaia Novarino (715508 and DK W1232-B24). I am very thankful to the Doctoral Program "Molecular Drug Targetes" (MolTag) for offering me the financial support that allowed me to perform essential experiments for the progress of my project and to participate at international conferences and courses.

I am very grateful to my supervisor, Gaia Novarino, for supporting me during the last 5 years. She taught me how to think in a critical way and how to see the bigger picture. I am very thankful that she trusted me when I told her that there is something more hidden in the depths of my project. Further, I would like express my gratitude to my external and internal thesis committee members, Laura Cancedda and Johann Danzl, for taking the time to evaluate my PhD thesis.

I want to acknowledge all the scientists that have contributed to this work. Specifically, I would like to say thank you to all the collaborators on this project, to Bernadette Basilico, Maria Gerykova Bujalkova, Mateja Smogavec, Lena Schwarz, Sarah Gorkiewicz, Nicole Amberg, Florian Pauler, Christian Knittl-Frank, Marianna Tassinari, Nuno Maulide, Thomas Rülicke, Jörg Menche and Simon Hippenmeyer. Special thanks go to Daniel Malzl, without him this project would have not become what it is now. In addition, I would like to thank the ISTA Proteomics Core Facility, the Electron Microscopy Facility and the Imaging and Optics Facility for the data analysis and technical support. Further, I would like to acknowledge the VBC and EMBL Metabolomics Facilities for lipidomics and metabolomics mass spectrometry data acquisition and analysis. Many thanks to the team of the ISTA Preclinical Facility, especially Sabina Deixler, Angela Stichelberger, Sophie Knoll, and Michael Schunn for their great support over the years.

I am very grateful for all the the wonderful colleagues I had the chance to work with during my time at ISTA. Thanks for all the brainstorming sessions, the great input and teamwork over the last 5 years. Especially, I would like to thank Anna and Viktor for the great technical support. Special thanks go to my colleagues Jasmin, Barbara,

Gintare and Lena, who became friends over the years. Thanks for the endless support, pep talks and fun moments in- and outside of the lab.

Last but not least, I want to thank my family, my friends and especially my partner Christoph. I dedicate this work to you. You are my safety net. Without you, I would not be where I am right now. Thank you for your limitless support, your love, the many hours of listening, making me smile and for reminding me that there is something else out there than lab work. Thank you for being there.

Lisa

Vienna, May 2023

About the author

Lisa S. Knaus obtained her BSc in Biology from the Leopold-Franzens University in Innsbruck in 2014. In 2017, she received her Master's degree in Developmental and Cell Biology from the same institution. While conducting research for her Master thesis at the Department for Neuroscience at the Medical University of Innsbruck under the supervision of Prof. Georg Dechant, she focused on the *in vitro* differentiation of human stem cells into peripheral sensory neurons. This project sparked her interest in neuroscience. In the same year, she started an internship in the lab of Prof. Gaia Novarino at IST Austria, and later affiliated with the same group. In 2019 she became a full member of the FWF-funded doctoral program "Molecular Drug Targets" (MolTag) in Vienna. During her PhD studies, she focused on understanding the role of large neutral amino acids in brain development. Her work resulted in a first-author publication in *Cell* in 2023. Lisa presented her research at national and international conferences and has earned the best poster award at the ECNP Workshop for Early Career Scientists in Nice, France in 2019.

List Publications

1. **Lisa S. Knaus**, Bernadette Basilico, Daniel Malzl, Maria Gerykova Bujalkova, Mateja Smogavec, Lena A. Schwarz, Sarah Gorkiewicz, Nicole Amberg, Florian M. Pauler, Christian Knittl-Frank, Marianna Tassinari, Nuno Maulide, Thomas Rülicke, Jörg Menche, Simon Hippenmeyer and Gaia Novarino (2023): Large neutral amino acid levels tune perinatal neuronal excitability and survival. *Cell* 186, 1950–1967
April 27, 2023*;* doi: https://doi.org/10.1016/j.cell.2023.02.037

Table of Contents

List of Figures

List of Supplementary Figures

List of Supplementary Tables

List of Abbreviations

AA	Amino acid
AC	Acylcarnitine
ADHD	Attention-deficit hyperactivity disorder
ADP	Adenosine-diphospate
AIS	Axon initial segment
α-KG	alpha-Ketoglutarate
AMPK	5' adenosine monophosphate-activated protein kinase
AP	Action potential

ASD	Autism spectrum disorder
ATP	Adenosine-triphosphate
BCAA	Branched-chain amino acid
BCAT1	Branched Chain Amino Acid Transaminase 1
BCAT2	Branched Chain Amino Acid Transaminase 2
BBB	Blood brain barrier
BCKDH	Branched-chain ketoacid dehydrogenase
BCKDK	Branched-chain ketoacid dehydrogenase kinase
BSA	Bovine serum albumin
C1	Carbon 1
C2	Carbon 2
C3	Carbon 3
CAT	Catalase
CNS	Central nervous system
CNV	Copy number variation
CoA	Coenzyme A
CP	Cortical plate
CPT1	Carnitine palmitoyltransferase 1
CPT2	Carnitine palmitoyltransferase 2
DHA	Docosahexaenoic acid
DNA	Deoxyribonucleic acid
EAA	Essential amino acid
ER	Endoplasmic reticulum
ETC	Electron transport chain

FADH2	Flavin adenine dinucleotide
FA	Fatty acid
FASD	Fetal alcohol spectrum disorder
FDR	False discovery rate
GABA	γ-Aminobutyric acid
GDP	Giant depolarizing potential
GFP	Green fluorescent protein
GO	Gene ontology
GPL	Glyerophospholipids
GS	Glutamine synthase
GTP	Guanosine triphosphate
GW	Gestational week
HC	Head circumference
HAT	Heteromeric amino acid transporter
HMG-CoA	3-hydroxy-3-methylglutaryl coenzyme A
His	Histidine
HPLC	High-performance liquid chromatography
ID	Intellectual disability
Ile	Isoleucine
IP	Immuno-precipitation
IPC	Intermediate progenitor
ISI	Inter-spike interval
KEGG	Kyoto Encyclopedia of Genes and Genomes
KO	Knock-out

LAT1	Large neutral amino acid transporter 1
LD	Lipid droplet
LNAA	Large neutral amino acid
MADM	Mosaic analysis with double markers
MELAS	Mitochondrial encephalopathy lactic acidosis and stroke-like episodes
Met	Methionine
MSUD	Maple-syrup urine disease
mTOR	Mammalian target of rapamycin
NDD	Neurodevelopmental disorder
NADH	Nicotinamide adenine dinucleotide
NADPH	Nicotinamide adenine dinucleotide phosphate
NEAA	Non-essential amino acid
NE	Neuroepithelial cell
NPC	Neuroprogenitor cell
NMDA	N-methyl-D-aspartate
OAA	Oxaloacetate
OL	Oligodendrocyte
OPC	Oligodendrocyte progenitor cell
OXPHOS	Oxidative phosphorylation
PA	Palmitic acid
PAH	Phenylalanine hydroxylase
PBS	Phosphate buffered saline
PCA	Principal component analysis
PCD	Programmed cell death

PC	Phosphatidylcholine
PE	Phosphatidylethanolamine
PFA	Paraformaldehyde
PG	Phosphatidylglycerol
Phe	Phenylalanine
P	Postnatal day
PNS	Peripheral nervous system
PTM	Posttranslational modification
PUFA	Polyunsaturated fatty acids
QC	Quality control
qPCR	quantitative polymerase chain reaction
RG	Radial glia progenitor cell
RMP	Resting membrane potential
RNA	Ribonucleic acid
ROS	Reactive oxygen species
RT	Room temperature
SD	Standard deviation
SLC3A2	Solute carrier family 3 member 2
SLC7A5	Solute carrier family 7 member 5
SVZ	Subventricular zone
TBST	Tris-buffered saline with tween
TCA	Tricarboxylic acid
Thr	Theonine
TG	Triacylglyceride

Trp	Tryptophan
Tyr	Tyrosine
UPR	Unfolded protein response
Val	Valine
VZ	Ventricular zone
WES	Whole exome sequencing
WHO	World’s Health Organization
WT	wild-type
iSVZ	Inner subventricular zone
oSVZ	Outer subventricular zone
G x E	Gene-environment interaction

1 Introduction

1.1 Cortical development and structure

The human brain is composed of approximately 160 billion neuronal and glial cells, with a subset of ~15-20 million neurons contributing to the formation of the six-layered neocortex[1,2]. This brain region governs the majority of all high-level brain functions, including sensory perception, motor control, cognition, and language[3,4]. Corticogenesis is based on highly conserved cellular and molecular processes that, in humans, span a significant period of time from 3 weeks post-conception to young adulthood[5]. The formation of this complex structure involves several embryonic and postnatal developmental phases, such as neurogenesis, neuronal migration, glial differentiation, and synaptogenesis (Figure 1), all of which are underpinned by a complex interplay between intrinsic genetic programs and extrinsic factors. Disruption of these developmental processes, due to mutations or exposure to environmental stressors, can cause pathological variants of cortical development.

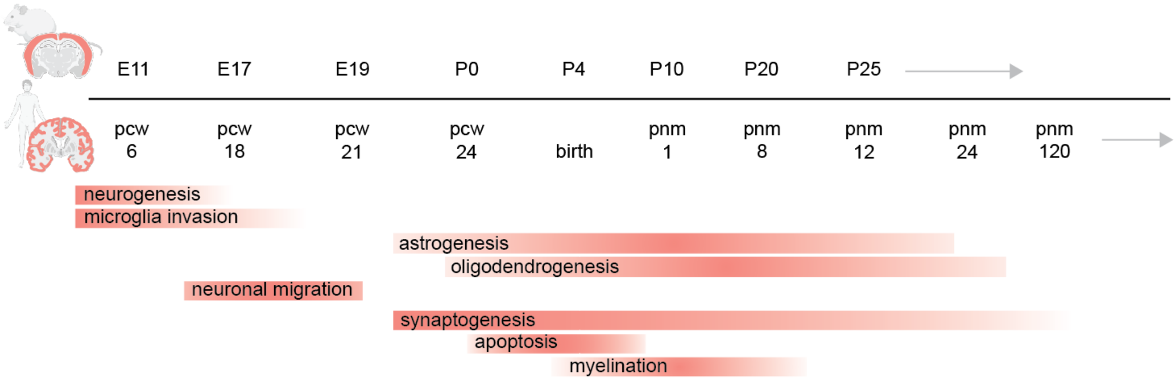

Figure 1. Timeline of the developmental processes during murine and human corticogenesis (adapted from Reemst et al.[6]).

1.1.1 The cortical architecture

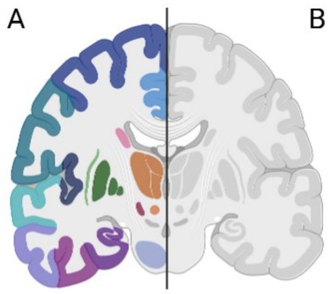

Figure 2. Schematic of a coronal section of a human brain. (A) Neocortical brain regions (B) Grey and white matter of the neocortex.

The neocortex exhibits not only remarkable cellular diversity, but also displays a high degree of organization at different macroscopic levels (reviewed in Adnani et al[7]). First, it is highly regionalized, with specific areas dedicated to relaying various sorts of inputs, such as auditory, somato-sensory, or visual stimuli (Figure 2A). Second, all regions of the cortex consist of two primary layers: the outer gray matter composed of neuronal somata, and the inner white matter containing the myelinated axons of these neurons (as depicted in Figure 2B). The grey matter is further subdivided along its radial axis into six neuronal layers, which are generated in an inside out fashion during corticogenesis (Figure 3) (reviewed in Kwan et al.[8]). All of these layers comprise different sub-types of pyramidal excitatory and inhibitory neurons projecting axons to different cortical and subcortical regions (reviewed in Campbell[9])

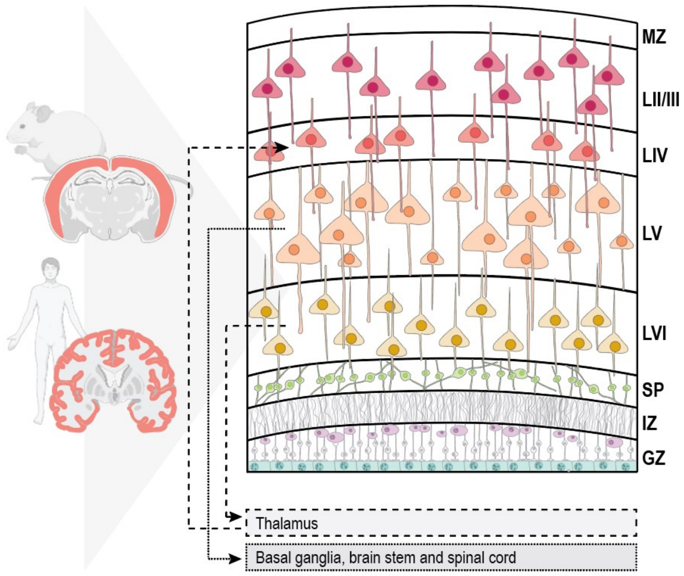

Figure 3. Structure of a cortical column. Schematic displaying the layered structure of the mature cortex; GZ: germinal zone; IZ: intermediate zone; SP: subplate; LVI: layer VI; LV: layer V; LIV: layer IV; LII/III: layer II/III; MZ: marginal zone (layer I). LIV, LV and LVI project and receive input from subcortical regions.

1.1.2 Embryonic corticogenesis

The primary aim of embryonic neurodevelopmental processes is to establish the foundational cell pool that will eventually give rise to a mature six-layered cortex.

Consequently, embryonic corticogenesis is mainly characterized by growth-promoting cellular processes such as proliferation, neurogenesis, migration and differentiation.

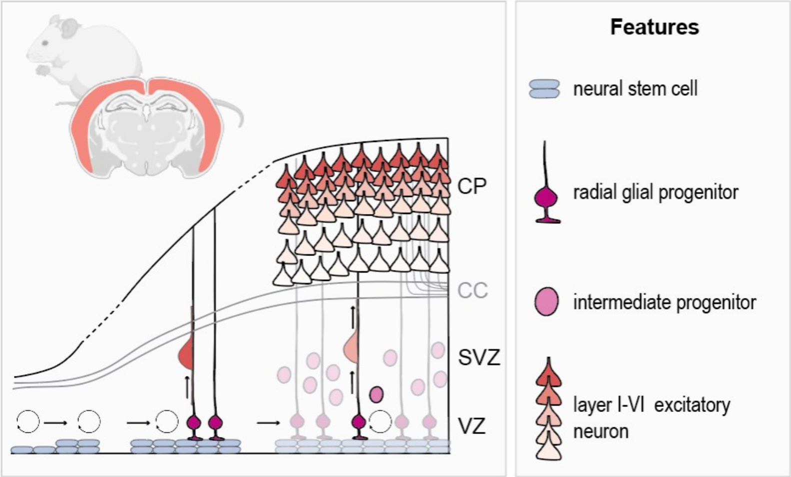

Figure 4. Cellular processes underlying the formation of a six-layered cortex. NE: Neural stem cell; RG: radial glial progenitor cell; IPC: intermediate progenitor cell; VZ: ventricular zone; SVZ: subventricular zone; CP: cortical plate.

1.1.2.1 Neurogenesis

The complex structure of the cerebral cortex is based on the proliferative capacity of a small number of neuroprogenitor cell types (NPCs) that are present throughout different phases of corticogenesis. Most of these proliferative progenitors exhibit the unique ability to perform asymmetric cell divisions, allowing them to maintain a proliferative cell pool and produce post-mitotic neurons in parallel. This process underlies the rapid expansion of cortical volume during embryonic development[10] (Figure 4). During embryogenesis, the cerebral cortex is derived from the highly proliferative neuroepithelial cells (NEs) of the dorsal telencephalic anlage[11] (Figure 4). At embryonic day (E) 10-12 of murine development (equivalent to gestational week (GW) 9 in humans[12]), NEs acquire the identity of apical radial glia progenitor cells (aRGs), which marks the shift from the proliferative to the neurogenic phase in corticogenesis[13,14]. aRGs produce post-mitotic neurons either directly via asymmetric cell division or indirectly via intermediate progenitor cells (IPCs)[15] (Figure 4), which form a second germinal layer, the subventricular zone (SVZ).

1.1.2.2 Migration & Differentiation

During the period of proliferation and neurogenesis a large number of excitatory neurons are generated in the VZ and SVZ, which subsequently migrate into the cortical plate (CP) to establish the layered structure of the neocortex. The formation of the six-layered cortex occurs in a sequential inside-out manner according to the timing of neuronal birth (Figure 4). Two main neuronal classes populate the neocortex during embryonic development: glutamatergic projection neurons and GABAergic inhibitory neurons[16]. Excitatory neurons predominantly perform gliophilic radial migration by using the basal fibers of the RGs as a scaffold (Figure 4), while cortical GABAergic inhibitory neurons invade the cortex tangentially from subcortical regions called the ganglionic eminences[9,17]. The mode and duration of migration are tightly controlled by distinct gene expression patterns[8]. In mice, the migratory phase occurs between embryonic day E12.5 and E18, while in humans it takes place between GW10 and GW23[18]. Upon reaching their final destination within the CP, immature neurons initiate an endogenous differentiation program. The expression of specific marker genes specifies the neuron's layer identity and induces the adaption of morphological characteristics that are unique to each cortical layer[9]. Consequently, the mature neocortex comprises a diverse range of neuronal subtypes[19–22].

1.1.2.3 Embryonic programmed cell death

Although it is seemingly counterintuitive, but apoptosis is a fundamental and strictly controlled tool employed throughout mammalian corticogenesis. In fact, murine and human brain development exhibit different periods of endogenously regulated programmed cell death (PCD) (reviewed in Wong et al.[23] and Blanquie et al.[24]). These surges of cell death are highly conserved, strictly regulated, and cell type-specific and ensure a proper formation and fine-tuning of the cortical network. In mice, the first wave of neural PCD occurs around E6.5 in the distal epiblast, the future neural plate[25]. During corticogenesis, two additional waves of PCD move through the developing pallium. The first wave occurs during embryonic periods, around E10.5, and targets mainly NPCs and newborn neurons located in the germinal layers[26,27]. The second wave occurs during early postnatal development in humans and rodents and marks a critical period for cortical network refinement[28,29]. Interestingly, developmental PCD seems to be aberrant in subpallamic progenitor cells[30]. PCD during embryogenesis plays a pivotal role in removing atypical or displaced cells, thereby preventing propagation of potential defects. In NPCs, PCD is largely triggered by anomalies in cell cycle progression or chromosome number (aneuploidy). This ensures proper DNA replication and repair during the highly proliferative phase of corticogenesis[31,32]. Notably, studies have demonstrated that PCD inhibition during this developmental periods results in increased numbers of aneuploidic cells in the murine cortex[33].

1.1.3 Postnatal cortical development

Although the foundational cortical cell pool is established embryonically, the human brain still undergoes the most notable changes in size and connectivity during postnatal development. Specifically, by 6 years of age, the human brain has already reached 90% of its adult size[5]. This remarkable postnatal growth rate can be largely attributed to two factors: (i) increased gliogenesis and maturation, and (ii) a rapid expansion of the neuropil. Similar to embryonic neurodevelopmental processes, postnatal programs are strictly governed by genetically encoded mechanisms but are further strongly influenced by environmental cues, which refine the cortical network based on individual experiences[34].

1.1.3.1 Gliogenesis and glial maturation

Three distinct types of glial cells are present in the mature central nervous system (CNS), namely astrocytes, oligodendrocytes and microglia, each of which perform specific functions and follow unique differentiation trajectories (Figure 5).

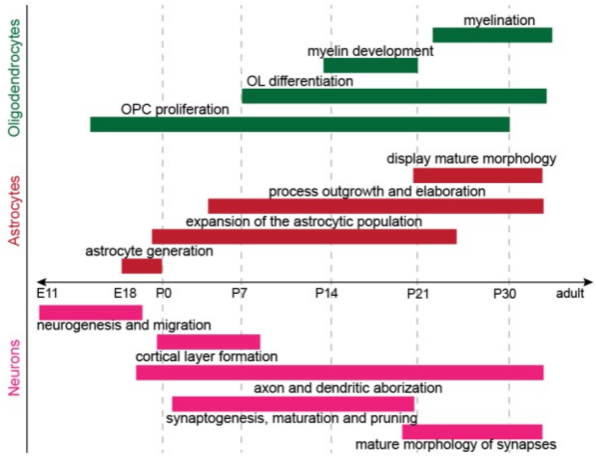

Figure 5. Developmental processes involved in neuronal, astrocyte and oligodendrocyte differentiation and maturation (adapted from Tselnicker et al.[35] and Nishiyama et al.[36]). Timeline (black) covering murine cortical development from embryonic stages to the end of the first postnatal month. Developmental processes occurring during this time period in neurons (pink), astrocytes (red) and oligodendrocytes (green) are shown.

Astrocytes play a crucial role in CNS development and function. During corticogenesis, RGs transition from a mainly neurogenic to a gliogenic potential[37–39]. In rodents, this transition occurs around birth (E.18). This marks the beginning of a 30 day long period of astrocytic proliferation[40,41]. As newly generated astrocytes progressively mature, they start to form elaborated processes and establish connections with neuronal synapses and blood vessels[42]. Through these connections, astrocytes provide metabolic support, neurotransmitter precursors, and ion buffering to neurons[42–45].

Oligodendrocytes (OLs) are responsible for the myelination of neuronal axons, which is essential for efficient neurotransmission in the CNS[46]. However, recent findings indicate that, like astrocytes, OLs also play an important metabolic role for neurons by directly supplying lactate and other metabolites to neuronal axons[47]. During corticogenesis, the oligodendrocyte progenitor cell (OPC) population peaks in density by the end of the first postnatal week, after which they begin to differentiate into myelin-producing OLs[46]. OL differentiation occurs during the first postnatal month, after which OLs begin to progressively myelinate axons of neighboring neurons in concentric layers, thereby providing insulation for improved action potential (APs) transmission[46]. Besides astrocytes and OLs, another type of glial cell, known as **microglia**, populates the mature cortex[48]. This cell type originates from a different germ layer than neural cells and infiltrate the cortex prior to the onset of neurogenesis. Microglia act as immune cells of the brain and are responsible for various functions such as waste clearance and synaptic pruning[48].

1.1.3.2 Synaptogenesis and pruning

Synapses serve as specialized sub-cellular compartments that mediate transmission of chemical or electrical signals between presynaptic and postsynaptic neurons via release of neurotransmitters stored in vesicles into the synaptic cleft in response to presynaptic APs (reviewed in Südhof[49] and Petzoldt et al.[50]). The proper formation and function of synapses, including the ability to modulate their strength in response to changes in activity, is a prerequisite for basic brain function. Synaptogenesis occurs throughout an organism's lifespan but is particularly enhanced during brain development. In rodents, the formation of the first cortical synapses occurs at around P5-P7[51,52]. This phase of production is followed by a period of network refinement, during which a substantial fraction of functional synapses are pruned[53–57 58]. The rates of pruning are highest during early postnatal periods, but they continue to persist throughout the entire lifespan of an organism. This is mainly because the process plays a crucial role in reinforcing the connections that are essential for the processing of specific environmental stimuli.

1.1.3.3 Developmental changes in network activity

The process of neuronal network formation and communication is the fundamental basis of brain function. Importantly, during neurodevelopment, the activity patterns of a maturing cortical network change constantly. These variations follow a distinct temporal sequence that reflects the formation and strengthening of neuronal connections[24,59]. The first signatures of neuronal activity occur during late embryonic corticogenesis in mice, where individual excitatory neurons start to display sparse, desynchronized Ca2+ spikes, despite not being integrated in a network yet[60] (Figure 6A). At birth, neurons are coupled via gap junctions, resulting in spontaneous network-wide Ca2+ waves[61,62] (Figure 6A). During the first two postnatal weeks, neurotransmitter-dependent network activities start to emerge. This phenomenon coincides with the peak of PCD, a process crucial for cortical network refinement[24,59,63,64] (chapter 1.1.4.4). Importantly, around this time different cortical layers start to receive inputs from subcortical regions aswell[65,66]. After the first postnatal week, as neuronal maturation progresses, the network begins to de-synchronize, thereby starting to present with firing patterns characteristic of mature cortical circuits[67,68] (Figure 6A).

1.1.3.4 Postnatal programmed cell death

During embryonic corticogenesis, excessive numbers of cortical neurons are generated. Here, the process of apoptosis plays a critical role in the removal of redundant neurons to establish a refined cortical network. While embryonic PCD is mainly used to eliminate impaired NPCs, postnatal apoptosis is primarily responsible for sculpting an efficient network. This phenomenon occurs during the first two postnatal weeks in rodents (P2-P10), while in humans, it starts during embryonic periods and persists until the first postnatal months (Figure 1)[18]. In mice, postnatal PCD consists of two sub-waves affecting different cellular populations. Cortical pyramidal neurons are eliminated between P2 and P5, followed by cortical inhibitory neurons, which adjust their numbers between P5 and P10 (Figure 6B)[23,28,29]. About one-third of all embryonically generated inhibitory neurons are removed via PCD during the first postnatal week[29,69–71]. But what are the factors that determine which neurons are eliminated and which ones are spared?

In the peripheral nervous system (PNS), neurotrophic factors play a critical role in modulating neuronal numbers[72]; however, the mechanisms determining cortical neuron survival remain incompletely understood. Several studies have indicated that during perinatal periods, the survival of cortical neurons is more dependent on electrical activity and synaptic inputs than on the availability of growth factors[73–75]. Notably, the peak of the postnatal PCD wave in murine cortical neurons (P5) coincides with the first occurrence of spontaneous neurotransmitter-dependent activity (see chapter 1.1.4.3). Interestingly, various *in vivo* and *in vitro* experiments have shown that cortical interneurons are predetermined to undergo apoptosis at a specific age (12 days after differentiation), and that synaptic inputs from excitatory pyramidal neurons are critical in blocking the apoptotic program in these inhibitory neurons[29,71,76]. Moreover, changes in the excitability of pyramidal neurons directly impacts the survival rate of neighboring inhibitory neurons[29]. Notably, blocking apoptosis in cortical excitatory neurons can prevent PCD in adjacent inhibitory neurons[29].

These results underscore the complex interplay between neuronal activity and survival rates in the CNS. However, it remains ambiguous which factors cause the variability in activity levels between individual neurons. The intrinsic neuronal fitness, as determined by the metabolic state of the cell, is a plausible factor that could potentially account for inter-neuronal variance in activity, especially since cellular metabolism and activity are linked at several levels. A number of studies suggest that the availability of certain nutrients and bioenergetic substrates directly influences neuronal excitability. For instance, impaired neuronal glucose accessibility, due to mutations in genes associated with glucose transport and catabolism, result in decreased basal cortical electrical activity, reduced excitability in fast spiking interneurons and increased seizure susceptibility in patients[77,78]. This phenomenon is further exploited in the context of epilepsy treatment. The ketogenic diet, which is characterized by a low-sugar, high-fat intake, has demonstrated remarkable efficacy in mitigating seizure activity in a subset of epilepsy patients[79].

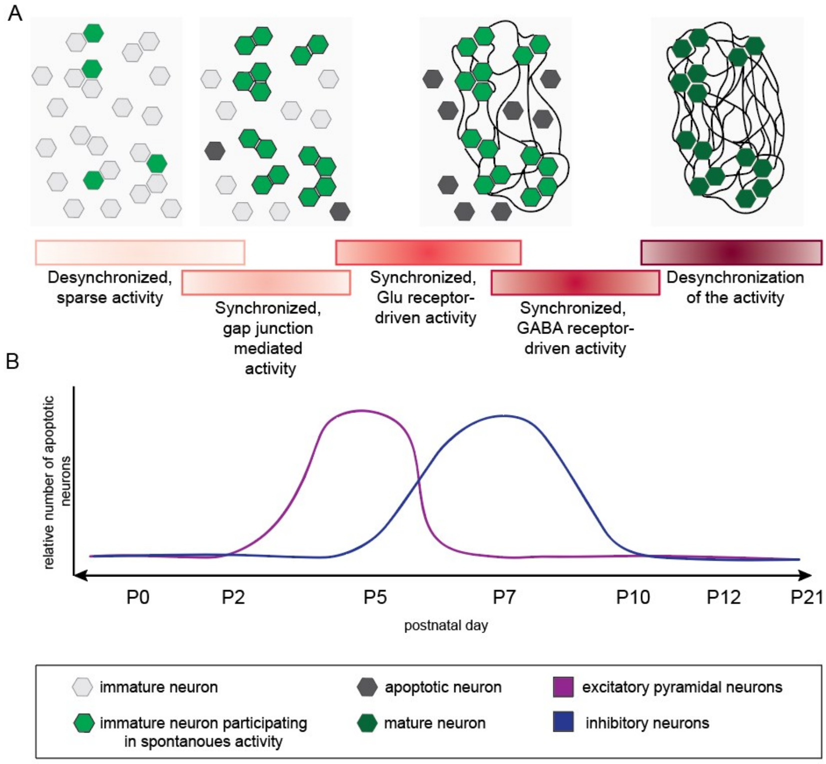

Figure 6. Temporal dynamics of spontaneous activity and apoptosis in the postnatal rodent neocortex (adapted from Blanquie et al.[24]). (A) At late embryonic timepoints, single neurons start to display stochastic activity. During the first postnatal days neurons are connected via gap junctions. Around P5 neurotransmitter-dependent synchronous activity starts to dominate. From around P10 on, neuronal networks start to decorrelate. (B) The number of apoptotic excitatory neurons starts to increase shortly after birth and peaks around P5, when glutamate-dependent synchronous activity is prevalent. Programmed cell death of GABAergic interneurons starts around P5 and peaks at P7 after birth. Coincident with the decorrelation of neuronal networks.

1.2 The metabolism of the cortex

Humans present with an exceptional range of motor and intellectual skills, which surpass those of any other known species. This is mainly attributed to the evolutionary development of the highly efficient and complex neocortex. Throughout neocortical evolution, a 1000-fold increase in the number of neurons contributed to the enhanced cognitive abilities of higher mammalian species[80]. These high levels of cognitive performance are based on an extensive network of neurons that communicate through APs. However, these cellular networks have significant energetic and anabolic costs. The adult brain requires 20% of the available oxygen and 25% of available glucose taken up by the body, despite making up only 2% of the human's body weight[81]. Neurons require substantial energy to maintain ion gradients essential for a stable resting membrane potential (RMP) and the generation of APs[82]. Therefore, this cell type is considered the most energy-demanding in the nervous system. Among neural cell types, excitatory neurons consume nearly 80% of the available energy for glutamate-based neurotransmission, with 13% required for maintaining the RMP[82].

To ensure the brain functions as a complex cellular network, various levels of cellular and structural relationships, as well as local and global metabolic cooperation among specialized cell types, are essential. This results in a brain that is metabolically highly compartmentalized, wherein diverse cell types utilize distinct bioenergetic pathways or produce different metabolites that are exchanged intercellularly. Importantly, the utilized metabolic pathways and the abundance of individual metabolites both intra- and extracellular determine the metabolic state of a cell. Each cell type within these networks possesses a unique metabolic profile with varying degrees of metabolic flexibility to adapt to external circumstances such as nutrient scarcity. Recently it has become increasingly evident that a cell's metabolic profile is not only fundamental to its function but also to its cell fate. Especially during neurodevelopmental periods of proliferation, differentiation and integration, extensive metabolic reprogramming has to occur. This allows the cells to adapt to different environmental conditions like oxygen availability, feeding strategies, or changing anabolic demands of a newly adopted cell fate. But what are the signals that trigger transient or permanent metabolic reprogramming of cells? On a systemic level, inter-tissue communication mainly relies on the exchange of hormones and other signaling molecules[83,84]. Meanwhile, intracellular communication and metabolic responses are mostly regulated on the transcriptional and translational level by modulating the abundance of metabolic enzymes and regulatory factors specific to a given tissue and circumstance. Enzyme function is further regulated through posttranslational modifications (PTMs). These processes collectively assign metabolites to metabolic pathways in the necessary proportions to match the individual cell's requirements. Importantly, deviations from a sustainable degree of metabolic flexibility can jeopardize cellular resilience thereby causing neuropathological outcomes[85–87].

1.2.1 Energy production pathways of the mature cortex

While cortical cells share fundamental metabolic currencies like ATP, acetyl-CoA, NADH, and NADPH, the distinct metabolic pathways utilized for their generation differ among neural cell types. The choice of pathways is dependent on various factors, such as the cell's metabolic flexibility, substrate availability and its microenvironment. Importantly, the proportion of activity between different branches of bioenergetic pathways is the main factor that determines the metabolic state of the cell[84,88]. Glucose is the primary macronutrient incorporated into the bioenergetic pathways of the cortex[82]. However, the exact metabolic pathways used to catabolize glucose vary between different neural cell types. The primary factors determining the preference for a specific catabolic pathway by a given cell type are (i) the level of oxygen availability and (ii) the capacity of the cell to endure the metabolic byproducts generated through these different reactions.

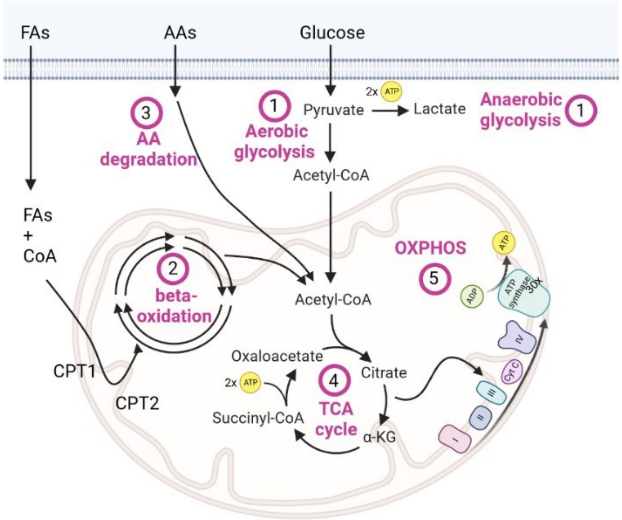

Figure 7. Schematic of the main bioenergetic pathways employed by neural cell types. (1) Anaerobic glycolysis and aerobic glycolysis; (2) fatty acid (FA) degradation via beta-oxidation; (3) amino acid (AA) degradation; (4) tricarboxylic acid cycle (TCA cycle); (5) Oxidative phosphorylation (OXPHOS).

1) Glycolysis: Glycolysis is a metabolic pathway that involves the conversion of glucose to pyruvate through ten enzymatic reactions (reviewed in Bauernfeind et al.[89]). It is one of the few bioenergetic pathways that does not require oxygen. The subsequent metabolic fate of pyruvate within the glycolytic pathways depends on both, the cell type and the oxygen availability. Some cell types utilize the anaerobic form of glycolysis to convert pyruvate to lactate (Figure 7 (1)). This method is simple but results in a low energy yield of only 2 ATP and 2 NADH. Importantly, this process can cause a significant change in intracellular pH, forcing specific cell types to avoid this bioenergetic strategy. Aerobic glycolysis is a more productive way of ATP production. It involves the transfer of glycolytic pyruvate into the mitochondrial tricarboxylic acid (TCA) cycle via Acetyl-CoA as intermediate. Importantly, whenever glucose is scarce, cells may adapt by utilizing amino acids (AAs), fatty acids (FAs), or their derivatives to fuel the TCA cycle.

2) Beta-oxidation: FAs possess a higher energetic potential per gram compared to glucose, rendering them highly efficient energy substrates. Organs with high energy demands such as the heart derive up to 50-70% of their ATP from FA degradation via the catabolic pathway of beta-oxidation (reviewed in Houten et al.[90]). In detail, long chain fatty acyl-CoAs, the primary components of FAs, undergo breakdown into Acetyl-CoA, which subsequently enters the TCA cycle (Figure 7 (2)). Prior to being transported into the mitochdondrial beta-oxidation machinery, FAs need to be "activated" via conjugation with a coenzyme A (CoA). Importantly, transfer of long-chain fatty acyl-CoAs across the mitochondrial membrane is not possible without prior transforming them into acylcarnitine (AC) through the catalytic activity of carnitine palmitoyltransferase 1 (CPT1). Inside the mitochondria, carnitine palmitoyltransferase 2 (CPT2) catalyzes the reconversion of long-chain acylcarnitines (ACs) into their corresponding long-chain fatty acyl-CoAs, which are then channeled towards the process of FA oxidation. Beta-oxidation is a metabolic pathway that comprises four stages of enzymatic dehydrogenation and hydrogenation, resulting in a reduction of the acyl-CoA chain length by two carbon atoms per cycle. Each complete cycle generates one molecule of Acetyl-CoA and NADH. Acetyl-CoA then undergoes subsequent oxidation by being incorporated into the TCA cycle, whereas the shortened acyl-CoA chain is further subjected to additional rounds of beta-oxidation until only one Acetyl-CoA molecule remains.

The majority of all FAs, including short-, medium-, and long-chain FAs, are predominantly degraded in mitochondria, whereas, the breakdown of very-long-chain fatty acids (VLCFAs) takes place in peroxisomes[91,92]. Peroxisomes are small, single-membrane-bound organelles, which are highly abundant in every mammalian cell. They interact directly with different organelles, lysosomes and lipid droplets[93,94]. Peroxisomes perform diverse functions in catabolic and anabolic pathways. In lipid metabolism, peroxisomes play particularly significant roles in beta-oxidation, reactive oxygen species management, and ether-phospholipid biosynthesis. Furthermore, peroxisomes are also involved in processes such as the synthesis of bile acid, docosahexaenoic acid, and cholesterol[91,95].

3) Amino acid degradation: The traditional view on brain metabolism is that it relies mainly on glucose. Nevertheless, there is growing recognition of the potential use of AAs as an alternative cellular energy source. For instance, glutamine, an essential amino acid (EAA), is an important amine group donor. The anaplerotic metabolism of glutamine results in the production of α-ketoglutarate (α-KG) and oxaloacetate (OAA), which are significant constituents of the TCA cycle[96] (Figure 7 (3)). Likewise, the catabolism of mitochondrial Branched-chain amino acids (BCAAs), valine, leucine, and isoleucine, has been shown to be a critical driver of mitochondrial ATP production and serves as an alternative source of Acetyl-CoA[97–99] (see chapter 1.2.4).

4) TCA cycle: The TCA cycle is an essential metabolic pathway in respiring cells that serves as the central hub of cellular metabolism (reviewed in Martinez-Reyes et al. [100]). It comprises a closed loop of 8 chemical reactions that enable the production of several bioenergetic currencies such as ATP, NADH, and FADH2, as well as critical metabolites for biosynthetic reactions (Figure 7 (4)). During this process, some of the generated metabolites are transported to the cytosol and used for biosynthetic processes. For instance, cytoplasmic citrate can be re-converted into Acetyl-CoA, which is utilized in lipid and nucleotide synthesis. In the presence of oxygen, the energetic currencies are further utilized in the process of oxidative phosphorylation (OXPHOS), which increases the ATP yield substantially.

5) Oxidative phosphorylation: In cellular respiration, OXPHOS is the most potent pathway for ATP generation. This process involves the reduction of molecular oxygen, which serves as an electron acceptor, thereby resulting in the generation of ATP. The electron transport chain (ETC), a set of five protein complexes comprised of various metal and lipid moieties, are the key components of this pathway[101]. In-depth, four of the ETC complexes use electrons provided by TCA cycle-derived NADH and FADH2 to pump protons across the inner mitochondrial membrane (Figure 7 (5)). The protons subsequently flow back across the membrane and down the potential energy gradient which converts ADP into ATP via a phosphorylation reaction[101]. This process is highly efficient in generating ATP[101]. However, utilization of OXPHOS has some caveats to it, as it inevitably generates ROS, which can cause oxidative stress if present in high levels. ROS accumulation can impair cellular physiology by causing DNA or RNA damage or lipid and AA oxidation[102,103,104]. To counteract these free radicals and neutralize oxidants, the cell employs various antioxidants, such as glutathione[105].

1.2.2 Metabolic programs of cortical cell types

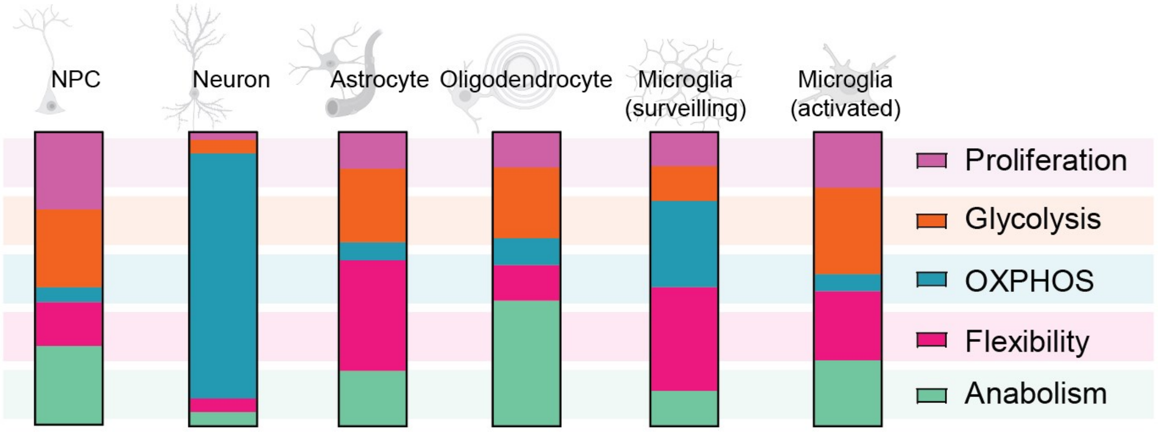

Figure 8. Metabolic make-up of cortical cell types (adapted from Traxler et al.[88]). Depending on their function different cortical cell types reside in diverse metabolic states.

During the early stages of brain development, neural stem cells and NPCs undergo a period of extensive proliferation, followed by a sequence of fate decisions and differentiation processes that are crucial for proper network formation[106]. During the phase of proliferation, the metabolism of progenitor cells is focused on generating building blocks for organelles, and DNA[107]. In addition to their remarkable proliferative capacity, multipotent NPCs must undergo sequential fate decisions to differentiate into the various neural cell types that make up the mature brain. These transitions involve significant metabolic adaptations, with the most pronounced changes occurring during the transition from a proliferative progenitor to a post-mitotic neuronal fate. In the brain, distinct cell types with varying metabolic demands and priorities exhibit unique metabolic states, resulting in a highly heterogeneous metabolic landscape within the mature cortical network (Figure 8). This metabolic diversity across different cortical neurons and glial cells is based on differences in employed bioenergetic pathways, substrate utilization, and lipid profiles[108]. Neuronal cells preferentially utilize oxidative metabolism, while astrocytes rely mainly on glycolysis, making them less sensitive to atmospheric oxygen levels. The level of metabolic flexibility and ability to switch between bioenergetics pathways varies between cell types. Neurons are particularly intolerant to certain metabolic pathways, such as anaerobic glycolysis, which if imposed on them even results in de-differentiation[88,109]. The metabolic variances observed between neural cells necessitate a precisely coordinated interplay between them to ensure appropriate functioning and development of the CNS.

Neuroprogenitor cells: The metabolism of embryonic NPCs is highly active and shares many transcriptomic, epigenetic, and metabolic traits with other highly proliferative cell populations, including certain types of cancer cells[88]. During early embryonic development, NPC metabolism relies on anaerobic glycolysis, which is redirected towards the pentose phosphate pathway (PPP), to increase nucleotide synthesis and meet the high anabolic demands of the proliferating cell[107,110–112]. While glucose is the preferred bioenergetic substrate, NPCs are metabolically flexible (Figure 8). NPCs metabolize carbohydrates, FAs, or AAs to balance catabolism and anabolism according to their current needs[110]. Moreover, the metabolic plasticity in NPC fate decisions is fueled by their ability to adapt to cell-type specific metabolic programs induced by the transcriptional programs of the new cell fate[110]. For instance, the metabolic switch from anaerobic glycolysis to OXPHOS during neuronal differentiation plays a critical role in determining cell fate[107,109]. Achieving a continuous shift to OXPHOS in NPCs is crucial for the generation of neurons, while the retention of anaerobic glycolysis promotes glial cell fate[109,113,114].

Neurons: Neurons represent the only post-mitotic cell type in the CNS. Consequently, these cells prioritize survival and maintenance of a neural networks, over metabolic flexibility, regeneration and proliferation. Due to their high sensitivity, neurons possess a specialized metabolic state that supports their neuronal fate and allows for efficient ATP generation without jeopardizing their survival[88,115]. The primary goal of neuronal metabolism is to produce large amounts of ATP, with 60-75% of the brain's energy budget allocated for generating and propagating APs. The rest is utilized for anabolic metabolism and maintenance, including protein synthesis, signaling transduction cascades, lipid metabolism, and cytoskeletal remodeling[89,116–118]. In order to meet these high energy demands, neurons heavily rely on mitochondrial OXPHOS. As a result, neurons are the primary oxygen consumers in the brain[115,118]. Disturbances in mitochondrial OXPHOS underlie a variety of neuropathologies and are commonly observed in diseases with neurodegenerative components[119–121]. In fully mature neurons, glucose is the principal fuel for OXPHOS. It is noteworthy that even though neurons utilize the efficient bioenergetic process of OXPHOS, it fails to fully satiate their energetic demands. This can be attributed to the neuron's limited capacity to store energy in the form of glycogen or lipid droplets[122–124]. Therefore, mature neurons exhibit a significant dependency on glial cells for metabolic support, particularly in the form of lactate[42,47]. Importantly, the means by which immature neurons fulfill their heightened energy demands during perinatal periods in the absence of glial support remains unknown.

Astrocytes and oligodendrocytes:

In contrast to neurons, glial cells exhibit a high degree of metabolic flexibility, allowing them to quickly adapt to changes in nutrient availability[115]. Astrocytes have the capacity to switch between anaerobic glycolysis and OXPHOS depending on the available substrates (Figure 8). Under conditions of hypoglycemia, astrocytes metabolize AAs such as glutamate, aspartate, and alanine[125,126]. Importantly, in times of nutrient scarcity or during highly energy-demanding processes, such as AP firing, glia do not only generate bioenergetic components for their own use, but also provide metabolic intermediates to neighboring neurons[45,111]. An auxiliary strategy provided by astrocytes is the "astrocyte-neuron lactate shuttle," wherein astrocytes synthesize and secrete lactate that is subsequently transported to neighboring neurons to serve as a substrate for the TCA cycle through pyruvate[42]. Additionally, astrocytes participate in the removal of neurotransmitters from the synaptic cleft through the "glutamine-glutamate cycle" to prevent supraphysiological levels of neurotransmitters and excitotoxicity[127]. Lipid metabolism constitutes another indispensable facet of astrocytic function. Under conditions of increased FA availability, astrocytes are the predominant site of beta-oxidation. Moreover, astrocytes play a pivotal role in maintaining neuronal cholesterol homeostasis, primarily through their involvement in brain lipoprotein synthesis. Of particular significance is ApoE, the main component of lipoproteins facilitating the transfer of astrocytic lipids and cholesterol to neurons[128,129]. Oligodendrocytes are essential for the efficient propagation of APs by myelinating the axons of neurons. During the process of differentiation and myelination, OLs display an increased demand for energy and FAs. In order to fulfill this demand, OLs primarily depend on OXPHOS for adequate ATP generation. Indeed, during the metabolically demanding developmental phase of myelination, oligodendrocytes depend on metabolic support from astrocytes[130]. After the primary period of myelination, OLs switch to anaerobic glycolysis (Figure 8). During this post-myelination phase, OLs provide metabolic support to neurons by supplying lactate directly to their axons[47,131,132].

Microglia: Microglia are considered the immune cells of the brain. Under normal, surveilling conditions, microglia predominantly rely on OXPHOS for ATP generation (Figure 8). However, microglia are highly metabolically adaptable, allowing them to exert their functions even during periods of starvation, hypoxia, and inflammation[133,134]. In response to an inflammatory stimulus, microglia transition into an activated state, characterized by a metabolic switch from OXPHOS to anaerobic glycolysis, similar to peripheral immune cells[133,134] (Figure 8).

1.2.3 Amino acid metabolism of the brain

The basis of eukaryotic AA metabolism is formed by 20 canonical amino acids, all of which are proteinogenic. A subset among these cannot be synthesized endogenously and must be obtained from external sources such as diet. They are therefore considered “essential” AAs (EAAs)[135]. In addition to their role as building blocks for proteins, both, EAA and nonessential amino acids (NEAA) are important substrates for bioenergetic pathways. Further, several AAs and their derivatives are crucial components of cellular processes, such as epigenetic regulation, neurotransmission, and nucleotide synthesis[136–138]. Importantly, the BBB is selective in the transport of AAs. This leads to a competition for transport over the BBB even at physiological AA plasma concentrations[139]. This makes the brain unique regarding its reliance on local synthesis of NEAAs. The majority of all NEAAs are synthesized from a small subset of canonical AAs, including glutamine, glutamate, methionine, arginine, phenylalanine, and leucine[140]. Especially, the conversion of glutamine to glutamate and the metabolism of arginine and its derivatives are particularly important metabolic pathways in the brain[141,142]. Likewise, BCAAs are known to have a significant impact on brain metabolism. Notably, around 30% of the nitrogen found in brain glutamate/glutamine can be attributed to leucine[143,144]. The maintenance of cortical **glutamate homeostasis** is critical for brain function. Aside from serving as the principal excitatory neurotransmitter in the cortex, glutamate plays a significant role as a precursor to other AAs, including aspartate, and the inhibitory neurotransmitter gamma-aminobutyric acid (GABA)[127,145]. Further, the process of **nucleotide synthesis** is also heavily dependent on AAs, especially on glycine, glutamine, aspartate, serine, and methionine. These AAs function as carbon and nitrogen donors for biosynthesis of both, purine and pyrimidine molecules[140,146]. Glutamate, glycine, and cysteine are further important for generating glutathione, a key player in **redox balance**[147,148]. Maintaining redox homeostasis is particularly critical for neuronal survival due to the high demand for OXPHOS and ROS management in neurons[149]. Finally, it should be noted that AAs and their derivatives play critical roles not only as substrates in metabolic pathways, but also in the regulation of gene expression and protein function through epigenetic and post-transcriptional modifications. Specifically, components of the methionine cycle, which is fueled by methionine, serine, and glycine, are essential for DNA and histone methylation[150–153]. Moreover, the acetylation of proteins and histones involves the utilization of Acetyl-CoA, which is derived from the catabolism of BCAAs and other AAs[140,154].

It is evident that AAs play a critical role in cellular physiology, but how does the brain effectively maintain AA homeostasis? In order to sustain the brain's AA demand, EAAs have to be transferred from external sources across the BBB into the brain. In humans, intracellular and tissue wide AA transport is facilitated by over 50 distinct transporter protein classes[155]. Among these are the Heteromeric Amino Acid Transporters (HATs), which belong to a group of transporters that cover the full range of AAs as substrates. In humans, HATs are constituted by a light and a heavy subunit connected by a disulphide bond. Specifically, there are two homologous heavy subunits and eight light subunits, grouped into the SLC3 and SLC7 transporter families[143]. Heavy subunits, such as 4f2hc (SLC3A2), are required for the localization of the light subunits to the plasma membrane[143,156]. The SLC7 family includes two distinct groups, the Cationic Amino Acid Transporters (CATs)[157], and the light subunits of Heteromeric Amino Acid Transporters[156]. Six of these light subunits combine with SLC3A2, namely LAT1, LAT2, y+LAT1, y+LAT2, Asc-1, and xCT[158–165]. These interactions establish the specificity of the transported substrates[143,156].

SLC7A5, known as LAT1, facilitates the antiport of metabolically-essential large neutral amino acids (LNAAs) across plasma membranes in a pH and sodium independent manner[166] (Figure 9). SLC7A5 plays a pivotal role in cellular physiology due to its involvement in the transport of EAAs to specific organs such as the placenta and across the BBB. The essential role of this transporter in cellular metabolism and growth is underlined by the fact that in mice a constitutive knockout of *Slc7a5* is lethal by E11.5[167]. Importantly, SLC7A5 exhibits a relatively low transport capacity, which makes it unsuitable for facilitating the absorption of dietary AAs in the gastrointestinal tract[168]. The highest levels of *SLC7A5* expression are detected in the testis, bone marrow, placenta, and brain[156,169]. In polarized epithelial cells, the distribution of SLC7A5 protein is predominantly restricted to basolateral membranes[156,170], except for the BBB, where it is found on the apical and basolateral cell membranes to facilitate AA antiport between the blood and the brain[171]. Importantly, the LAT1/CD98 heterodimer does not only localize to the plasma but also to the lysosomal membrane[172].

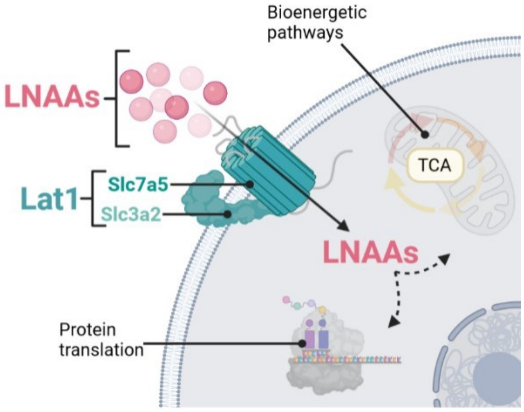

Figure 9. The Heteromeric transporter Lat1 catalyzes large neutral amino acid (LNAA) flux across the plasma membrane. The transporter Lat1 comprises a heavy (Slc3a2) and light subunit (Slc7a5). Slc7a5 encodes the transmembrane spanning domain of the transporter, which transports LNAAs in a pH and sodium independent manner. LNAAs are utilized for protein translation or are transferred into bioenergetic pathways, such as the TCA cycle.

1.2.3.1 Large neutral amino acids

The cluster of LNAAs consists of nine canonical amino acids, specifically leucine (Leu), isoleucine (Ile), valine (Val), methionine (Met), phenylalanine (Phe), tyrosine (Tyr), tryptophan (Trp), threonine (Thr), and histidine (His). Each single one plays a significant role in various essential functions of brain physiology.

Tyrosine is a precursor to the neurotransmitters and neuromodulators dopamine, norepinephrine, and epinephrine, which are known to modulate a variety of physiological responses, including mood, cognitive function, and stress response[173]. Importantly, tyrosine is nonessential. It can be synthesized from **phenylalanine**, another LNAA[174]. **Tryptophan**, on the other hand, functions as the precursor to the neurotransmitter serotonin, which is involved in regulating mood, appetite, and sleep[175]. **Methionine**, another LNAA, is an indispensable sulfur-containing AA, which is part of the folate-methionine cycle[151]. Methionine is converted to S-adenosyl-methionine (SAM), which acts as the primary methyl group donor[150]. Dysfunction of the folate-methionine pathway has significant effects on vital cellular processes, including DNA synthesis, DNA methylation, and cellular redox balance. Further, Methionine acts as a precursor for the biosynthesis of various essential molecules, including succinyl-CoA, cysteine, creatine, and carnitine[152,176,177]. **Histidine** is an AA that is highly abundant in the brain, where it is primarily metabolized into histamine. Histamine acts as a neuromodulator and plays a role in the regulation of sleep, appetite, and learning and memory[178–180].

The BCAAs **leucine**, **isoleucine** and **valine** hold significant importance in brain metabolism. In muscle and cancer cells BCAAs, especially Leu, are potent modulators of the mTOR signaling pathway[181,182]. Hagenfeldt et al.'s pioneering study in 1980 revealed that peripheral tissues take up 55% of intravenous leucine, 25% goes to the visceral region, and 10% to the brain, underlining the brain's dependency on sufficient BCAA supply[183]. In non-neuronal cell types, BCAA catabolism mainly takes place in the mitochondria. The process involves several enzymatic steps, with the initial step being a BCAA transamination reaction by the BCAA transaminase (BCAT) (Figure 10). There exist two different BCAT proteins, one localizing to the mitochondria, while the other is mainly distributed throughout the cytoplasm. The brain is rich in BCAT activity, and both, cytosolic (BCAT1) and mitochondrial enzymes (BCAT2), are expressed (reviewed in Sperringer et al.[184]). These enzymes transfer the α-amino group from BCAAs to α-KG, resulting in glutamate and three distinct branched-chain α-ketoacids (BCKAs). These ketoacids are subsequently catabolized by several AA-specific enzymes, including the branched-chain α-ketoacid dehydrogenase complex (BCKDH). Due to the fact that BCAAs are so important for brain function the catabolism of these AAs is strictly regulated. The branched-chain α-ketoacid dehydrogenase kinase (BCKDK) modulates the activity of BCKDH by phosphorylation and subsequent inactivation. The catabolism of BCAAs generates important metabolic products such as Acetyl-CoA, Propionyl-CoA, Succinyl-CoA and C3 & C5-acylcarnitines (Figure 10), which are further channeled into other metabolic pathways such as the TCA cycle, beta-oxidation or cholesterol and FA synthesis. Notably, not only the end products, but also the enzymes involved in BCAA catabolism are shared with lipid catabolism. Suggesting a link between these two pathways. For instance, Bckdk, which inhibits BCAA breakdown in mitochondria, has recently been shown to be a crucial regulator of FA synthesis in the cytoplasm[185] (Figure 10).

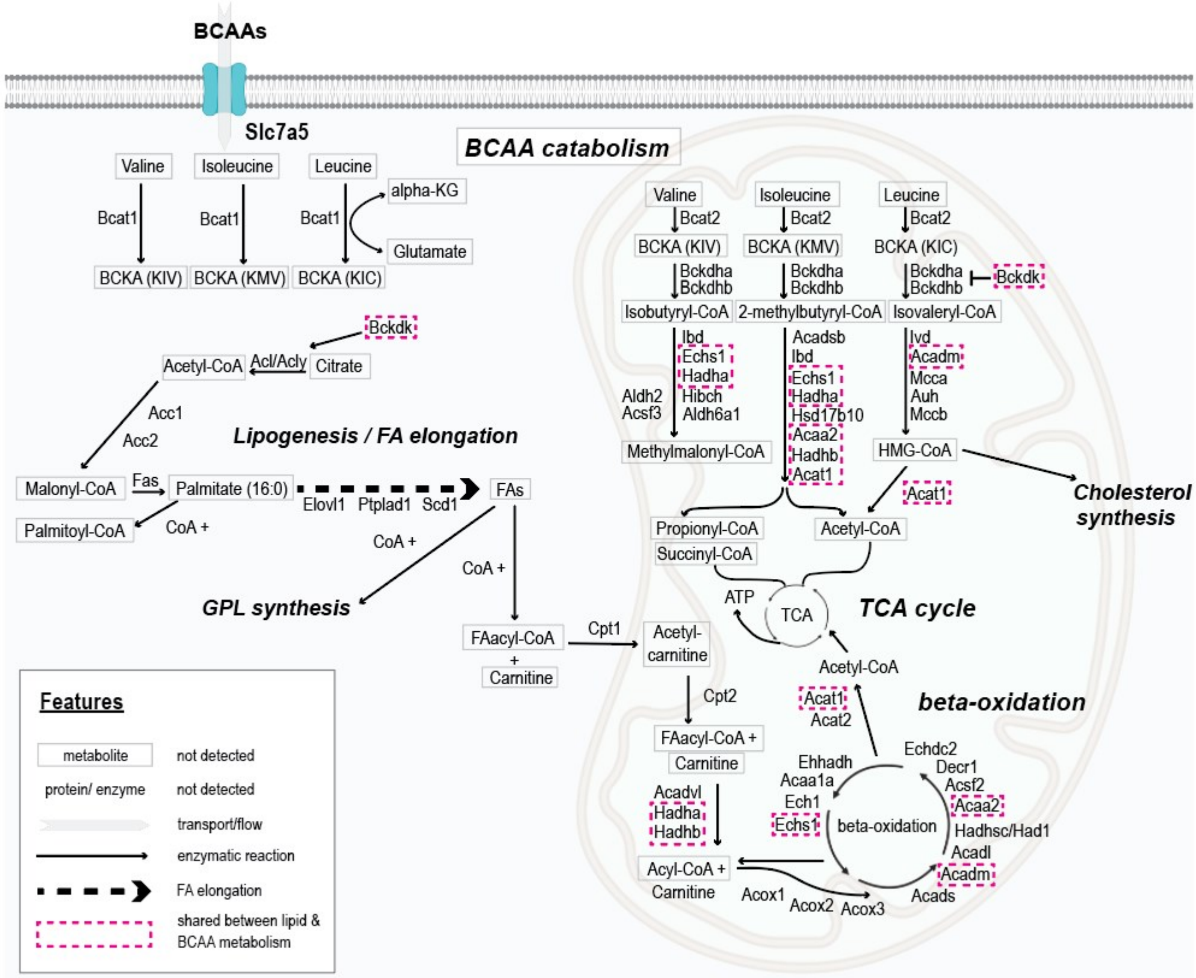

Figure 10. The link between BCAA catabolism and lipid metabolism. The schematic depicts metabolites and enzymes associated with the metabolic pathways: “BCAA catabolism”, “FA degradation” (beta-oxidation) and “FA synthesis/elongation”. Enzymes shared by the BCAA and FA pathways are highlighted by a dashed rectangle.

1.2.4 Lipid metabolism of the brain

About 50-60% of the human brain's dry mass is composed of lipids. In contrast to adipose tissue, which primarily serves as an energy depot by storing triglycerides, the brain comprises mainly of acylated lipids, which are key components of plasma membranes and myelin[186]. Importantly, not only the lipid- but also the FA composition of the brain differs from other tissues. The FA profile features a considerable abundance of essential polyunsaturated fatty acids (PUFAs), namely arachidonic acid (AAC), eicosapentaenoic acid (EPA), and docosahexaenoic acid (DHA), which all need to be derived from external sources[187]. FAs function as the main building blocks for lipid biosynthesis and serve as significant bioenergetic substrates[188,189].

Lipids are typically characterized by their polar head group and hydrophobic acyl side chains derived from FAs. In the brain, the major lipid classes are glycerophospholipids (GPLs), sphingolipids (SLs), and cholesterol[190], which all play essential roles in the formation of plasma membranes and various developmental and signaling processes such as synaptogenesis, anchoring of membrane proteins, and ion-channel function[191]. Membranes in eukaryotic cells exhibit remarkable structural diversity on a cellular and subcellular level, thereby defining cell organelle identity and function[192,193]. The exact lipid composition of membranes influences membrane features such as surface charge, lipid packing density, and bilayer thickness[193]. Intriguingly, there has been a growing interest in the functional diversity of the plasma membrane beyond its traditional function as a protective barrier. Specifically, it has been found that the membrane serves as a dynamic reservoir of lipid signaling molecules. For instance, upon the binding of neurotransmitters, neurotrophic factors, and cytokines, lipid messengers can be enzymatically cleaved off the cell membrane (see chapter 1.2.5.3). These lipid mediators further modulate cellular physiology. Altogether, the short-term availability of lipid-mediators such as phosphatidylinositol 4,5-bisphosphate (PIP_2), or free FAs, and the long-term developmental changes in membrane composition modulate neuronal activity and physiology[194].

1.2.4.1 Lipid biosynthesis

The endoplasmic reticulum (ER) is the primary location for lipid synthesis, membrane protein folding and insertion in neural cells[195] (Figure 11). Within the ER, the majority of GPLs and sterols are synthesized, thereby supplying a substantial proportion of membrane lipids to the Golgi, the plasma membrane, and other organelles such as mitochondria[196]. Newly synthesized lipids are exported through secretory vesicles and cytoplasmic lipid transfer proteins[197]. It is noteworthy that, despite the extensive exchange of lipids between different organelles, various cellular structures display significant differences in their lipid composition[193,198,199].

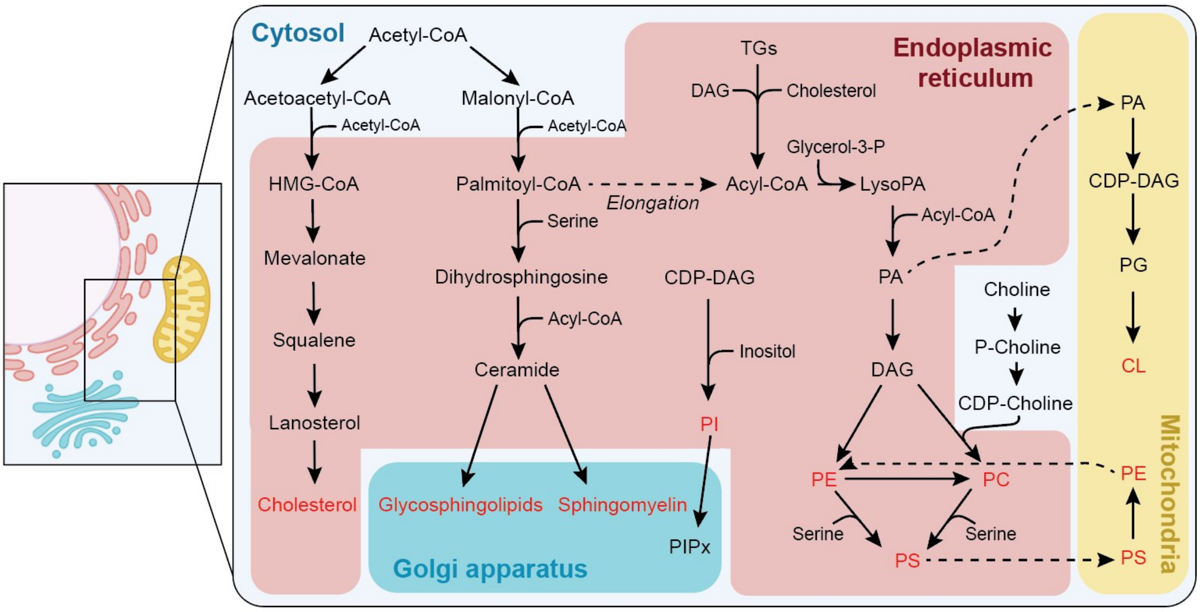

Figure 11. FA and lipid biosynthesis in the cell (adapted from Holthuis et al.[193]). Principal pathways for the production of FAs, cholesterol, sphingolipids and phospholipids in mammals. CDP-Choline: cytidinediphosphate choline; CDP-DAG: cytidine diphosphate-diacylglycerol: CL: cardiolipin; FA: fatty acid; HMG-CoA: hydroxymethylglutaryl coenzyme A (CoA); PA: phosphatidic acid; P-Choline: phosphocholine; PG: phosphatidylglycerol; PIPx: phosphoinositide; PC: phosphatidylcholine; PI: phosphatidylinositol; PE: phosphatidylethanolamine; PS: phosphatidylserine; TG: triacylglycerol.

Fatty acid biosynthesis and elongation: FAs can originate from either exogenous sources such as the diet, or from endogenous biosynthetic pathways within the cell. The cytoplasm and the ER membrane are the primary location for FA biosynthesis and elongation[200]. This process involves moving a FA-acyl-CoA molecule through a four-step cycle (reviewed in Kihara et al.[200]). The acyl-CoA molecule gains additional two carbon chain units in comparison to its original form upon the completion of one cycle. Mammals, including humans, possess the capacity to biosynthesize specific categories of FAs, such as saturated and some mono-unsaturated FAs[194,201]. However, long chain ω-3 and ω-6 PUFAs are considered to be essential, as they cannot be synthesized endogenously. They need to be either supplied from external sources like fish or vegetable oils or synthesized from externally derived FA precursors[202]. In humans, the elongation and desaturation of the precursor α-linolenic acid, generates the two main ω-3 fatty acids EPA and DHA. AAC, which is a ω-6 PUFA, is the primary product resulting from the precursor, linoleic acid. In the brain, plasma membranes of neural cells predominantly contain AAC and DHA[203,204]. Notably, the integration of ω-3 and ω-6 PUFAs and their precursors into lipids appears to follow organ- and stage-specific patterns. Sinclair et al.[205] monitored the integration of radioactively labelled linoleic acid, AAC, and DHA into liver and brain lipids of suckling and adult rats. In the liver, the provided PUFAs were mainly integrated into triglycerides, whereas in the brain, they were mostly incorporated into phospholipids. Importantly, the rate of incorporation into brain lipids in adult rats was considerably lower than that in pre-weaning rats, indicating an increased demand for phospholipid synthesis during this time period[205].

Glycerophospholipids: GPLs represent the most abundant lipid species in the brain and constitute a significant proportion of cell membranes (reviewed in Ziegler et al.[206]). This lipid class is named after its characteristic glycerol backbone that consists of three carbons. Typically, a hydrophobic saturated long-chain FA (palmitic or stearic acid) is attached to carbon 1 (C1). In the brain, a PUFA, such as DHA or AAC are preferentially attached to carbon 2 (C2)[207–210]. The third carbon, C3, is linked to a phosphate head group. The diverse modifications of the phosphate head group give rise to different subclasses of GPLs. The most abundant GPLs in the human brain are phosphatidylcholine (PC), phosphatidylserine (PS), phosphatidylethanolamine (PE), phosphatidylinositol (PI), lysophospholipids, phosphatidic acid (PA), and phosphatidylglycerol (PG)[211]. PC accounts for more than 50% of all GPLs in most eukaryotes, depending on the cell type and developmental stage. The ER is the main site of GPL *de novo* synthesis[212] (Figure 11). Its synthesis rate is a crucial check-point in global membrane homeostasis. Phospholipids are asymmetrically distributed in the plasma membrane, whereby in mammalian cells PC is predominantly located in the extracellular leaflet and PI and PS are primarily found in the inner leaflet. This uneven distribution of phospholipids has implications for the interactions between lipids and charged residues located in transmembranal fraction of channel proteins (see chapter 1.2.4.3)[210,213,214].

Sphingolipids and Cholesterol: In the brain, SLs and sterols are the other two most prevalent lipid classes. SLs are found in high abundance in the myelin sheaths of neurons (reviewed in Lamari et al.[212] and Hussain et al.[190]). Unlike GPLs, all SLs, such as sphingomyelins and glycosphingolipids have a unique structures[193]. They consist of a ceramide backbone, which is mainly linked to two saturated or unsaturated acyl chains, and a polar head group, which can have over 300 different structures[212]. The synthesis of SLs primarily takes place within the ER and commences with the incorporation of serine and palmitoyl-CoA (Figure 11).

Sterols, such as cholesterol, play a critical role in brain function during both developmental and adult stages[215]. Cholesterol regulates membrane fluidity[193]. The ER represents the principal site of cholesterol synthesis[215] (Figure 11). In the early stages of postnatal neurodevelopment, the majority of brain cholesterol is synthesized by oligodendrocytes to ensure proper myelination of neuronal axons[216]. The brain contains approximately 25% of the body's cholesterol[215], with the majority of it being present in the form of myelin[216,217].

1.2.4.2 Lipid storage

In the brain, lipid droplets (LDs) serve as specialized organelles for the storage of lipids or FAs (reviewed in Ralhan et al.[218]). LDs accumulate surplus FAs in the form of neutral lipids, such as triglycerides (TGs) or sterol esters[219,220]. Importantly, LD formation does not only serve as a bioenergetic reserve but also provides protection against lipotoxicity, a condition that may arises from accumulation of free FAs in the cytosol[221,222]. LDs are composed of a core of hydrophobic neutral lipids, which is enveloped by a phospholipid monolayer. Their biogenesis involves a range of cellular processes, including lipid biosynthesis at the ER, the budding of newly formed LDs, and their growth via further lipid intake. The formation of LDs is primarily triggered by a high exogenous lipid availability. However, they can also emerge under circumstances of nutrient deprivation, due to cells shifting their preferred energy substrate from glucose to high-energy FAs[223,224]. In response to hypoxia or increased oxidative stress, LDs play a protective role by serving as a buffer against lipid-mediated toxicity[222,225,226] .

1.2.4.3 FAs and lipids, regulators of cellular physiology

Membrane lipids, such as GPLs, and FAs serve as essential components not only in preserving the structural integrity of neural membranes, but also in laying the groundwork for an entire signaling cascade, ultimately modulating cellular activity and physiology[227]. Importantly, neural membranes consist not only of lipids but also of transmembrane and peripheral proteins. Binding of GPLs to these proteins is essential for their vertical positioning and tight integration within the lipid bilayer and therefore ensures optimal functioning of receptors, membrane-bound enzymes and **voltage-gated ion channels**[209,210,214]. Consequently, disruption of the GPL or FAs composition of plasma membranes can affect channel conformation and function by so called hydrophobic mismatches, where the transmembrane region of an ion channel does not match the FA tail of a neighboring GPL[228,229]. This phenomenon is also observed in connection with changes in membrane curvature[230].

A lipid class that is a key player in lipid-mediated signaling and regulation are phosphatidylinositol phosphates, or **PIPs.** In depth, a small fraction of the PI pool undergoes further phosphorylation leading to the formation of seven different PIPs. These lipids can serve as constitutive signals that define organelle identity[231] or can be hydrolyzed into second messengers that mediate acute responses[232]. One of the most important functions of PIPs in the brain is their role in synaptic transmission. PIPs help to regulate the activity of ion channels and transporters that are involved in the release and uptake of neurotransmitters[233,234]. PIPs also act as second messengers, relaying extracellular signals to the nucleus and modulating gene expression[235]. PIPs help to regulate the activity of cytoskeletal proteins, such as actin and myosin, and are involved in the formation and maintenance of the complex cytoskeletal structures that underlie neurite outgrowth and synaptic plasticity[236].

While it is well-established that the composition of cellular membranes can affect ion channel activity, recent evidence has demonstrated that lipid-derived factors, beyond the membrane composition itself, can also impact the conformation of voltage-gated ion channels. Especially, since ion channels are literally enclosed by precursors of lipid signalling, these channels are highly receptive to messages encoded by lipid mediators or free FAs. PUFAs are the FA class with the most significant regulatory potential in the brain. Among those FAs, DHA and AAC have been found to be particularly potent regulators of neuronal activity[194,209]. For instance, membrane shedding of PUFAs from GPLs is the main mode of regulating the availability of free FAs as second messengers[194,209]. Upon activation of specific G-protein coupled metabotropic receptors, membrane phospholipids undergo enzyme-mediated hydrolysis to liberate non-esterified free FAs. Once released, free PUFAs can be further metabolized to produce lipid mediators called eicosanoids, docosanoids or platelet-derived factor[227,237]. Furthermore, PUFAs themselves can modulate the activity of voltage-gated ion channels, with higher levels of free PUFAs generally associated with inhibition of Na+, Ca2+ and K+ currents[238–245], although increased K+ currents have been documented aswell[246,247].

FAs have a multifaceted role in biological processes. They are not only indispensable for lipid synthesis and signaling, or energy production but also for mediating post-translational modifications (PTMs) of proteins[248–250]. Various lipids or their derivatives such as sterols or phospholipids can covalently bind to proteins, thereby modulating their physical properties and affinities[251,252]. In the brain, the most common forms of **lipidation** are palmitoylation, myristoylation, and prenylation[253–256]. Palmitoylation involves the attachment of palmitate (a 16-carbon FA) to proteins at distinct residues[257]. This changes the proteins hydrophobicity, enabling it to associate more readily with hydrophobic lipid bilayers such as cell membranes or vesicles. Importantly, the reversibility of this modification renders it an important mechanism for modulating protein trafficking, membrane localization, and interactions[258,259]. Unlike myristoylation and prenylation, which typically occur co-translationally, palmitoylation is not necessarily coupled with protein translation[260]. As a result, proteins can be modified selectively in response to stimuli or in distinct cellular compartments. Due to these features palmitoylation serves as an essential protein modification process in the context of synaptic plasticity, ion channel gating and neurotransmitter receptor trafficking in neurons[256,261,262]. During neurodevelopment, palmitoylation of proteins plays a key role in the formation of axons and dendrites[249,263–265]. Moreover, it aids in the localization of proteins to the plasma membrane and facilitates movement of proteins between various cellular compartments during the plastic synaptic changes that occur in developing neuronal networks[249,266].

Importantly, all these examples of lipid-mediated signaling and modulation are not mutually exclusive. Altogether, they suggest a direct and complex mechanism how lipids fine-tune neuronal excitability and synaptic transmission. Disruption of the cellular lipid profile can trigger strong compensatory mechanisms, as lipid homeostasis is crucial for proper brain formation and cellular function[198,199,267].

1.3 Neurodevelopmental disorders

The term "neurodevelopmental disorders" (NDDs) encompasses a heterogeneous group of neurological conditions that result in deficits in cognition, communication, motor skills, and may be accompanied by seizures and neuroanatomical anomalies. A growing body of evidence suggests that these disorders share common underlying mechanisms that are linked to genetic or environmental insults, which disrupt molecular processes critical for brain development such as transcriptional control, protein synthesis, chromatin remodeling, cellular metabolism, and synapse formation and function[268–270]. Although these mechanisms are not exclusive to neural cells, these cell types are particularly vulnerable to their disruption during development. NDDs comprise a diverse range of neuropathological conditions including autism spectrum disorder (ASD), intellectual disability (ID), attention deficit/hyperactivity disorder (ADHD), epilepsy, and neuroanatomical malformations like microcephaly[271–274]. The etiology and clinical presentation of NDDs are multifaceted, and are characterized by varying degrees of severity and comorbidity.

1.3.1 Neuroanatomical malformations

In mammals, the formation of the six-layered neocortex during corticogenesis is achieved through a tightly regulated sequence of molecular and cellular events. These events can be broadly classified into three partially overlapping developmental phases: proliferation, migration, and post-migration. Importantly, a derailment of any of these developmental events may result in severe neurodevelopmental defects such as neuroanatomical anomalies. Pathological alterations in brain size such as a decrease of the occipitofrontal head circumference (HC) by 2 standard deviations (SD) below the mean for sex, age, and ethnicity, are referred to as **microcephaly**[273,275,276]. Depending on its timepoint of occurrence this condition is classified as congenital (before birth) or postnatal microcephaly (after birth)[272]. The underlying mechanisms of microcephaly are diverse. Abnormal NPC proliferation or neuronal migration defects are common causes of congenital microcephaly, while impairments in dendritic arborization, myelination, apoptosis, and some metabolic disorders often lead to postnatal microcephaly[272,273,277,278]. Contrarily, the term **megalencephaly** or **macrocephaly** (>2.5 standard deviations above the mean) is used to describe a diffuse or partial excess of cortical tissue, whereas **focal cortical dysplasia** refers to overgrowth restricted to one or two lobes[273,275]. Both of these conditions are often associated with a deregulation of NPC proliferation or neuronal differentiation[272]. **Lissencephaly** or **polymicrogyria** are other neuroanatomical defects characterized by absent or excessively wide gyri, along with cortical thickening and disorganization. These disorders are frequently related to defects in neuronal migration, thereby causing misplaced or ectopic neurons, sometimes even resulting in band or nodular heterotopia[273,275].

1.3.2 Autism spectrum disorder

Autism spectrum disorder (ASD) is a neurological condition characterized by deficits in communication and social interactions, as well as the presence of repetitive and restrictive behaviors and interests[279]. The term “autism” has first been used by Dr. Hans Asperger and Dr. Leo Kanner in the 1940s to describe a group of children with deficits in social behavior. Nowadays, the term has been replaced by the umbrella term "ASD," reflecting the heterogeneous symptomatic manifestations of the disorder[280,281]. Individuals diagnosed with ASD display varying degrees of deficits in social interactions and non-verbal and verbal communication, and often present with restrictive and repetitive behaviors, including the usage of stereotyped speech or movements. Sensory processing abnormalities are also frequently observed in individuals with autism[282]. The prevalence of ASD is high, with 1 in 44 children in the US aged 8 years estimated to be diagnosed with an ASD[283]. Diagnosis of ASDs can be challenging especially due to late manifestations of the disorder and high comorbidity with other neurological impairments, such as ID (35-40%)[284] and epilepsy (20-25%)[285]. The etiology of ASD is multifactorial, with both genetic and non-genetic factors potentially disrupting neurodevelopmental processes, such as synapse formation and function, chromatin remodeling, and protein synthesis[282,286].

1.3.3 Epilepsy

Epilepsy is a neurological disorder characterized by a persistent susceptibility to generate spontaneous seizures as a result of abnormal or excessive neuronal activity in the CNS[287,288]. The etiology of epilepsy is highly diverse, ranging from known genetic or environmental incidents such as trauma or tumors, to idiopathic causes[289].

Epilepsy patients are commonly classified according to their “seizure type”, “epilepsy type”, “etiology”, and “epilepsy syndrome” [290]. The prevalence of epilepsy is relatively high, affecting approximately 50 million individuals according to the World Health Organization (WHO)[291]. The primary treatment strategy for epilepsy consists of anti-epileptic drugs (AEDs). However, one-third of epilepsy patients present with seizures refractory to pharmacotherapy[292]. Other treatment options in this case include epilepsy surgery, which involves the removal of the affected brain area, or ketogenic diet, a high-fat - low-sugar diet, both of which have been successful in alleviating seizures in certain subsets of epilepsy patients[292].

1.3.4 Etiology of NDDs

NDDs are a collection of complex neurological conditions that share underlying pathophysiological mechanisms, including the disruption of signaling pathways crucial for normal brain development. The etiology of NDDs is multifactorial, and a broad range of genetic and environmental factors have been implicated, such as nutritional deficiencies, maternal infections, birth complications, trauma, chemicals, genetic mutations, and metabolic disorders[274,286,293]. The specific timing of the disruptive event plays a crucial role in determining which neurodevelopmental processes are affected. Prenatal insults tend to interfere with processes such as NPC pool formation, cell cycle progression, neuronal migration, or DNA damage response, while postnatal insults can affect neuronal arborization, synaptogenesis, gliogenesis, or myelination[270,271,274,294,295]. Some NDDs may also have a neurodegenerative component.

Due to the complexity of NDDs, investigating the various etiologies and their contribution to the pathology of the disorders is challenging, especially given the large number of high-risk loci involved and the dynamic interplay between genes and the environment throughout developmental processes.

1.3.4.1 Genetic causes of NDDs

Studying NDD high-risk genes, or disease-causing genetic variants, has not only become a powerful tool in understanding the complex etiology and phenotypical variability of these disorders, but also to elucidate shared underlying mechanisms and to identify potential entry points for treatments[270]. However, investigating the genetics of NDDs is challenging. For instance, a human genome acquires 100-200 new mutations from one generation to the next[296]. So, which factors determine if a genetic variant is actually disease causing? The two main principles that influence the genetics of NDDs are "gene vulnerability" and "mutational load." (reviewed in Parenti et al.[294]). The term **gene vulnerability** refers to the competence of a gene to tolerate mutational events[294]. Many NDD high risk genes are haploinsufficient and are characterized by a strong dosage sensitivity. In this case one single monoallelic disruptive event bears a significant disease risk[297]. These rare variants therefore present with a high gene vulnerability. However, phenotype-genotype correlation studies have shown that the patients' phenotypical representation can vary despite the presence of a comparable variant[298,299]. The underlying cause for this variability is not yet fully understood. Further, it has become clear that not only rare but also common genetic variants with low disease risk hold the potential to interfere with typical neurodevelopmental processes (reviewed in Mullins et al.[300]). Variants located in less sensitive locis are not exposed to strong selective pressure and can accumulate over generations, leading to cumulative effects that disturb neurodevelopmental trajectories. This phenomenon is referred to as **mutational load**[297,301,302]. Importantly, the mutational load can be derived from a combination of germline and somatic mutational events, known as the **two-hit model**[294].

In the context of monogenic NDDs, the majority of high-risk genes are associated with a limited set of cellular functions that are crucial for brain development, including transcriptional regulation, protein synthesis, and synaptic function. Another significant proportion of high-risk loci in NDDs are genes encoding key metabolic components. For instance, metabolic NDDs often involve disruptions in the switch from anaerobic glycolysis to OXPHOS, which is a critical step in neuronal maturation. In Leigh syndrome (LS) and mitochondrial encephalopathy lactic acidosis and stroke-like episodes (MELAS), mutations in components of the ETC lead to systemic ATP depletion and a compensatory upregulation of glycolytic pathways thereby causing hyperlactatemia, seizures, and increased patient lethality[303,304]. This shift from OXPHOS to glycolysis is associated with neuronal cell identity instability and a block of maturation[109,305].

Other neurometabolic disorders are caused by an accumulation of certain metabolites due to their increased production or decreased clearance[306]. For instance, phenylketonuria is a disorder that arises from mutations in a phenylalanine-degrading enzyme (PAH), leading to elevated systemic levels of the AA phenylalanine, and resulting in severe ID and psychiatric disorders[85]. Similarly, the accumulation or depletion of BCAAs, including leucine, isoleucine, and valine, contributes to severe neuropathologies. Autosomal recessive mutations in the genes that encode the Branched-chain ketoacid dehydrogenase (*BCKDH*) complex, who is the primary driver of BCAA catabolism, lead to a neurological syndrome known as Maple-syrup urine disease (MSUD)[307,308]. Mutations affecting this complex result in excessive amounts of BCAAs and their derivatives (BCKAs) in the tissue and serum of patients, causing severe neurological dysfunction, acidemia, and increased mortality[307,308]. Likewise, chronically decreased levels of BCAAs have been demonstrated to have deleterious effects on brain development. Patients carrying autosomal recessive mutations in the enzyme Branched-chain ketoacid dehydrogenase kinase (*BCKDK*), which is responsible for phosphorylation-mediated inactivation of the BCKDH complex, present with autism, epilepsy, ID, and microcephaly. Bi-allelic mutations in BCKDK lead to a continuously active BCAA catabolic pathway, resulting in chronically low BCAA serum levels in patients[309]. Similarly, homozygous missense mutations in the primary BCAA transporter of the brain, *SLC7A5*, have been linked to autism, epilepsy, and microcephaly, further emphasizing the significance of adequate BCAA supply for brain development[310]. Notably, many of these neurometabolic disorders are treatable to some extent. Dietary interventions, such as a restriction or supplementation of AAs, have been shown to alleviate many symptoms in patients with mutations in *BCKDH*, *BCKDK*, or *PAH*[311–315].

1.3.4.2 Extrinsic factors

Brain formation is primarily governed by genetic instructions, which follow a predetermined "clock-like" schedule that operates independently of external factors to achieve a consistent outcome in terms of structure and function across individuals[293]. However, the environment also plays a crucial role in shaping neurodevelopmental processes, particularly during critical periods of network formation trough a mechanism termed plasticity. This allows experiences to refine the brain circuitry to adapt to the unique environmental factors of each individual[274,316]. While this interplay between genes and environment is essential for normal neurobehavioral development, disruptive environmental factors can lead to aberrant neurodevelopment. A wide range of external stressors, such as environmental toxins, drugs, radiation, infection, and malnutrition, have been implicated in the etiology of NDDs.

Chemicals, including heavy metals[317,318], various classes of pesticides[319–321], and phthalates[322], possess high levels of neurotoxicity. Exposure to these teratogens during early fetal development can significantly impair brain formation at doses lower than those affecting adult brain function[323]. Similarly, prenatal exposure to alcohol is associated with fetal alcohol spectrum disorder (FASD), a disorder with a robust neuropathological component. The pathological effects of alcohol vary based on the duration and time point of exposure[324]. FASD is associated with developmental delay, caused by disruption of gene expression and epigenetic mechanisms involved in key cellular processes such as proliferation, migration, and differentiation[325–327]. In addition to these effects, alcohol exposure can also alter synaptic plasticity by blocking NMDA receptors and modulating GABA-a receptors[328,329]. In newborn rats, alcohol has been shown to abolish gamma oscillations and spindle burst during the postnatal time window of PCD leading to an increased surge of apoptosis in the developing neocortex[330]. Similarly, exposure to anesthetics and anticonvulsants (such as midazolam and isoflurane) during early postnatal periods has been found to induce long-term anatomical, behavioral, and cognitive impairments[331–333], due to their modulation of GABA and NMDA receptor function. Postnatal exposure to these compounds can cause cortical atrophy by impairing postnatal spontaneous network activity and PCD[24,334,335].

In addition to exposure to chemicals and drugs, **maternal viral infections**, such as West Nile virus, cytomegalovirus, Zika virus, rubella, and herpes simplex virus infections[336–341] have been associated with severe neuroanatomical malformations, particularly when the infection occurs during the first trimester of pregnancy[342] .

Maternal nutrition during pregnancy has also been identified as a potential factor in the development of neuropathological outcomes[293,343,344]. Inadequate fetal nutrient supply, including vitamins (folate, B12, vitamin A, vitamin E, vitamin D, and vitamin K), micronutrients (iodine, iron, copper, creatine, choline, zinc,), and macronutrients (FAs, proteins, and carbohydrates), is linked to various neurodevelopmental and neuropsychiatric disorders, including alterations in brain structure and function, behavioral deficits, and cognitive impairments. Deficiencies in specific nutrients during critical periods of brain development can cause long-term neuropathologies, such as impaired neural cell proliferation and differentiation, reduced fetal tissue growth rates and impaired protein synthesis and bioenergetic pathways due to insufficient carbohydrate or AA intake[345,346]. Additionally, decreased maternal protein intake leads to a decline in FA levels in the fetal brain due to reduced maternal lipid availability[347]. The molecular mechanisms underlying these effects are not yet fully understood. Similarly, impaired lipid metabolism and availability of FAs have been implicated in the etiology of NDDs[348–350]. PUFAs, such as DHA, are particularly critical for brain development mainly from the third trimester to early childhood since they are involved in neuronal membrane formation, energy production, synaptogenesis, dendritic growth, and myelination[346,347,351–353]. However, excessive levels of maternal PUFAs in rodents have also been associated with negative outcomes, including decreased hippocampal neurogenesis and behavioral alterations in the offspring[347,354].

1.3.4.3 Gene x environment interactions

A range of environmental stressors such as smoking, maternal stress, infections, and trauma have been identified as potential risk factors for neuropathologies[336]. However, studies in both, humans and rodents have demonstrated substantial inter-individual variability in the susceptibility to these environmental factors, with exposure not consistently resulting in neuropathological outcomes[355]. To explain this variability, the concept of "genetic moderation" has been introduced, which suggests that differences in genetic background, including mutational load, determine an individual's level of resilience or vulnerability to environmental stressors[355,356]. These gene x environment interactions (G x E) have been proposed as a potential explanation for a significant proportion of idiopathic NDD cases[356,357]. This concept adds further complexity to our understanding of NDD etiology by suggesting that neuropathological outcomes are not solely determined by the period, duration, and frequency of exposure to disruptive insults, but also by the degree of an individual's susceptibility, determined by their genetic background[358]. Despite their complexity, studying G x Es does not only provide an opportunity to reveal the underlying pathological mechanisms of subsets of NDDs, but also to identify those who are susceptible to developing these disorders in response to known environmental stimuli, thereby enabling the initiation of preventive or more targeted therapies[358].

2 Results

2.1 Metabolome profiling reveals distinctive metabolic states of the cerebral cortex across development

Human cortical development entails the timely coordination of a number of critical steps that are devised to generate a precise range of correctly positioned and functionally integrated neuronal cells. These steps are guided and regulated by a network of genes whose mutations can underlie neurodevelopmental and neuropsychiatric disorders[294]. Challenging environmental conditions may also account for pathological variations of neurodevelopment but the identification of such factors is complicated and less understood[344,359–361]. Genetic conditions, however, offer tractable entry points to isolate some of the extrinsic factors influencing the assembly of the brain.

We recently identified mutations in the gene *SLC7A5,* encoding a large neutral amino acid transporter (LAT1), as a rare cause of autism spectrum disorders[310]. Most of the LNAAs are essential; thus, their presence in the human body depends on dietary intake. However, it remains largely unknown if and how the level of these AAs changes over time in the brain and how fluctuations in their amount may influence the course of neurodevelopment. In fact, despite its importance, little is known about the metabolic program unfolding during brain development and the specific nutrient dependencies that this entails. For example, we know that neural progenitor cells (NPCs) mainly rely on anaerobic glycolysis (Figure 12A - left)[107,362]. In contrast, mature neurons meet their ATP demand through oxidative phosphorylation (Figure 12A - right), but due to their high energy requirement and their inability to store glycogen[123,124], they rely on astrocytes to provide metabolic support[42,47]. However, it is unknown how maturing neurons meet their energy demand at intermediate developmental stages when they lack full glial support (Figure 12A - middle).

To gain an understanding of the metabolic states and transitions occurring during brain maturation, we analyzed the metabolome of the wild-type mouse cerebral cortex obtained at three different time points: embryonic day 14.5 (E14.5), postnatal day 2 (P2), and postnatal day 40 (P40). These time points coincide with different feeding strategies and are enriched for neural cells in different states: NPCs and immature (E14.5), maturing (P2), and mature (P40) neurons (Figure 12A). By employing two independent High-Performance Liquid Chromatography (HPLC) detection strategies (see Star-Methods), we quantified 346 metabolites. Principal component analysis (PCA) of the results separated the samples based on sampling age (Figure 12B), indicating that the cerebral cortex at each of these three time points is in a distinct metabolic state. The metabolic reorganization of the developing cortex is extensive, with the level of 273 out of 346 metabolites changing over time (Figure 12C-C'). The variability across animals of the same age was small (Figure S1A), indicating that the observed changes are tightly regulated. Compared to E14.5, at P2, the level of 137 metabolites is significantly decreased and that of 60 increased (Figure 12C). At P40, 202 metabolites show a different level than at P2, with an approximately equal number of metabolites showing increased or decreased levels (Figure 12C'). Enrichment analysis revealed an overrepresentation of purine- and pentose phosphate-related metabolites among those increasing at P2 (compared to E14.5) and enrichment of AA-related metabolites among those decreasing (Figure 12D). At P40, we detected a substantial increase in glutamine and glutamate-related metabolites and a decrease in a different set of AAs (Figure 12E), disclosing a stage-specific regulation of AA metabolism. To better understand the quality of those changes over time, we plotted the developmental trajectories of the detected metabolites (Figure S2 grey trajectories, Supplementary data 1). Employing a Gaussian mixture model (GMM), we clustered all measured metabolites based on their time trajectories. Next, focusing on KEGG annotated metabolites (n=179) (Figure 12F), we assessed whether different trajectory-related groups were enriched for particular classes of metabolites (Figure 12G, Supplementary data 2). This analysis revealed a predictable enrichment for neuroactive and cAMP signaling pathways in the cluster representing metabolites with ascending trajectories over time (Cluster 1, Figure 12F-G), with the majority of the metabolites steeply increasing between P2 and P40. Furthermore, we found that cluster 5, comprising metabolites with declining trajectories over time, is enriched for branched-chain AAs (BCAAs) and BCAA-related metabolites (Figure 12F-G). This cluster sparked our interest since BCAAs are substrates of the SLC7A5 transporter. The decline over time of these and a few other AAs (i.e., Figure S2; grey trajectories, metabolite (M) 016, M017, M030, M062, M086) could indicate either a decreasing brain intake or an increasing utilization by neural cells as they mature. Either way, this observation further suggests that neural cells have distinctive AA demands at different developmental stages. Finally, the only other cluster enriched for specific classes of metabolites is cluster 3, which displays a drop in glycerophospholipid- and arginine-related metabolite levels, specifically at P2 (Figure 12F-G).

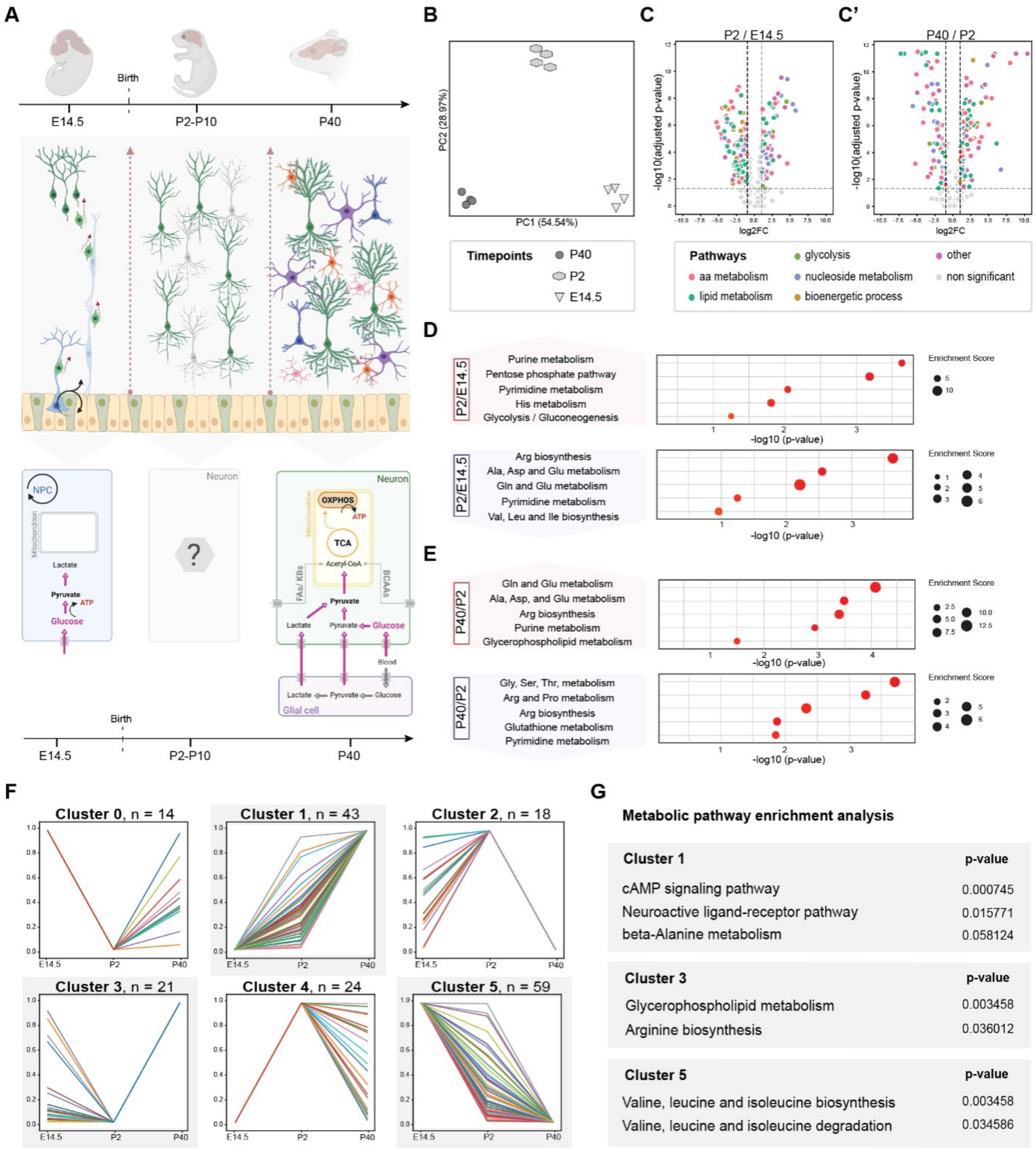

Metabolic pathway enrichment analysis

Cluster 1	p-value
cAMP signaling pathway	0.000745
Neuroactive ligand-receptor pathway	0.015771
beta-Alanine metabolism	0.058124

Cluster 3	p-value
Glycerophospholipid metabolism	0.003458
Arginine biosynthesis	0.036012

Cluster 5	p-value
Valine, leucine and isoleucine biosynthesis	0.003458
Valine, leucine and isoleucine degradation	0.034586

Figure 12. Metabolome profiling of the forebrain across time highlights developmental stage-specific metabolic states. (**A**) Schematic description of ATP synthesis strategies in the cortex at different developmental stages. **Top left**: At E14.5, neural progenitor cells (NPCs) produce intermediate progenitors and migrating immature excitatory neurons, generating the different cortical layers. **Bottom left**: For ATP synthesis, NPCs rely on anaerobic glycolysis, a cytoplasmic biochemical process converting glucose into lactate. **Top middle**: Perinatally, the cortical network, mainly consisting of maturing excitatory and inhibitory neurons, undergoes significant refinement. Glial cells are detectable but immature. **Bottom middle**: The metabolic landscape of maturing neurons is largely unknown. **Top right**: A mature cortical network, including pyramidal (green), inhibitory neurons (blue) and glial cells (astrocytes (purple), oligodendrocytes (orange) and microglia (pink)). **Bottom right**: Mature neurons utilize glucose to produce ATP via aerobic glycolysis. Since endogenous pyruvate is insufficient to

meet energy demand, neurons depend on metabolic support by glial cells (TCA = tricarboxylic acid cycle, OXPHOS = oxidative phosphorylation). (**B**) Principal component analysis of the metabolome of E14.5, P2 and P40 wild-type mouse cortices. (**C-C'**) Volcano plots showing differentially abundant metabolites across developmental stages. (**D-E**) Metabolic pathway enrichment analysis of all significantly up- (red) or down-regulated (blue) metabolites at P2 compared to E14.5 (**D**) and P40 compared to P2 (**E**). (**F**) Clustering of all metabolites based on their trajectory over time; (x-axis: age; y-axis: scaled abundance). (**G**) Metabolic pathway enrichment analysis (Supplementary data 2) revealed an overrepresentation of metabolites related to 'cAMP signaling pathway' (*p<0.00075; adj-p<0.021*), 'beta-Alanine metabolism' (*p<0.059; adj-p<0.4*) and 'Neuroactive ligand-receptor pathway' (*p<0.016; adj-p<0.22*) in cluster 1. Cluster 3 is enriched for 'Glycerophospholipid metabolism' (*p<0.013; adj-p<0.24*) and 'Arginine biosynthesis' (*p<0.037; adj-p<0.25).* Cluster 5 is enriched for 'Valine, leucine and isoleucine biosynthesis (*p<0.0035; adj-p<0.22*) and - degradation' (*p<0.035; adj-p<0.89*). See also Figure S1 and S2.

2.2 Perturbation of LNAA uptake leads to perinatal disruption of lipid metabolism

Knowing that the level of BCAAs and BCAA-related metabolites changes during brain maturation, we investigated the consequences of limiting BCAA supply to neural cells. Therefore, we ablated *Slc7a5*, the main LNAA transporter, in these cells. Indeed, although Slc7a5 has been described as a BBB transporter[310], we found that, in the cerebral cortex, it is also expressed in excitatory neurons and glial cells of all layers, particularly perinatally (Figure 12A-C' and S1B-C), coinciding with the time window displaying a drop in BCAA levels (Figure 12F-G - cluster 5). In addition, while patients with *SLC7A5* mutations present with microcephaly, the deletion of *Slc7a5* from the BBB in mice (*Slc7a5*$^{fl/fl}$;*Tie2*-Cre positive (+) mice) does not lead to a reduction in brain size[310]. This suggests a function of *SLC7A5*, and its substrates, in cell types other than the endothelial cells of the BBB. Thus, we crossed floxed *Slc7a5* mice (*Slc7a5*^{fl}) with *Emx1*-Cre animals. *Emx1*-Cre mice express the Cre recombinase in the radial glial cells of the dorsal telencephalon from E9.5 onwards[363], thereby inducing *Slc7a5* deletion in NPCs and their progeny, including the excitatory neurons of the neocortex and hippocampus as well as in the glial cells of the pallium (Figure 13A and Figure S1D), but not in the endothelial cells of the BBB (Figure 13C'). Next, we analyzed the metabolome of the cerebral cortex of *Slc7a5*$^{fl/fl}$;*Emx1*-Cre+ mice over time and compared it to that of wild-type animals. This approach allowed us to resolve i) the cause of the drop in LNAAs (particularly BCAAs) observed in P2 wild-type cortical lysates (Figure S2, grey trajectories M016, M017, M030, M062, M086) and ii) the impact of deregulating these AAs on the metabolism of the cerebral cortex. The effect of *Slc7a5* deletion on the overall metabolite profile is relatively minimal (Figure S1E).

To investigate whether *SLC7A5* mutations affect specific groups of metabolites, we performed an enrichment analysis of the KEGG-annotated metabolites showing divergent temporal trajectories ($r < 0.975$) in mutants and controls (Figure 13D-H, Figure S2, Supplementary data 1). As expected, this analysis identified the pool of AAs transported by Slc7a5, grouped into the term 'Aminoacyl-tRNA biosynthesis' (Figure 13G), as the major class of affected metabolites in mutant animals. However, the deletion of *Slc7a5* alters the levels of these AAs in cortical tissue only at P2 (Figure 13H), indicating a function of Slc7a5 in neonatal mice.

Furthermore, the level of these AAs is higher, not lower, in mutants compared to controls (Figure 13H), suggesting that in the absence of Slc7a5, the LNAAs accumulate in the extracellular space and are not consumed by neural cells (Figure 13I). To test this possibility, we quantified AAs in neural cells isolated from P2 control and mutant cortices (Figure 13J), thereby measuring their intracellular amount. Indeed, the levels of the primary Slc7a5 substrates are significantly reduced in mutant cells. In contrast, the level of histidine, the counter AA[364], is increased (Figure 13K). Thus, the lack of Slc7a5 at P2 impairs the transport of LNAAs into neural cells resulting in their net decreased consumption. These results also indicate that the drop in AA levels observed in P2 control samples (Figure 13H) reflects an increased utilization by neural cells.

Although the BCAAs are a source of Acetyl-CoA, an essential compound for the TCA cycle[365], we observed only a very mild reduction in the levels of some of the energy storage- and transfer-related metabolites (Figure S3A-F), suggesting compensatory mechanisms. Indeed, while a derailment of energy homeostasis has been associated with increased levels of oxidative stress[366–368], the ratio between reduced and oxidized Glutathione was not altered in *Slc7a5* mutant cells (Figure S3G). Further, the decrease in intracellular LNAAs does not lead to defects in AA sensing- and protein synthesis pathways, such as the mTOR, the Adenosine monophosphate-activated protein kinase (AMPK), or the unfolded protein response (UPR) signaling cascades (Figure S4)[181,182,369–372].

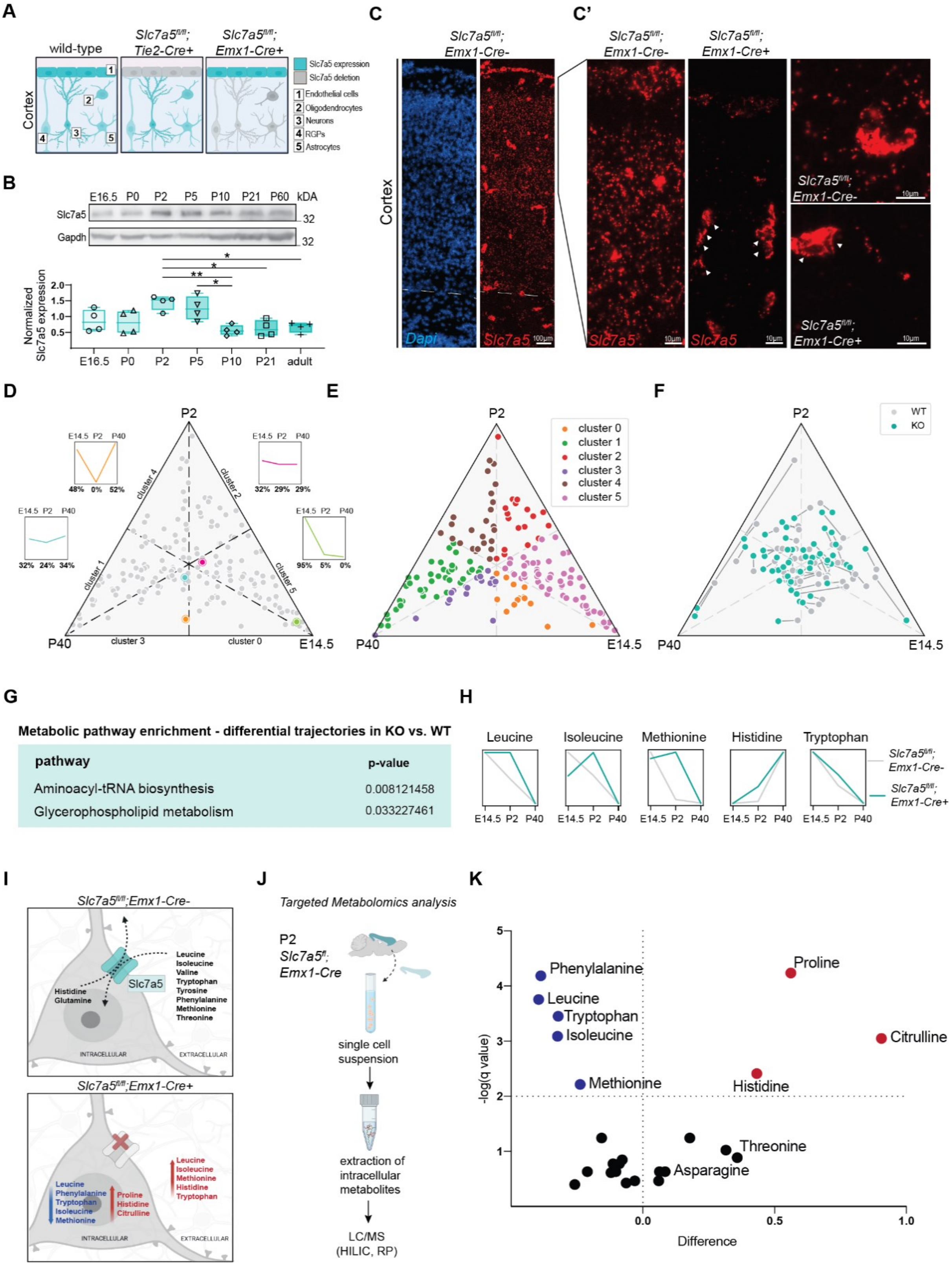

Metabolic pathway enrichment - differential trajectories in KO vs. WT

pathway	p-value
Aminoacyl-tRNA biosynthesis	0.008121458
Glycerophospholipid metabolism	0.033227461

Figure 13. The neonatal metabolic state is dependent on *Slc7a5* expression. (**A**) *Slc7a5* expression in the cerebral cortex of wild-type (**left**), *Slc7a5$^{fl/fl}$;Tie2-Cre+* (**middle**) or *Slc7a5$^{fl/fl}$;Emx1-Cre+* (**right**) mice. (**B**) Gapdh-normalized Slc7a5 levels in cortical samples obtained from *Slc7a5$^{fl/fl}$;Tie2-Cre+* animals across development (n = 4 mice per genotype per time point; **p<0.05; **p<0.01;* unpaired two-tailed *t*-test)**.** (**C-C'**) *Slc7a5* mRNA expression in P2 murine wild-type somatosensory cortex (SSCtx)(**C-C'** (**left**)). In *Slc7a5$^{fl/fl}$;Emx1-Cre+* SSCtx (**C'** (**right**))**,** *Slc7a5* expression is preserved at the BBB (arrows). (**D-F**) Ternary plot classification of metabolites in

wild-type and mutant cortex. (**D**) The localization of each metabolite (dot) within the ternary plot is determined by its previously determined cluster affiliation (Figure 1F) and its exact unscaled trajectory, defined as the ratio between the three time points. (**E**) Ternary plot of KEGG-annotated metabolites in wild-type mice. (**F**) Compared to controls (grey dots), mutants display changes in the trajectory of some metabolites (cyan dots). (**G**) Metabolic pathway enrichment analysis of the KEGG-annotated metabolites displaying an altered trajectory in mutants (Supplementary data 2). (**H**) Stage-specific accumulation of Slc7a5 substrates in *Slc7a5*$^{fl/fl}$*;Emx1-Cre*+ cortical tissue (n=4 animals per genotype per time point; Pearson's coefficient: Supplementary data 1; x-axis : age; y-axis: scaled abundance). (**I**) Slc7a5 facilitates the flux of BCAAs and LNAAs across the neuronal membrane (**top**). Loss of *Slc7a5* causes extracellular accumulation and intracellular depletion of LNAAs (**bottom**). (**J**) Experimental workflow of the targeted intracellular metabolomic analysis. (**K**) Volcano plot of the AAs measured in *Slc7a5* mutant and control cells. AAs showing significantly lower (blue) or higher (red) levels in *Slc7a5*$^{-/-}$ cells are indicated (n = 7 per genotype; FDR cut-off: 1%). See also Figure S1 and S2.

However, we found that loss of *Slc7a5* in neurons affects the levels of metabolites related to 'glycerophospholipids' (Figure 13G). Specifically, a PCA of all the detected lipid-related metabolites disclosed that while at E14.5 and P40 mutant and control samples cluster together, P2 samples separate by genotype (Figure S3H), thereby suggesting a time point-specific alteration in lipid composition due to the loss of *Slc7a5*. But how are BCAA and lipid metabolism linked? To better comprehend how a change in BCAA levels can disturb lipid metabolism, we first identified the exact lipid classes affected by *Slc7a5* deletion. Thus, we performed a comparative untargeted lipidomic analysis of P2 *Slc7a5*$^{fl/fl}$;*Emx1*-Cre+ and *Slc7a5*$^{fl/fl}$;*Emx1*-Cre- cortical tissue and dissociated cells (Supplementary data 3). These analyses revealed a specific reduction of glycerophospholipids (GPLs) in mutant cortical cells, along with an increase of triacylglycerols (TGs) in *Slc7a5* deficient cortical tissue (Figure 14A-B). Members of the GPLs are the main components of the phospholipid bilayer of biological membranes[193]. TGs, on the other hand, account for the majority of dietary fats and represent a way to store energy[373]. Sites of TG synthesis and storage are the liver and adipose tissue[374,375] but they can be mobilized rapidly in case of energy or fatty acid (FA) demand by the brain[187,376]. To determine if detected alterations are specific to any cell type, we compared our results with a dataset of human cortical cell type-specific lipids[189]. Interestingly, several of the lipids differentially abundant in Slc7a5 mutants are neuron-enriched, while astrocyte-enriched lipids are not affected in mutants (Figure 14C).

Next, to uncover the molecular mechanisms underlying the alterations in the cortical lipid profile, we performed a comparative proteomic study of perinatal control and mutant cerebral cortices (Figure 14D and S3I). We identified 1202 proteins deregulated in mutant samples, comprising 954 up-regulated and 248 down-regulated proteins in the *Slc7a5$^{fl/fl}$;Emx1-Cre+* cortex (Figure 14D). Gene Ontology (GO) enrichment analysis returned proteins involved in lipid metabolism as being the most significant and numerous among the up-regulated proteins (Figure 14E - right), while among the down-regulated GO-terms, we found an enrichment for neuron projection and membrane-associated proteins (Figure 14E – left; Supplementary data 4). Those GO-terms were reproducible at the mRNA expression level (Figure S3J, Supplementary data 5) and linked to the reduction of GPLs[210] (Figure 14A-B). Next, to indentify potential direct interaction partners of Slc7a5 we performed a proteomics analysis of a co-immunoprecipitation experiment of the transporter exclusively from the membranes of cortical neural cells. The analysis confirmed the known interaction of Slc7a5 with Slc3a2[159]. Additionally, we indentified two novel interaction partners, which are Vac14, a endo-lysosomal protein involved in PtdIns(3,5)P-phosporylation[377–379], and Ide, the enzyme responsible for insulin breakdown[380–382]. This experiment further excluded interactions with components of the B1/B3 integrin pathway[383] (Supplementary data 6).

Finally, to identify the connection between BCAA and GPL metabolism, we integrated the proteomic, lipidomic and metabolomic results focusing on potential convergent pathways (Figure 14F). Via this integration, we recognized that *Slc7a5* mutant cells, probably due to the shortage of BCAAs, prioritize mitochondrial BCAA catabolism, part of the ATP production machinery, over cytoplasmic BCAA catabolic reactions (i.e., Bcat2 vs. Bcat1; Figure 14F). Most importantly, about half of the enzymes involved in BCAA metabolism in the mitochondria are also involved in FA beta-oxidation, thereby disclosing a molecular overlap between BCAA and lipid catabolism (Figure 14F). The reduction of the intracellular BCAA levels leads to a compensatory upregulation of several of these shared enzymes (e.g., Acaa2, Acadm, Echs1), thereby increasing FA beta-oxidation and causing a drop in FAs. These results suggest that neurons at the perinatal stage rely on BCAAs as substrates for ATP production (Figure S3K). In their absence, FAs are redirected from GPL synthesis into beta-oxidation (Figure 14F). The observed increase in tissue TGs reflects the increased demand for FAs to support beta-oxidation and ATP production. Indeed, the increase of TGs in mutant cortical tissue is accompanied by the upregulation of Gcn2 and Apob. Gcn2 is a kinase acting as a sensor for intracellular BCAA levels[384]. Low levels of BCAAs induce Gcn2 autophosphorylation, resulting in the inhibition of its protein turnover[385,386].

Interestingly, Gcn2 has also been involved in the mobilization of TGs from fat storage in response to brain energy demand[376,387]. Apob constitutes the primary lipoprotein transporting dietary lipids across tissues[388]. Finally, *Slc7a5* mutants also show an increased level of Bckdk, a regulator of the BCAA catabolic pathway also implicated in the phosphorylation of cytoplasmic Acl, a key enzyme in citrate-based lipogenesis[185].

These findings suggest an increased perinatal dependency of neural cells on LNAAs. Decreased availability of these AAs reveals a direct link between BCAAs and lipid metabolism in the brain.

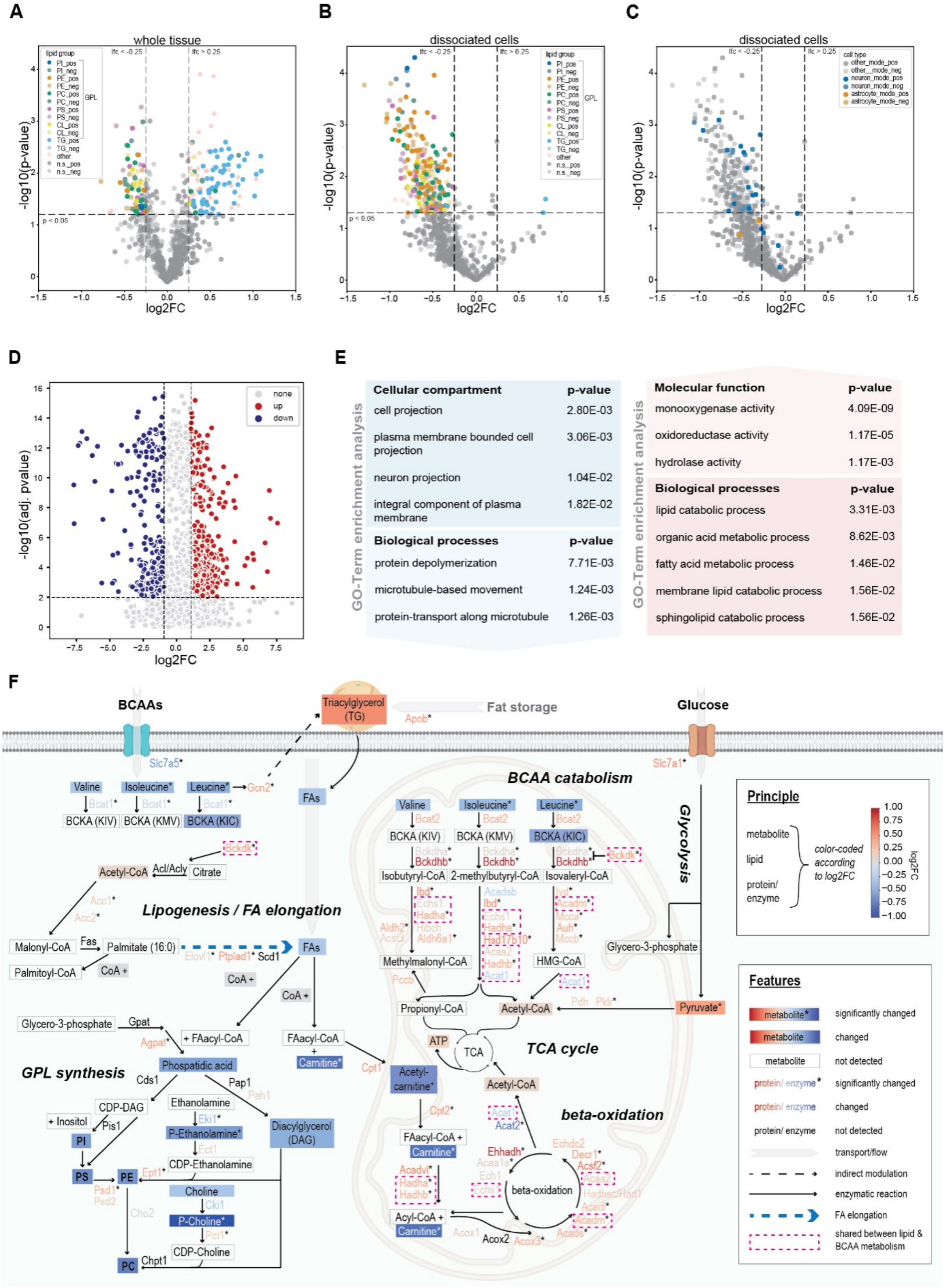

Cellular compartment	p-value
cell projection	2.80E-03
plasma membrane bounded cell projection	3.06E-03
neuron projection	1.04E-02
integral component of plasma membrane	1.82E-02

Biological processes	p-value
protein depolymerization	7.71E-03
microtubule-based movement	1.24E-03
protein-transport along microtubule	1.26E-03

Molecular function	p-value
monooxygenase activity	4.09E-09
oxidoreductase activity	1.17E-05
hydrolase activity	1.17E-03

Biological processes	p-value
lipid catabolic process	3.31E-03
organic acid metabolic process	8.62E-03
fatty acid metabolic process	1.46E-02
membrane lipid catabolic process	1.56E-02
sphingolipid catabolic process	1.56E-02

Figure 14. BCAA deprivation alters neuronal lipid metabolism. (**A-B**) Volcano plots of deregulated lipids in *Slc7a5* mutant cortical tissue (**A**) and dissociated cells (**B**). Lipids showing significantly lower or higher levels are color-coded according to their annotated class (PI: Phosphatidylinositol, PE: Phosphatidylethanolamine, PC: Phosphatidylcholine, PS: Phosphatidylserine, CL: Cardiolipin, TG: Triacylglyerol; _pos= detected in positive mode; _neg: detected in negative mode; n = 5 per genotype; p-value cut-off: 0.05; Supplementary data 3). (**C**) Same plot

as in (**B**) with neuron-enriched (blue) or astrocyte-enriched lipids (orange) highlighted (Supplementary data 3). (**D**) Volcano plot of proteins deregulated (1% False Discovery Rate cut-off) in the P5 *Slc7a5*$^{fl/fl}$*;Emx1-Cre*+ cortex. (**E**) GO-term enrichment analysis of up- and down-regulated proteins at 2% FDR (Supplementary data 4). (**F**) Integration of the proteomic, metabolomic and lipidomic data of P2 cortical tissue and cells. The schematic depicts enzymes associated with the metabolic pathways: "BCAA catabolism", "FA degradation" (beta-oxidation), "FA synthesis/elongation", "glycolysis" and "glycerophospholipid synthesis". Changes in expression or abundance due to *Slc7a5* depletion are color-coded (blue: decreased; red: increased; *$^*p < 0.05$). Enzymes shared by the BCAA and FA pathways are highlighted by a dashed rectangle. See also Figure S3 and S4.

2.3 Lack of the AA transporter SLC7A5 leads to stage-specific neuronal cell loss

Can the perinatal metabolic shift displayed by *Slc7a5* mutant neural cells explain some clinical issues reported in patients? *Slc7a5*$^{fl/fl}$;*Emx1*-Cre+ mice are born at Mendelian ratios, are viable and at birth do not display obvious growth defects compared to their wild-type littermates (i.e., *Slc7a5*$^{fl/fl}$;*Emx1*-Cre- or *Slc7a5*$^{fl/+}$;*Emx1*-Cre+ mice) (Figure S5A). In agreement with *Slc7a5* expression profile (Figure S1B) and the AA profile that changes only postnatally, *Slc7a5*$^{fl/fl}$;*Emx1*-Cre+ mutants are born with normal brain size (Figure S5B-C), indicating that *Slc7a5* is dispensable in the NPCs of the forebrain. Thus, *SLC7A5* mutations do not lead to microcephaly by hindering the generation of an appropriate number of neurons. However, by P40, the brain of *Slc7a5*$^{fl/fl}$;*Emx1*-Cre+ mice is significantly smaller than that of their control littermates (Figure 15A-A' and S5D). Histological analysis revealed a reduction in the thickness of the cerebral cortex of P40 *Slc7a5*$^{fl/fl}$;*Emx1*-Cre+ animals (Figure 15B-B'), with layers II-III being the drivers of this difference (Figure S5E-G'). By monitoring the brain weight over time, we found that the difference in brain size between control and *Slc7a5* mutant animals appears during the first postnatal week (Figure 15C) and remains stable from P10 onwards, coinciding with the increased *Slc7a5* expression levels in neural cells perinatally (Figure 13A-B). This time course supports a temporal dependence of *Slc7a5* function in postnatal neurodevelopment. To test if the phenotype reflects an increase in postnatal neural cell death, we assessed the protein level of Cleaved (Cl)-Caspase-3, a pro-apoptotic marker, on cortical samples obtained from control and mutant mice across development. Compared to controls, mutants show a significant increase in Cl-Caspase-3, specifically at P2 and P5 (Figure 15D). In line with the reduction of layer II-III thickness (Figure S5E-G'), most apoptotic cells are localized in the upper cortical layers (Figure S5H-I). Importantly, the period affected by the surge in Cl-Caspase-3 levels corresponds to the phase of programmed cell death targeting cortical excitatory neurons. This is an innate process required to refine the number of neurons in the cerebral cortex[28]. Specifically, to obtain a calibrated network, cortical neurons are generated in excess and subsequently eliminated by two waves of apoptosis, one of which occurs early after birth. Additionally, previous studies have shown that to obtain an optimal pyramidal/inhibitory neuron ratio, the wave of apoptosis affecting cortical excitatory neurons around P5 is followed by an adjustment in the number of inhibitory neurons[29]. Thus, although *Slc7a5*$^{fl/fl}$;*Emx1*-Cre+ mice only lack *Slc7a5* expression in the excitatory neurons of the forebrain, inhibitory cell number might be indirectly affected. Indeed, compared to their littermate controls, adult *Slc7a5*$^{fl/fl}$;*Emx1*-Cre+ animals have a significantly lower number of inhibitory neurons, particularly in the upper cortical layers (Figure S5J-K). In contrast, non-neuronal cells are unaffected (Figure S5L-O), indicating that *Slc7a5* is important specifically for neuronal functions.

Next, we asked whether the critical temporal window identified in mice is also sensitive to the loss of *SLC7A5* function in humans. Thus, having identified patients with mutations in *SLC7A5,* we measured their head size for several weeks from birth on (Figure 15E-H). Patients 130-1 and 130-2 are siblings from a non-consanguineous family presenting with the clinical feature of *SLC7A5* deficiency (Figure S5P). Trio-WES analysis of both siblings and their parents identified compound heterozygous pathogenic variants in the *SLC7A5* gene: the previously described and functionally assessed missense variant c.1124C>T, p.(Pro375Leu)[310] and a novel intragenic deletion of exons 5 to 10. Parents are heterozygous carriers. Patient 130-1 showed microcephaly at birth (-3 SD). The microcephaly progressively worsened to -5 SD at the age of 7 months (Figure 15F). The clinical history and presentation of the younger sibling, patient 130-2, are essentially similar. A mild microcephaly was diagnosed at birth (-2,5 SD), progressively deteriorating to -4.5 SD at the age of 6-7 months (Figure 15H). The phenotypic comparison of published patients[310] revealed that the constant features associated with biallelic pathogenic *SLC7A5* variants include microcephaly, developmental and motor delay, seizures and autistic features (Table S2). Notably, the pathological variants identified in patients are mostly missense mutations that impact the transport capacity, not the expression, of the transporter[310]. Thus, the human data indicates that the transport of SLC7A5 substrate is key to the patient's clinical presentation. Therefore, *SLC7A5* mutations likely result in decreased BCAA uptake and lead to microcephaly during the period of cortical refinement and programmed cell death in mice and humans.

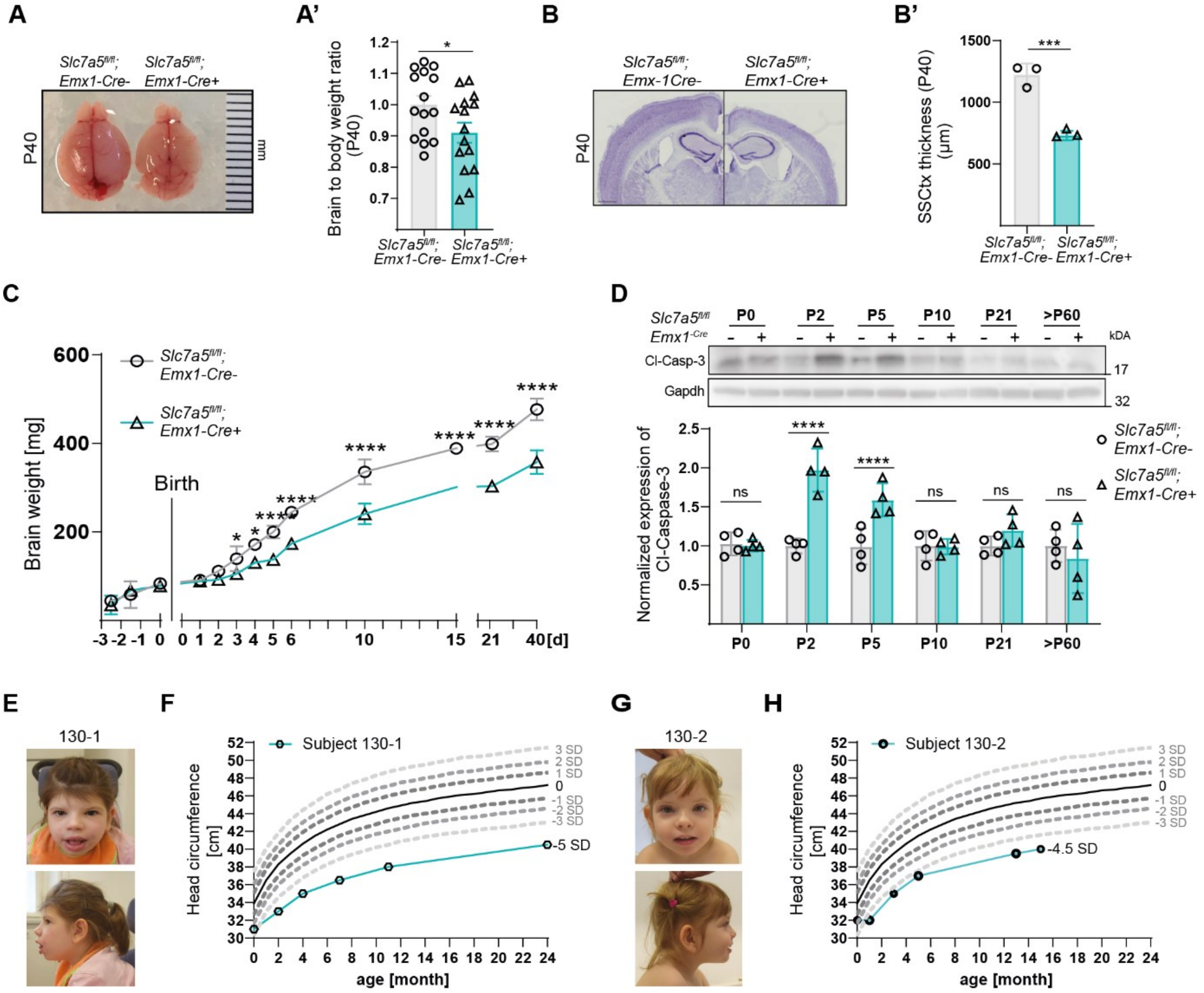

Figure 15. *Slc7a5* mutations cause postnatal microcephaly. (**A**) Pictures of adult *Slc7a5*$^{fl/fl}$*;Emx1-Cre+* and control brains. (**A'**) Brain-to-body weight ratio of adult *Slc7a5*$^{fl/fl}$*;Emx1-Cre+* mice and littermate controls (means ± SEM; n = 15 mice per genotype; **p<0.05*; unpaired two-tailed *t*-test). (**B-B'**) Representative images (**B**) and quantification (**B'**) of Nissl-stained coronal sections of P40 mutant and control SSCtx (means ± SD; n = 3 littermates per genotype; ****p<0.001*; unpaired two-tailed *t*-test; scale bar: 1500µm). (**C**) *Slc7a5*$^{fl/fl}$*;Emx1-Cre+* mice develop postnatal microcephaly during the first 10 days after birth (means ± SD; n ≥ 3 littermates per genotype/time point; **p<0.05; ***p<0.001*; *****p<0.0001;* multiple unpaired two-tailed *t*-test). (**D**) Gapdh-normalized Cleaved-Caspase-3 expression in mutant and wild-type cortex across development (means ± SD; n = 4 mice per genotype time point; ^{ns}*p>0.05; ****p<0.00001*; multiple unpaired two-tailed *t*-test). (**E** and **G**) Frontal and lateral images of patient 130-1 and 130-2, diagnosed with *SLC7A5* compound heterozygous pathogenic variants. (**F** and **H**) Measurements of the head circumference of the two patients showing the progression of microcephaly. See also Figure S5 and Table S2.

2.4 *Pyramidal neuron loss is cell-autonomously linked to Slc7a5 deficiency*

Next, we investigated whether *Slc7a5* deficiency-linked neuronal cell death is due to a cell-autonomous or non-cell-autonomous effect. Assessing this was important, especially since in the absence of Slc7a5 AAs accumulate in the extracellular space, which could be harmful to the tissue. To perform a quantitative assessment, we used the mosaic analysis with double markers (MADM) system, which enables concurrent fluorescent labeling and gene knockout in sparse single-cell clones *in vivo*[389,390]. Specifically, two reciprocally chimeric marker genes (*GT* and *TG* alleles) are targeted to identical loci upstream of *Slc7a5*. The marker genes are part of the so-called MADM cassette (M8), which consists of split coding sequences for eGFP and tdTomato fluorescent proteins interspaced by a *loxP* site (Figure S6). Following Cre recombinase-mediated interchromosomal recombination, the sequence for eGFP and tdTomato are reconstituted. Due to an innately low stochastic interchromosomal recombination rate, the green (eGFP+), red (tdTomato+), and yellow (eGFP+/tdTomato+) labeling are confined to individual sparse clones. In our experimental set-up, the Cre recombinase expression is coupled with the *Emx-1* promotor. This facilitates MADM labeling and deletion of *Slc7a5* in single telencephalic radial glia progenitors (RGs) and their progeny (Figure 16A), thereby generating cortex-specific genetic mosaics. To analyze potential cell-autonomous effects of the loss of *Slc7a5* in the developing neocortex, we assessed the relative abundance of green (eGFP, *Slc7a5*$^{-/-}$) and red (dtTomato, *Slc7a5*$^{+/+}$) excitatory neurons at different time points of postnatal development (P0, P5 and P40) in mosaic-MADM (*MADM-8*$^{GT/TG,Slc7a5}$*;Emx1-Cre*+) and control-MADM (*MADM-8*$^{GT/TG}$*;Emx1-Cre*+) animals (Figure 16B-D'). While at P0 we did not observe significant changes in the ratio of green to red cells (Figure 16B-B'), supporting that *Slc7a5* deficiency does not affect the proliferative phase of cortical development, by P5 there are significantly fewer *Slc7a5*$^{-/-}$ than *Slc7a5*$^{+/+}$ excitatory neurons (Figure 16C-C'). Further, mosaic-MADM animals present fewer *Slc7a5*$^{-/-}$ (green) neurons in upper cortical layers (LII-LIV) compared to control (red) cells, while neurons in the lower layers (LV-VI) are not affected by *Slc7a5* deletion. The same analysis done at P40 revealed a slightly more profound reduction of mutant neuronal cells in mosaic-MADM cortices (Figure 5D-D').

We concluded that the deletion of *Slc7a5* leads to a cell-autonomous increase in neuronal cell loss immediately after birth.

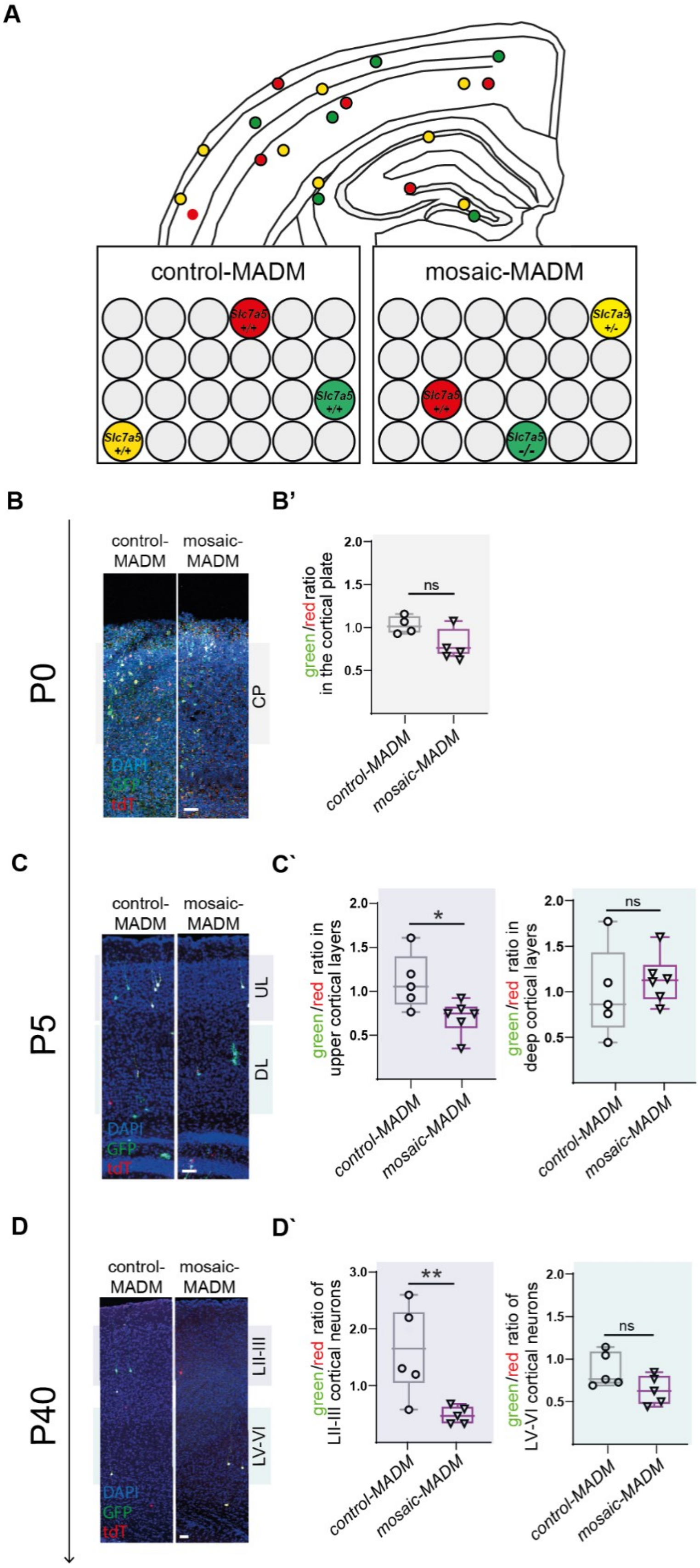

Figure 16. Loss of *Slc7a5* leads to a cell-autonomous reduction of cortical upper-layer neurons. (**A**) Schematic representation and genotypes of cells of control-MADM (*MADM-8$^{GT/TG}$;Emx1-Cre+)* and mosaic-MADM (*MADM-8$^{GT/TG,Slc7a5}$;Emx1-Cre+)* cortex. (**B**) Coronal sections and (**B'**) quantification of green/red cell ratio of MADM-labeled neurons in the cortical plate of P0 mosaic- and control-MADM littermates. (**C**) Coronal sections and (**C'**) quantification of green/red cell ratio of MADM-labeled upper layer (**left**) and lower layer (**right**) excitatory neurons in P5 mosaic- and control-MADM littermates. (**D**) Coronal sections and (**D'**) quantification of green/red cell ratio of MADM-labeled upper layer (**left**) and lower layer (**right**) excitatory neurons in P40 mosaic- and control-MADM littermates (P0: n= 4; P2 and P40: n= 5 (P2 and P40) animals per genotype; average of >5 slices per animal; $^{ns}p>0.05;^{**}p<0.001$; Mann-Whitney test; scale bar: 100µm). See also Figure S6.

2.5 LNAA-dependent metabolic reprogramming controls neuronal excitability in neonatal mice

What mechanisms could underlie the stage- and cell-type-specific cellular phenotype observed in *Slc7a5*$^{fl/fl}$;*Emx1*-Cre+ mice? Considering that neuronal excitability can determine the survival of cortical pyramidal cells during the postnatal wave of programmed cell death[28,29], we hypothesized that abnormal AA and lipid metabolism might ultimately lead to changes in excitability. Indeed, alterations in neuronal lipid composition, especially in GPLs, can directly affect membrane formation and structure[193]. Furthermore, protein-lipid interactions and post-translational modifications can modulate the clustering and activity of many ion channels[191,391–393]. In particular, palmitoylation, a FA-dependent posttranslational modification mediated by palmitoyltransferases, is an important regulatory mechanism in neurons[261,394,395]. Indeed, we found that three palmitoyltransferases are deregulated in *Slc7a5* mutants (Figure S7A). These include Zdhhc17, which specifically modifies proteins involved in neuronal functions. Additionally, approximately half of the downregulated proteins associated with the GO-term "integral component of the plasma membrane" (Figure 14E) are regulated by palmitoylation. Among these, we found Ank2, which is palmitoylated to support membrane scaffolding of the voltage-gated sodium channel Nav1.2[396]; Kcnd2, a potassium channel involved in the regulation of action potential backpropagation[262,397]; and Snap25, one of the top targets of Zdhhc17 involved in various neuronal functions[398,399] (Figure S7A). Thus, we assessed the intrinsic excitability of layer II-III pyramidal neurons from the somatosensory cortex of mutant and control animals at P6-P7 by performing whole-cell current clamp recordings while applying a series of current steps to elicit APs. Recordings from *Slc7a5$^{fl/fl}$;Emx1-Cre*+, *Slc7a5$^{fl/+}$;Emx1-Cre*+ and wild-type littermates revealed a substantial reduction in neuronal firing in *Slc7a5*$^{fl/fl}$*;Emx1-Cre+* animals (Figure 17A and S7B-C). Since both metabolic abnormalities and reduced neuronal survival in *Slc7a5*$^{fl/fl}$*;Emx1-Cre+* mice are limited to the first days after birth, we performed current-clamp recordings at P25-26 to assess whether the neuronal excitability defect is restricted to the same time window. Indeed, at P25-26 *Slc7a5*$^{fl/fl}$*;Emx1-Cre+* samples are indistinguishable from controls (Figure 17B and Figure S7D), underscoring the importance of Slc7a5 in modulating neuronal excitability early after birth. While the transient nature of the phenotype suggests a rather direct link between the metabolic state of the neuron and its excitability, it remained a possibility that the observed electrophysiological abnormalities were due to plasticity effects associated with network properties. However, should the reduced excitability directly be connected to, or even cause Slc7a5-dependent neuronal cell loss, we expected this phenotype to be cell-autonomous. Thus, we returned to the mosaic-MADM mouse model (Figure 17C) and performed current clamp recordings from *Slc7a5*$^{-/-}$ (green) and *Slc7a5*$^{+/+}$ (red) excitatory neurons in the same animal. Indeed, the AP firing rate is significantly reduced in LII-III *Slc7a5*$^{-/-}$ neurons from the somatosensory cortex at P6-7 (Figure 17D), indicating that *Slc7a5* expression controls neuronal excitability cell-autonomously at early stages after birth. To understand the bases of the reduced firing rate caused by *Slc7a5* deletion, we analyzed the AP properties. We inferred that *Slc7a5* mutant neurons at P6-7 do not fire less because they are more immature than wild-type neurons since they show AP features more comparable to those observed in older (i.e., P25-26) control neurons (Figure 17E). Indeed, compared to controls, mutant neurons at P6-7 display larger amplitude (Figure 17F), faster rise time (Figure 17G) and more hyperpolarized AP threshold (Figure 17H), matching the AP features observed in control neurons at P25-26 and suggesting a different modulation of the voltage-gated channels involved in the initiation and rising phase of APs. In agreement, dendrites of mutant LII-III pyramidal neurons present with a more mature spine morphology compared to controls (Figure S7E-I), therefore excluding a maturation delay. Nonetheless, other properties such as the resting membrane potential, the inter-spike interval (ISI) ratio, the AP decay time and half-width are unchanged at P6-7 (Figure S7J-M). We further examined the AP waveform using the phase plane plot analysis (Figure 17I) to evaluate the dynamic changes of the membrane potential over time (dV/dt; Figure 17J). Our analysis revealed a striking increase in the velocity of the AP, highlighting a potential defect at the axon initial segment (AIS) and a faster AP backpropagation in the somatodendritic compartment of mutant neurons (Figure 17I-J), linking to the reduction of Kcnd2 protein level (Figure S7A). Accelerated AP backpropagation can also point toward defects in dendritic arborization[400]. Indeed, while the soma size is not affected (Figure S7N-O), we found a slight decrease in dendritic number and length in *Slc7a5*$^{fl/fl}$*;Emx1-Cre+* mice perinatally (Figure S7P-Q). However, these morphological alterations persist until adulthood (Figure S7R-S) and, therefore, are not associated with changes in excitability. Furthermore, while the unchanged resting membrane potential would exclude a role of ATP-dependent potassium channels, the electrophysiology data point to changes in the properties of multiple channels, probably through a different modulation and/or distribution of voltage-gated sodium (e.g., Nav1.2) and potassium channels (e.g., A-type), potentially explained by the downregulation of the detected palmitoylated proteins (Figure S7A).

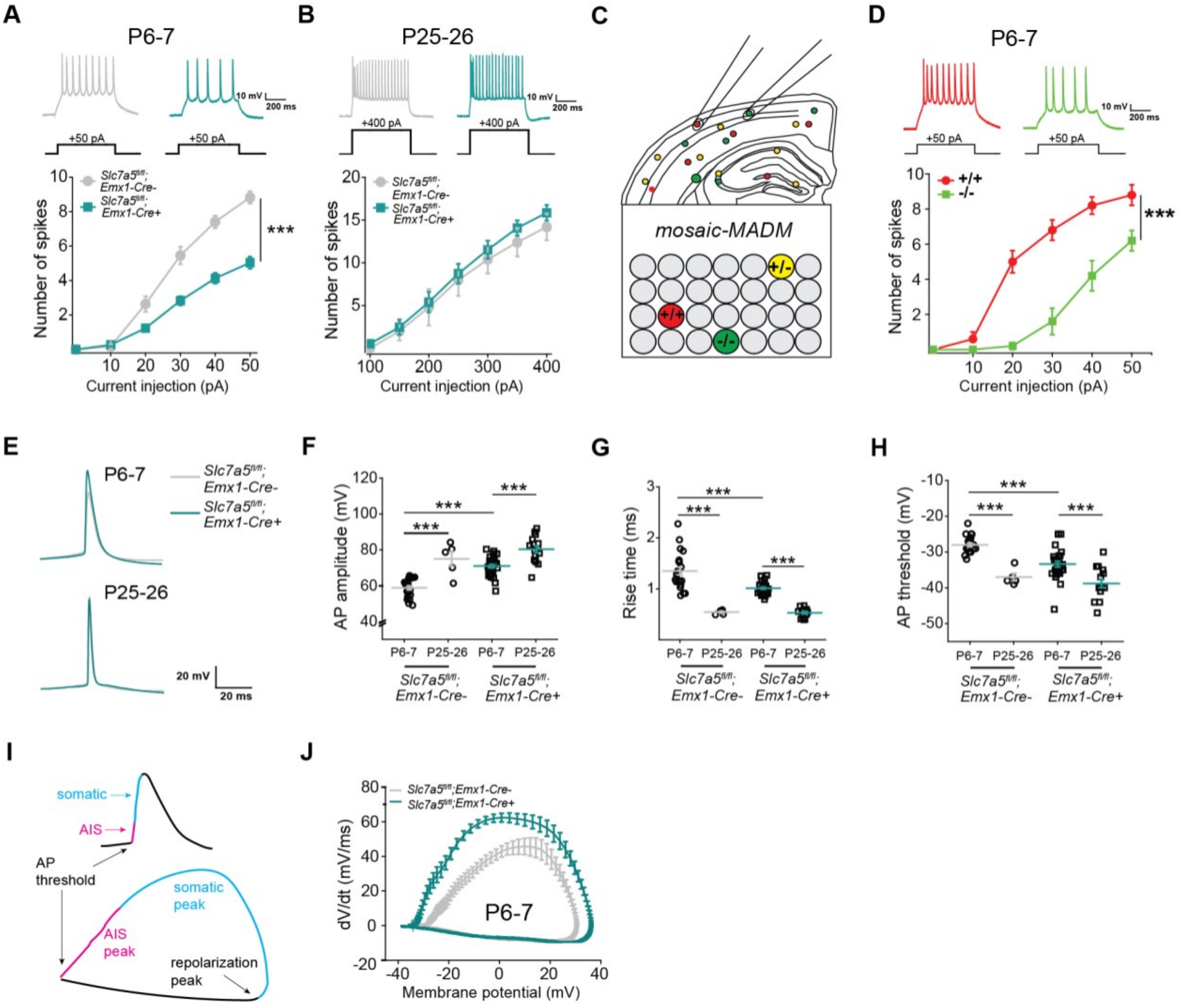

Figure 17. Intracellular AA levels modulate neuronal excitability perinatally. (**A**) Current clamp recordings from LII/III pyramidal neurons in P6-P7 *Slc7a5*$^{fl/fl}$*;Emx1-Cre+* and *Slc7a5*$^{fl/fl}$*;Emx1-Cre-* SSCtx (*Slc7a5*$^{fl/fl}$*;Emx1Cre-*

: n = 22 cells / 3 mice; *Slc7a5*$^{fl/fl}$*;Emx1-Cre*+: n = 30 cells / 3 mice; Two-way ANOVA: genotype F(1,311) = 123.01 ***p<0.001, current step F(5,311) = 205.3 ***p<0.001, interaction F(5,311) = 16.75 ***p<0.001) and (**B**) P25-P26 (*Slc7a5*$^{fl/fl}$*;Emx1Cre*-: n = 5 cells / 3 mice; *Slc7a5*$^{fl/fl}$*;Emx1-Cre*+: n = 15 cells / 3 mice; Two-way ANOVA: genotype F(1,139) = 1.84 ^{ns}p>0.5, current step F(6,139) = 34.87 ^{ns}p>0.5, interaction F(6,139) = 0.07 ^{ns}p>0.5). (**C**-**D**) Schematic (**C**) and results (**D**) of patch clamp recordings from green (*Slc7a5*$^{-/-}$) and red (*Slc7a5*$^{+/+}$) LII/III pyramidal neurons from the same P6-P7 mosaic-MADM animal (*Slc7a5*$^{+/+}$*:* n = 5 cells; *Slc7a5*$^{-/-}$: n = 7 cells from 5 mice; Two-way ANOVA: genotype F(1,65) = 116.05 ***p<0.001, current step F(5,65) = 79.22 ***p<0.001, interaction F(5,65) = 11.16 ***p<0.001). (**E**) Representative action potential (AP) traces from the data shown in (**A**-**B**). The AP amplitude (**F**), AP rise time (**G**) and AP threshold (**H**) are transiently affected in Slc7a5 deficient LII/III pyramidal neurons at P6-7 (numbers as in (**A**)) compared to age-matched littermates and P25-26 time point (numbers as in (**B**); Two-way ANOVA for AP amplitude: genotype F(1,71) = 23.15 ***p<0.001, time point F(1,71) = 52.57 ***p<0.001, interaction F(1,71) = 3.24 ^{ns}p>0.5, Holm-Sidak post hoc ***p<0.001. Two-way ANOVA for AP rise time: genotype F(1,71) = 7.32 ***p<0.001, time point F(1,71) = 101.21 ***p<0.001, interaction F(1,71) = 6.4 *p<0.05, Holm-Sidak post hoc ***p<0.001. Two-way ANOVA for AP threshold: genotype F(1,71) = 10.56 **p<0.01, time point F(1,71) = 42.93 ***p<0.001, interaction F(1,71) = 2.61 ^{ns}p>0.5, Holm-Sidak post hoc ***p<0.001. (**I**) AP plotted as voltage vs. time (**top**) and dV/dt vs. voltage (phase-plane plot, **bottom**). Phases of the AP are color-coded to highlight the initiation of the AP in the axon initial segment (AIS; pink), the propagation in the somatodendritic compartment (blue), and the repolarization peak. (**J**) Phase-plane plot of data shown in (**A**) reveals defects in the AIS and the somatodendritic compartment in LII/III pyramidal neurons of *Slc7a5*$^{fl/fl}$*;Emx1-Cre*+ animals. See also Figure S7.

2.6 Slc7a5 deficient animals show persistent behavioral defects

To assess whether the alterations observed in *Slc7a5* mutant animals during the period of cortical circuit refinement lead to permanent behavioral abnormalities, we subjected adult *Slc7a5*$^{fl/fl}$*;Emx1-Cre*+ and control animals to behavioral tests. In an open field, mutant animals present with increased horizontal (Figure 18A-B’) and vertical explorative behavior (Figure 18C) but no anxiety-like behaviors (Figure 18D). Since *SLC7A5* patients present with severe motor deficits, we assessed locomotion features in *Slc7a5*$^{fl/fl}$*;Emx1-Cre*+ mice. Indeed, mutant mice exhibit moderate motor deficits (Figure 18E), such as decreased stride and stance length (Figure 18F-F’’), as well as hind limb clasping behavior (Figure 18G-G’). Next, we tested *Slc7a5*$^{fl/fl}$*;Emx1-Cre*+ mice for social interest and social memory behaviors. We found that *Slc7a5*$^{fl/fl}$*;Emx1-Cre*+ mice have indications of sociability and social-memory impairments (Figure 18H-K’). In summary, our analyses show that *Slc7a5* deficiency in neurons causes persistent behavioral dysfunctions.

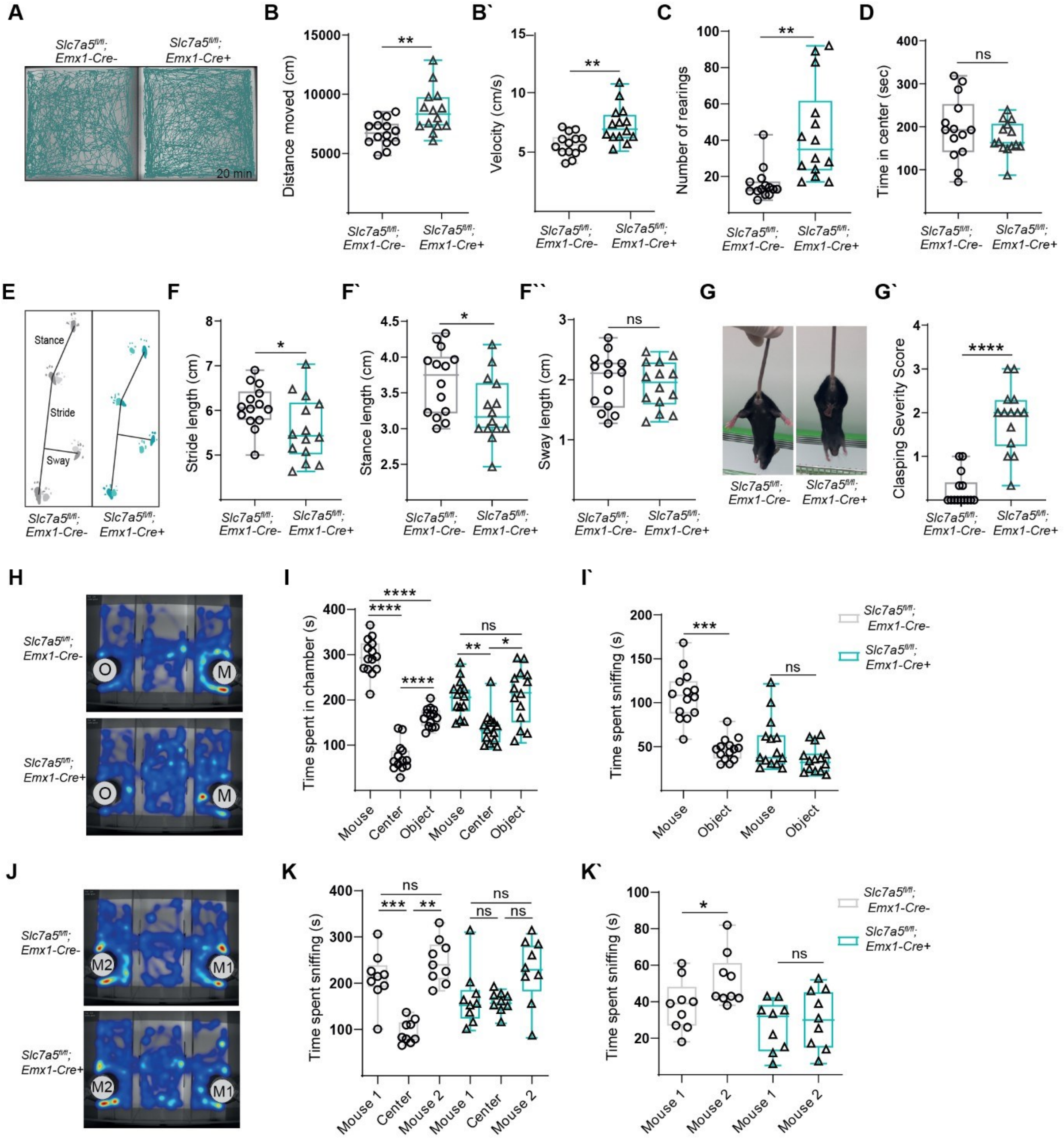

Figure 18. Loss of *Slc7a5* in cortical excitatory neurons causes persistent behavioral dysfunctions. (**A-C**) *Slc7a5*$^{fl/fl}$*;Emx1-Cre+* animals are hyperactive. (**A**) Representative traces of mutant and wild-type animals moving 20 min in an open field. (**B**) Quantification of the total distance traveled, (**B'**) velocity**,** (**C**) number of rearings and (**D**) time spent in center during one open field session (n=14 mice per genotype; two-tailed unpaired *t*-test). (**E-F''**) *Slc7a5*$^{fl/fl}$*;Emx1-Cre+* animals display a mild gait defect. (**E**) Representative control and mutant strides. Quantification of stride (**F**), stance (**F'**) and sway (**F**'') length (n=14 per genotype, $^{*}p<0.05$; two-tailed unpaired *t*-test). (**G**) Hind limb clasping observed in *Slc7a5*$^{fl/fl}$*;Emx1-Cre+* mice. (**G'**) Scoring of hind limb clasping severity (0–1 (normal) to 3 (most severe) (n = 14 animals per genotype; $^{****}p<0.00001$; two-tailed unpaired *t*-test)**.** (**H-K'**) *Slc7a5*$^{fl/fl}$*;Emx1-Cre+* mice present defects in sociability. (**H**) Representative heat maps of control (**top**) and mutant (**bottom**) behavior during the first round of the three-chamber sociability test (TCST). (**I**) Quantification of time spent in the chamber and (**I'**) time spent sniffing (*n* = 14 mice per genotype; $^{****}p<0.00001$, $^{**}p<0.01$; $^{*}p<0.05$; $^{ns}p>0.05$; 1-way ANOVA and Sidak's multiple comparison test). (**J**) Representative heat maps of control (**top**) and mutant (**bottom**) behavior during the second round of the TCST. (**K**) Quantification of time spent in the chamber

and (**K'**) time spent sniffing (*n* = 9 mice per genotype; females only; $^{***}p<0.0001$, $^{**}p<0.01$; $^{*}p<0.05$; $^{ns}p>0.05$; 1-way ANOVA and Sidak's multiple comparison test).

3 Methods

**Unless otherwise specified, experiments were performed by Lisa S. Knaus.*

3.1 Experimental model and subject details

Animals

All animal protocols were approved by the Institutional Animal Care and Use Committee at IST Austria and by the Bundesministerium für Bildung, Wissenschaft und Forschung, Austria (approval number: BMBWF-66.018/0015-V/3b/2019). All Experiments were performed on mice ranging from embryonic day (E) 12.5 to postnatal day (P) 90. Embryonic time points were determined by plug checks after timed matings, defining E0.5 as the morning after copulation. Animals were kept on a 12 h light/dark cycle (lights on at 7:00 am) and housed in groups of 3-4 animals per cage, with food and water available ad libitum. Experiments were carried out under specific pathogen-free conditions and the health status of the mouse lines was routinely checked by a veterinarian. All transgenic mouse lines were back-crossed into C57BL/6J background ≥2 times. Experiments were carried out using littermate pairs of the same sex. Both, males and females were used for experiments. The *Slc7a5*^{fl}*;Emx1-Cre* conditional line was generated by crossing *Slc7a5*$^{fl/fl}$ mice with animals expressing the Cre recombinase under the *Emx1* promoter (B6.129S2 (Emx1tm1cre)Krj/J). In the *Slc7a5*^{fl} (B6.129P2-Slc7a5tm1.1Daca/J) mouse line, exon 1, including the initiation codon, is flanked by two loxP sites. *Slc7a5*^{fl}*;Tie2-Cre* conditional animals were generated by crossing *Slc7a5*$^{fl/fl}$ with *Tie2-Cre* mice. The generation of the *Tie2-Cre*, *Emx1-Cre* and *Slc7a5*^{fl} lines has been previously described[363,401,402]. In addition, for this study we generated mosaic *Slc7a5*-MADM (*MADM-8*$^{GT/TG,Slc7a5}$*;Emx1*$^{-Cre/+}$) mice with sparse green (GFP^{+}) homozygous *Slc7a5*$^{-/-}$ mutant, yellow (GFP^{+}/tdTomato^{+}) heterozygous *Slc7a5*$^{+/-}$, and red (*tdTomato*$^{+}$) *Slc7a5*$^{+/+}$ wild-type cells in an otherwise unlabeled heterozygous background. To this end, *Slc7a5*^{fl} were genetically linked to the MADM-8 TG cassette via meiotic recombination as described previously[389]. The primer sequences for MADM-GT and

MADM-TG cassettes for MADM-8 can be found in Contreras et al.[389]. The sequence of all the other genotyping primers is given in Table S1.

Human subjects

For the human subjects (patients and their parents), written informed consent and collection of data and samples were obtained according to a protocol approved by the Ethics Committee of the Medical University of Vienna (protocol number 1443/2020). Family 130 with two affected daughters (patients 130-1 and 130-2) was referred to genetic counseling and testing in the Institute of Medical Genetics of Medical University Vienna through a supporting Centre for Developmental Disabilities in Vienna. Trio-WES analysis of both siblings and their parents identified compound heterozygous pathogenic variants in the *SLC7A5* gene: the previously described and functionally assessed missense variant c.1124C>T, p.(Pro375Leu)[310] and a novel intragenic deletion of exons 5 to 10. Parents are heterozygous carriers. Patient 130-1 was born at term and showed microcephaly at birth (head circumference (HC) of 31 cm, -3 SD). Birth weight and height were normal. The microcephaly deteriorated progressively to -5 SD (HC of 36.6 cm) at the age of 7 months. A premature closure of fontanelles was observed from the age of 8 months. A surgical treatment (frontobasal advancement) of presumed craniosynostosis was performed at the age of 12 months. The patient displayed pronounced muscular hypotonia and motor delay. At the age of 3 years, the patient developed seizures, which could be successfully treated with valproate. Brain MRI showed, in addition to microcephaly, pontocerebellar and corpus callosum hypoplasia. At the time of the first genetic counseling, patient 130-1 was 9 years and 4 months old and presented with severe microcephaly and growth retardation (HC 43 cm, -7 SD; height 109 cm, -4.5 SD and weight 17.1 kg, -4 SD). The patient could sit independently and stand with help but could not walk and the speech was absent. The history and presentation of the younger sibling, patient 130-2, are essentially similar. The microcephaly was diagnosed at birth, progressively deteriorating to -4.5 SD by the age of 6-7 months, followed by premature closure of fontanelles. Pontocerebellar and corpus callosum hypoplasia were detectable by brain imaging. At genetic counseling, patient 130-2 was 4 years and 4 months old and displayed severe microcephaly (-6 SD), growth retardation (-5 up to -6 SD), global developmental delay (independent sitting possible, no walking, absent speech) and autistic features. The first seizures occurred at the age of 6 years and are controlled with anticonvulsive treatment. Before WES analysis an aCGH (Microarry-based Comparative Genomic Hybridization) was carried out, providing inconspicuous results for both patients.

3.2 Method details

Whole-exome sequencing analysis of patient samples

**performed by Maria Gerykova Bujalkova and Mateja Smogavec*

Whole-exome sequencing: Whole-exome sequencing was performed for both affected siblings and their healthy unrelated parents (extended Trio-WES). DNA samples were prepared following the workflow of the TruSeq Exome Library Kit (Illumina) for the enrichment of exonic regions. The final library was paired-end sequenced on an Illumina NextSeq500 sequencer. Sequencing reads were aligned to GRCh37/hg19 using the Burrows Wheeler Aligner (BWA-MEM) and further processed in house according to GATKs best practice protocol for calling single nucleotide variants, insertions and deletions. The evaluation of the called variants was performed using the program VarSeq from Golden Helix Inc®. Variants were classified according to the American College of Medical Genetics and Genomics (ACMG) guidelines[403]. In addition, a copy number variation (CNV) analysis was performed with the VarSeq software by comparing the calculated coverage of each sequenced sample of Family 130 to the coverage data of previously analyzed in-house samples. Quantitative PCR (qPCR): To verify the identified multiexonic deletion of *SLC7A5* we performed a quantitative PCR (qPCR) using CFX Connect™ Real-Time PCR Detection System (Bio-Rad) with primers spanning the deleted region. All primers were purchased from Eurofins Genomics. The specificity of each primer set was monitored by a dissociation curve. PCR reactions were performed in triplicate and normalized to *PAPD5 and PRKD1*. Primer sequences are listed in Table S1.

Immunofluorescence

Immunofluorescent staining of adult mouse brain: Adult littermate animals were anesthetized and transcardially perfused with 4% paraformaldehyde (PFA). After dissection, brains were post-fixed in 4% PFA overnight and dehydrated using 30% sucrose (in 1X phosphate buffered saline (PBS)). Dehydrated brains were sectioned at 30-40 µm on a Sliding Microtome SM2010R (Leica). Adult brain sections were stained free-floating. No antigen retrieval was performed unless specifically recommended in the primary antibody datasheet. Sections were washed in 1X PBS and blocked with 4% normal donkey or goat serum in 0.3% Triton X-100. Primary antibodies were diluted in blocking solution and incubated overnight on a horizontal shaker at 4°C. After 14-16h, the sections were washed and a species-specific secondary antibody was added for 2 h at room temperature (RT). For nuclear counterstaining, 300 nM DAPI (Life Technologies) in 1X PBS was applied. Sections were mounted on SuperFrost Plus™ Adhesion slides (Epredia™) using DAKO fluorescent mounting medium (Dako). Immunofluorescent staining of embryos and early postnatal brain*:* In brief, embryos were decapitated and the head was immersion-fixed for 24h in 4% PFA at 4°C. Pups (P0-P10) were decapitated and the brain was dissected. After dissection, the brain was immersion-fixed as described above. After fixation the samples were dehydrated in 30% sucrose (in 1X PBS) and embedded in Tissue-Tek® O.C.T. Compound (Sakura® Finetek). Brains were sliced on a CryoStar NX70 cryostat (Thermo Scientific™) and directly mounted on SuperFrost Plus™ Adhesion slides (Epredia™). Immunofluorescence stainings were performed directly on the slides using a humidity chamber. The detailed staining procedure is stated in the section above. A detailed list of used primary and secondary antibodies is provided in Table S1. Quantification: To examine cortical layering, the thickness of Cux1+ cell layer and the Ctip2+ cell layer was measured at three defined points of each cortical hemisphere (n= 3 littermate animals per genotype, at least 4 images per mouse). The density of upper or lower layer neurons was quantified by normalizing the number of Ctip2+ or Cux1+ cells to the total number of DAPI+ cells within a defined square. To assess the number of apoptotic cells, Cl-Caspase-3+ cells were quantified in coronal brain sections. The number of apoptotic cells located in the cortex was normalized to the total number of Cl-Caspase-3+ cells quantified in subcortical regions (n= 3 littermate animals per genotype, at least 5 images per mouse). To assess the number of inhibitory neurons, the number of Parvalbumin+ cells was quantified per cortical layer and normalized to the absolute number of Parvalbumin+ cells per cortical column (n= 3 littermate animals per genotype, at least 5 images per mouse). Potential changes in astrocyte and microglia numbers were monitored by quantifying the number of Gfap+ or Iba1+ cells per cortical column. The numbers were normalized to the size of the selected area (n= 3 littermate animals per genotype, at least 5 images per animal).

Image acquisition: Images were acquired using a Zeiss LSM800 inverted confocal microscope and analyzed in ImageJ[404].

Immunohistochemistry stainings

Nissl staining: Adult animals were transcardially perfused with 4% PFA. The brains were dissected and post-fixed overnight in 4% PFA at 4°C. P0-1 brains were immersion fixed in 4% PFA for 24h at 4°C. The fixation was followed by a dehydration step in 30% sucrose (in 1X PBS). P0-1 coronal sections were obtained at the CryoStar NX70 cryostat (Thermo Scientific™). Adult coronal sections at 40 µm thickness were obtained using a Sliding Microtome SM2010R (Leica). Sections were mounted on SuperFrost Plus™ Adhesion slides (Epredia™) and air-dried for >2h at room temperature. Sections were cleared for 10 min using RotiHistol (Carl Roth) and dehydrated using graded absolute ethanol (abs. EtOH) steps: 30%, 50%, 70%, 90%, 96%, 90% and abs. EtOH (3-5 min each). The section were stained using a 1% Cresyl Violet (Sigma Aldrich) in abs. EtOH. After staining, slices were de-stained using 2% acetic acid in abs. EtOH. After several washes in EtOH, sections were immersed in RotiHistol (Carl Roth) and mounted using DPX mountant (Sigma Aldrich). Image acquisition: Images were obtained at an Olympus slide scanner VS120 and quantified using ImageJ (n=3 per genotype, at least 4 images per mouse).

Golgi-Cox staining: Golgi-Cox staining was performed using the FD Rapid GolgiStain Kit™ (FDNeurotechnologies) kit. After three weeks of impregnation in the staining solutions provided by the kit, brains were sliced coronally (120 µm) using a Vibratome VT 1200S (Leica). The sections were mounted onto 1% gelatinized slides. After drying the samples were dehydrated through graded EtOH steps and cleared using RotiHistol (Carl Roth). Coverglasses were mounted with DPX mountant (Sigma Aldrich). Image acquisition: A Nikon Eclipse Ti2 microscope (40x objective) was used to acquire images of LII/III pyramidal neurons of the somatosensory cortex (12 neurons per brain, n=3 per genotype). For analysis, single pyramidal neurons were manually traced using Imaris software x64 v9.3.1, followed by quantification of average filament area, filament length and Sholl intersections.

RNAscope Assay

Spatial gene expression analysis was performed using the RNAscope®[405] Multiplex Fluorescent v2 Assay (ACD) kit including specific probes targeting *Slc7a5* mRNA

(ACD; Cat.# 472571 and Cat.# 461031). Sample preparation: P2 mice were decapitated and the brain was dissected rapidly on ice. The cerebellum was removed and the brain was embedded in pre-cooled Tissue-Tek® O.C.T. Compound (Sakura® Finetek) and stored at -80°C until further used. Tissue was sliced at 10 µm at a CryoStar NX70 cryostat (Thermo Scientific™) and directly mounted on SuperFrost Plus™ Adhesion slides (Epredia™). Sections were stored at -80°C. RNAscope® assay: The assay was performed according to the instructions provided by the RNAscope® Multiplex Fluorescent v2 Assay kit. In brief, sections were fixed in 4°C cold 4% PFA and further pre-treated employing a H_2O_2- and protease-digestion. After the pre-treatment, sections were incubated with the probe targeting the mRNA of interest. Probes were further hybridized to a cascade of signal amplification molecules, followed by a hybridization with a dye-labelled probe (Akyoa Sciences). After the hybridization steps, sections were stained with a nuclear counterstain and mounted using ProLong™ Gold Antifade Mountant (Invitrogen™). Image acquisition: Images were acquired at a LSM800 confocal microscope using 10X, 20X and 65X objectives.

Isolation and quantification of MADM-labelled tissue

Tissue harvesting: P0 and P5 animals were decapitated, brain was isolated and fixed in 4% PFA overnight at 4°C. From P6 onwards, mice were transcardially perfused using 4% PFA. Brains were post-fixed in 4% PFA overnight to ensure complete fixation. Brains were cryopreserved with 30% sucrose in 1X PBS for approximately 48 h and were then embedded in Tissue-Tek® O.C.T. Compound (Sakura® Finetek). 40 µm coronal frozen sections were cut on a Sliding Microtome SM2010R (Leica), and mounted on SuperFrost Plus™ Adhesion slides (Epredia™). Next, sections were stained with 300 nM DAPI (Life Technologies). The coverglass was mounted using DAKO fluorescent mounting medium (Dako). Image acquisition: Images were acquired using a Zeiss LSM800 inverted confocal, Olympus Slidescanner VS120 or Nikon Eclipse Ti2. Images were post-processed and analyzed in Zen Blue 2.6 software and ImageJ. Quantification: The number of MADM-labelled green, red and yellow neurons within the somatosensory cortex was quantified according to their localization within the different cortical layers. The ratio between green and red neurons was calculated per animal (>10 hemispheres per animal; n=6 mice per genotype).

Electron microscopy

**sample preparation performed by ISTA Electron microscopy facility*

Sample preparation: P2 mice were decapitated and the brain was dissected, washed in 0.1M PB, dropped into EM suitable fixative (2.5% glutaraldehyde and 2% PFA in 0.1M PB) and fixed for 10 min using a BioWave Pro+ microwave (Pelco). Fixed brains were sliced at a Leica Vibratome VT 1200S (100 µm). Sections were placed in 1% osmium tetroxide in 0.1M PB solution, followed by 1% uranyl acetate in 50% EtOH. This step was followed by a dehydration protocol with ascending EtOH concentration (50%, 70%, 90%, 96% and 2x 100%). Samples were then placed into propylene oxide, followed by consecutive incubations in 1:2, 1:1 and 2:1 Durcupan:propylene oxide solutions and an overnight incubation in Durucupan. After the treatment, samples were mounted on siliconized coverslips, placed on a heating plate for 30 min at 37°C, followed by 48 h at 60°C to allow the polymerization of the resin. The region of interest (layer II/III somatosensory cortex) was cut and re-embedded in a resin block for further slicing. Ultrathin serial section (70 nm) ultrathin serial sections were cut using an UC7 ultramicrotom (Leica Microsytems), collected on formvar-coated copper-slot grids and examined in FE-SEM. Image acquisition: Images were acquired on a Tecnai T10 transmission electron microscope at 24000X magnification.

Western Blot

Sample preparation: Mice at different developmental time points were decapitated, the cortex was dissected on ice, snap frozen and stored at -80°C until further used. For protein extraction cortices were homogenized in ice-cold lysis buffer (20mM Tris-HCl pH:8, 137mM NaCl. 10% Glycerol, 0.1% NP-40, 1mM EDTA, 9.5mM NaF, 10mM PPi (Sodium pyrophosphate dibasic), 1mM Na_3Vo_4) plus cOmplete™ Protease Inhibitor (Roche). Samples were kept on ice for 20 min followed by a centrifugation step at 500g for 10 min at 4°C. The supernatant was transferred into a fresh tube and centrifuged at max speed for 20 min at 4°C. The lysates were again transferred into a fresh tube, aliquoted and stored at -80°C. Protein concentration was determined using the Pierce™ BCA Protein Assay Kit (Thermo Fisher). Western Blot assay: Samples were diluted with 2X Laemmli buffer (10% SDS, 20% Glycerol, 100mM Tris-Cl (pH 6.8), Bromophenol blue, 3% Pierce™DTT), denatured at 65°C for 10 min and separated using 8-12% SDS-PAGE gels. 25-50 µg of protein per sample were loaded. Proteins were blotted to an Immobilon®-P PVDF Membrane (Merck) for 1-2 h at 4°C with 300 mA constant current using a Bio-Rad immunoblot apparatus. The membranes were blocked using 2.5% Bovine serum albumin (BSA) in 1X Tris-buffered Saline + 0.1% Tween (TBST) for 1h at room temperature. Primary antibodies were diluted in blocking solution and the membranes incubated overnight at 4°C on a horizontal shaker. After several washes with 1X TBST, the secondary anti-IgG antibodies coupled to horseradish peroxidase (HRP) were diluted in blocking solution and the membranes incubated for 1h at RT. Signal detection: Detection was carried out using Pierce™ ECL Western Blotting Substrate (ThermoFisher) or SuperSignal™ West Pico PLUS Chemiluminescent Substrate (ThermoFisher) in combination with the Amersham Imager 680 (GE Healthcare).

Untargeted metabolomic of whole cortical tissue

**sample analysis performed by VBCF metabolomics core facility*

Sample preparation: Mice were decapitated and the brains dissected on ice. Cortices were collected in 2ml Eppendorf tubes, washed with 1ml ice-cold 1X PBS, weighed and stored at -80°C until further processed. Metabolite extraction: Ice-cold solvent mixture (methanol:acetonitrile:H2O (2:2:1, v/v) MS-grade; cooled to -20°C) was added to the tissue and homogenized for 1 min using Bel-Art® disposable pestles. The homogenization was followed by a sonication step of 5 min in a water bath sonicator. The samples were incubated for 1 h at -20 °C, followed by a centrifugation step at 14,000g for 3 min at 4°C. The supernatant was transferred into a 1.5-ml microcentrifuge tube and stored at -20°C and the pellet was re-suspended in ice-cold solvent (methanol:acetonitrile:H2O (2:2:1, v/v)). After vortexing, the pellet was incubated for another hour at -20°C and then centrifuged at 14,000g for 3 min at 4°C. The resulting supernatant was combined with the supernatant obtained in the previous centrifugation step and incubated for 2 h at -20°C. This was followed by a last centrifugation step at 14,000g for 10 min at 4°C. The supernatant was again transferred to a new 1.5-ml microcentrifuge tube, snap frozen and stored at -80°C. Sample analysis: Extracts were thawed on ice and centrifugated for 5 min at 15,000g. 10 µL of each sample were pooled and used as a quality control (QC) sample. Samples were randomly assigned into the autosampler and injected on the respective phase system. For HILIC (hydrophilic interaction chromatography), an iHILIC®-(P) Classic, PEEK column, (100mm x 2.1mm, 5µm) with a precolumn (HILICON) was used. A 26 min gradient from 90% A (acetonitrile) to 80% B (25 mM ammonium bicarbonate in water) was used, employing a flow rate of 100 µL/min delivered through an Ultimate 3000 HPLC system (Thermo Fisher). After the analysis by HILIC-MS/MS, samples were analyzed with reversed phase chromatography (RP). Here, an ACQUITY UPLC HSS T3 column (150mm x 2.1mm; 1.8 µm) with VanGuard precolumn (Waters Corporation) was used. A 20 min gradient of 99% A (0.1% formic acid in water) to 60% B (acetonitrile with 0.1% formic acid) was employed using the same HPLC system and flow rate. In both cases, metabolites were ionized via electrospray ionization in polarity switching mode after HILIC separation and in positive polarity mode after RP separation. Sample spectra were acquired by data-dependent high-resolution tandem mass spectrometry on a Q-Exactive Focus (Thermo Fisher Scientific™). The ionization potential was set to +3.5/-3.0 kV, the sheet gas flow was set to 20, and an auxiliary gas flow of 5 was used. Samples were analyzed in a randomized fashion and QC samples were additionally measured in confirmation mode to obtain additional MS/MS spectra for identification. Obtained data sets were processed by Compound Discoverer software v3.0 (Thermo Fisher Scientific™). Compound annotation was performed with a mass accuracy of 3 ppm for precursor masses and 10 ppm for fragment ion masses searched in public spectral databases as well as our in-house spectral library. Experimentally obtained retention times were used for the validation of metabolite identifications.

Targeted intracellular metabolomics

**sample analysis performed by VBCF metabolomics core facility*

Sample preparation: P2 mice were decapitated, the cortices dissected on ice and the meninges and hippocampus removed. The tissue was dissociated according to the protocol provided by the Papain Dissociation System (Worthington Biochemical Corp.) kit to obtain a single cell suspension. In brief, cortices were moved to 50 ml TPP® TubeSpin Bioreactor tubes (Merck) and incubated in papain for 30 min at 37°C in a shaking water bath. After several dissociation steps, cells were pelletized at 200g for 8 min at room temperature and re-suspended in EBSS + 1%BSA. The cell suspension was stored on ice while the live cell count was determined using a TC20 Automated Cell Counter (Bio-Rad). Metabolite extraction: 1x10^6 cells per sample were transferred into a 1.5 ml Eppendorf tube and centrifuged at 200g for 8 min at 4°C using a tabletop centrifuge. The supernatant was removed and 100µl ice-cold solvent mixture (methanol:acetonitrile:H2O (2:2:1, v/v) MS-grade; cooled to − 20°C) was added to the pellet. The cells were mechanically homogenized with a P1000 pipette for 1 min and then sonicated for 5 min in a water bath sonicator. Samples were further processed as described for the untargeted metabolomics analysis and stored at -80°C until analyzed. Sample analysis: Polar metabolites were analyzed using HILIC-LC-MS/MS. Each sample was injected onto an iHILIC®-(P) Classic, PEEK column, (100mm x 2.1mm, 5µm) with a precolumn (HILICON). An Ultimate 3000 HPLC system (Dionex, Thermo Fisher Scientific™) was used, employing a flow rate of 100 µl/min and directly coupled to a TSQ Quantiva mass spectrometer (Thermo Fisher). A 15-minute gradient from 14% B to 80% B (A: 95% acetonitrile 5% 10 mM aqueous ammonium acetate; B: 5 mM aqueous ammonium bicarbonate) was used for separation. The following transitions were used for quantitation in the negative ion mode (2.8 kV): pyruvate: 87 m/z → 43 m/z, lactate: 89 m/z → 43 m/z, taurine: 124 m/z → 80 m/z, ketoleucine: 129 m/z → 85 m/z, α-ketoglutaric acid: 145 m/z → 101 m/z, AMP: 346 m/z → 79 m/z, IMP: 347 m/z → 79 m/z, ADP: 426 m/z → 134 m/z, ATP: 506 m/z → 159 m/z, NAD: 662 m/z → 540 m/z, NADH: 664 m/z → 408 m/z, NADP: 742 m/z → 620 m/z, NADPH: 744 m/z → 426 m/z, CoA: 766 m/z → 408 m/z, Acetyl-CoA: 808 m/z → 408 m/z and in the positive ion mode (3.5kV) GSH: 308 m/z → 408 m/z, GSSG: 613 m/z → 355 m/z and SAM: 399 m/z → 250 m/z. The remaining metabolites were quantified by reverse phase LC-MS/MS, injecting 1 µl of the metabolite extract onto a RSLC ultimate 3000 (Thermo Fisher) directly coupled to a TSQ Altis mass spectrometer (Thermo Fisher) via electrospray ionization. A Kinetex C18 column was used (100 Å, 150 x 2.1 mm), employing a flow rate of 80 µl/min. A 7-minute-long linear gradient was used from 99% A (1 % acetonitrile, 0.1 % formic acid in water) to 60% B (0.1 % formic acid in acetonitrile). Liquid chromatography-tandem mass spectrometry (LC-MS/MS) was performed by employing the selected reaction monitoring (SRM) mode of the instrument in the positive ion mode, using the transitions 156 m/z → 110 m/z (histidine), 175 m/z → 70 m/z (arginine), 241 m/z → 74 m/z (cystine), 76 m/z → 30 m/z (glycine), 133 m/z → 70 m/z (ornithine), 175 m/z → 74 m/z (asparagine), 106 m/z

→ 60 m/z (serine) 120 m/z → 74 m/z (threonine), 147 m/z → 84 m/z (lysine), 147 m/z → 130 m/z (glutamine), 148 m/z → 84 m/z (glutamic acid) 90 m/z → 4 m/z (alanine and sarcosine), 104 m/z → 84 m/z (GABA), 176 m/z → 159 m/z (citrulline), 116 m/z → 70 m/z (proline), 118 m/z → 72 m/z (valine), 150 m/z → 133 m/z (methionine), 132 m/z → 86 m/z (isoleucine and leucine), 182 m/z → 136 m/z (tyrosine), 166 m/z → 103 m/z (phenylalanine), 205 m/z → 188 m/z (tryptophane), 134 m/z → 74 m/z (aspartic acid) 177 m/z →160 m/z (serotonin) and 154 m/z → 137 m/z (dopamine). For all transitions, the optimal collision energy was defined by analyzing pure metabolite standards. LC-MSMS chromatograms were interpreted using TraceFinder (Thermo Fisher). After LC-MS/MS analysis, retention times were verified by standard addition of pure compounds to arbitrarily selected samples, validating experimental retention times with the respective pure substances. Statistical analysis: Raw peak areas were normalized using the probabilistic quotient normalization method as described in Dieterle et al.[406] implemented using pandas 1.3.5[407] and numpy 1.22.4[408]. P-values were computed using an unpaired two-tailed t-test and corrected using the Benjamini-Hochberg procedure implemented in statsmodels 0.13.1[409].

Parallel untargeted lipidomics and metabolomics

**sample analysis performed by EMBL metabolomics facility*

Sample preparation: P2 mice were decapitated, cortices dissected on ice and the meninges and hippocampus removed. The left hemisphere was immediately transferred into a 1.5ml Eppendorf-tube and snap frozen for whole tissue lipidomics/metabolomics. The right hemisphere was dissociated with the Papain Dissociation System (Worthington Biochemical Corp.) kit and used to obtain the cellular lipidome/metabolome. Dissociation protocol is described in the previous section. Lipid and metabolite extraction: For lipid and metabolite extraction, samples were treated as described in the section above. Ice-cold isopropanol:H2O (90% - 10%, v/v) was used as a solvent. EquiSPLASH™ LIPIDOMIX® Quantitative Mass Spec Internal Standards (Avanti Polar Lipids) and Metabolomics Amino Acid Mix Standards (Cambridge Isotope Laboratories) were added as internal standards to the solvent.

Sample analysis: LC-MS/MS analysis was performed on a Vanquish UHPLC system coupled to an Orbitrap Exploris 240 high-resolution mass spectrometer (Thermo Fisher Scientific™) in positive and negative ESI (electrospray ionization) mode. All experimental samples were measured in a randomized manner. Pooled quality control (QC) samples were prepared by mixing equal aliquots from each processed sample. Multiple QCs were injected at the beginning of the analysis in order to equilibrate the LC-MS system. A QC sample was analysed after every 5th experimental sample to monitor instrument performance throughout the analytical sequence. For determination of background signals and subsequent background subtraction, an additional processed blank sample was recorded. Data was processed using MS-DIAL[410] and raw peak intensity data was normalized via internal standards or total ion count of all detected analytes[411]. Feature identification was based on accurate mass, isotope pattern, MS/MS fragment scoring and retention time matching to an in-house library (metabolomics) and the MS-DIAL LipidBlast library (lipidomics). Analysis of untargeted metabolomics data: Chromatographic separation was carried out on an Atlantis Premier BEH Z-HILIC column (Waters; 2.1 mm x 100 mm, 1.7 µm) at a flow rate of 0.25 mL/min. The mobile phase consisted of water:acetonitrile (9:1, v/v; mobile phase phase A) and acetonitrile:water (9:1, v/v; mobile phase B), which were modified with a total buffer concentration of 10 mM ammonium acetate (negative mode) and 10 mM ammonium formate (positive mode), respectively. The aqueous portion of each mobile phase was pH-adjusted (negative mode: pH 9.0 via addition of ammonium hydroxide; positive mode: pH 3.0 via addition of formic acid). The following gradient (20 min total run time including re-equilibration) was applied (min/%B): 0/95, 2/95, 15/50, 14/60, 14.5/50, 16.5/50, 16.8/95, 20/95. Column temperature was maintained at 40°C, the autosampler was set to 4°C and sample injection volume was 5 µL. Analytes were recorded via a full scan with a mass resolving power of 120,000 over a mass range from 60 – 900 m/z (scan time: 100 ms, RF lens: 70%). To obtain MS/MS fragment spectra, data-dependant acquisition was carried out (resolving power: 15,000; scan time: 22 ms; stepped collision energies [%]: 30/50/150; cycle time: 600 ms). Ion source parameters were set to the following values: spray voltage: 4100 V / 3500 V, sheath gas: 30 psi, auxiliary gas: 5 psi, sweep gas: 0 psi, ion transfer tube temperature: 350°C, vaporizer temperature: 300°C. Analysis of untargeted lipidomics data: Chromatographic separation was carried out on an ACQUITY Premier CSH C18 column (Waters; 2.1 mm x 100 mm, 1.7 µm) at a flow rate of 0.3 mL/min. The mobile phase consisted of water:acetonitrile (40:60, v/v; mobile phase phase A) and isopropanol:acetonitrile (9:1, v/v; mobile phase B), which were modified with a total buffer concentration of 10 mM ammonium acetate + 0.1 % acetic acid (negative mode) and 10 mM ammonium formate + 0.1% formic acid (positive mode), respectively. The following gradient (23 min total run time including re-equilibration) was applied (min/%B): 0/15, 2.5/30, 3.2/48, 15/82, 17.5/99, 19.5/99, 20/15, 23/15. Column temperature was maintained at 65°C, the autosampler was set to 4°C and sample injection volume was 5 µL (dissociated cells) and 1 µL (tissue samples). Analytes were recorded via a full scan with a mass resolving power of 120,000 over a mass range from 200 – 1500 m/z (scan time: 100 ms, RF lens: 70%). To obtain MS/MS fragment spectra, data-dependant acquisition was carried out (resolving power: 15,000; scan time: 54 ms; stepped collision energies [%]: 25/35/50; cycle time: 600 ms). Ion source parameters were set to the following values: spray voltage: 3250 V / 3000 V, sheath gas: 45 psi, auxiliary gas: 15 psi, sweep gas: 0 psi, ion transfer tube temperature: 300°C, vaporizer temperature: 275°C.

Proteomic analysis

**sample analysis performed by ISTA Proteomics core facility*

Sample preparation for the proteomics analysis of whole cortical tissue: P5 mice were decapitated, the cortices dissected on ice, the hippocampus was removed and the samples stored at -80°C until used for further steps. Sample preparation for the proteomics analysis of Slc7a5 co-immunoprecipitation from neural cell membranes: Lysates enriched for cell membranes were obtained based on the protocol modified from Lee et al.[412]. Brief, P5 Slc7a5$^{fl/fl}$;Tie2-Cre+ animals were used to ensure that the precipitated Slc7a5 is derived from neural cells-only. Animals were decapitated and the brain was dissected on ice. Hippocampus and meninges were removed. The cortex was homogenized in ice-cold solution A (pH7.4; 5mM HEPES; 0.32M sucrose;1mM NaHCO; 1mM MgCl; 0.5 mM CaCl; ddH$_2$O) using a teflon-homogenizer on ice. 150µl of the fresh lysate was transferred into a separate tube and 1% NP-40 was added (=L1 - whole lysate). The remaining sample was centrifuged in a table-top centrifuge at 1400 g for 10 min at 4°C. The supernatant was transferred to a fresh 1.5ml tube. Solution A was added to the pellet and homogenized with a pipette. The homogenate was centrifuged at 700 g for 10 min at 4°C. The two supernatants were combined, transferred into 13.2ml Thinwall Ultra-Clear™ Tubes (Beckman Coulter) and centrifuged at 13.800x g (RCF) for 10 min using an OPTIMA-XPN 100 ultracentrifuge. 150µl of the supernatant + 1%NP-40 were transferred into a fresh tube (=S2- cytosolic fraction). To obtain the membrane fraction of the sample (=M1), the pellet was re-suspended in solution B (pH8.0; 6mM Tris-HCl, 0.32M sucrose; 1mM NaHCO; ddH$_2$O), mechanically homogenized with a pipette and 1% NP-40 was added. The protein concentration of L1, S2 and M1 fractions was determined using the Pierce™ BCA Protein Assay Kit (Thermo Fisher Scientific). The samples were snap-frozen and stored at -80°C. Only fraction M1 was further used for the co-immunoprecipitation experiment. Co-immunoprecipitation was performed using Protein A Magnetic beads (Abcam) and a DynaMag™-2 Magnet (Invitrogen™) rack. The beads were washed and equilibrated using IP-lysis buffer (50 mM Tris-HCl (pH 8.0); 120 mM NaCl; 0.5% NP-40; 1 mM EDTA). 800µg of total protein per sample were used as input. Crude lysates were pre-cleared to eliminate proteins, which unspecifically bind to the beads. In detail, the samples were incubated with pre-washed beads for 2 hrs on a rotating rack at 4°C. After incubation a magnetic field was applied using the DynaMag™-2 Magnet rack to collect the pre-cleared lysate. During the 2hrs pre-clearing step, pre-washed beads were incubated in lysis buffer with either normal rabbit igG control (Cell Signaling Technologies) or the anti-LAT1 (Slc7a5) antibody (25µg of antibody per sample) rotating at 4°C. After 2 hrs the conjugated beads were washed twice and re-suspended in IP-lysis buffer w/o NP-40 (50 mM Tris-HCl (pH 8.0); 120 mM NaCl; 1 mM EDTA). After this step die actual pull-down was performed by incubating the pre-cleared lysate over night with i) beads conjugated to the primary anti-LAT1 (Slc7a5) antibody (IP+) and ii) beads conjugated to the IgG control (IP-) at 4°C on a rotating rack. On the next day IP+ flow through was collected using the magnetic rack. The beads were washed using IP-lysis buffer and gently vortexed. The samples were moved on the magnetic rack again and the supernatant was removed. The beads were washed and re-suspended in IP-lysis buffer w/o NP-40. The IP+ and IP- samples were further used for mass spectrometry analysis. <u>Mass spectrometry analysis:</u> All samples were processed with the iST-NHS kit from PreOmics GmbH. Modified protocols for on-beads digest (lysis for 10 min at 60°C) or whole tissue (sonication for 10*30s in a Bioruptor sonicator in presence of 50 mg Protein Extraction beads (Diagenode)) were used for co-IP samples and tissue samples, respectively. Digestion time was 2h for samples from co-IP experiments, 3.5 h for tissue samples. Two TMT-10plex kits were used (lot VK306785 for the whole lysate dataset, lot WC306775 for the co-IP dataset). Samples were cleaned up and combined. The whole lysate TMT sample was fractionated by offline High pH Reversed Phase fractionation into 48 fractions (A: de-ionized water + 10 mM NH4OH; B: 90% LC-grade Acetonitrile + 10 mM NH4OH; flow: 0.15 mL/min; 0-4 min: 1% B, 115 min: 25%, 140 min: 40%, 148 min: 75%, maintained for 12 min, followed by 45 min equilibration at 1% B). Unfractionated co-IP samples and whole lysate fractions were vacuum-dried overnight then re-dissolved in LC-LOAD (co-IP samples) and sent for MS analysis. <u>LC-MS/MS analysis:</u> All samples were analyzed by LC-MS/MS on an Ultimate 3000 nano-HPLC (Dionex) coupled with a Q-Exactive HF (Thermo Fisher Scientific™). Chromatographic method: peptide samples were loaded onto a GEN1 uPAC column (Pharmafluidics; Thermo Fisher Scientific™); solvent A: H2O, 0.1% formic acid; solvent B: 80% acetonitrile in H2O, 0.08% formic acid; gradients: tissue fractions, 2% to 44% B in 60 min; co-IP dataset, 2% to 31% (155 min) then 44% B (180 min); Mass Spectrometry method: Data-Dependent acquisition (Full MS / dd-MS2); MS1: 1 microscan, 120,000 resolving power, 3e6 AGC target, 50 ms maximum IT, 380 to 1,500 m/z, profile mode; up to 20 data-dependent MS2 scans per duty cycle, excluding charges 1 or 8 and higher, dynamic exclusion window 10s (60 min gradient) or 60s (180 min gradients); isolation window 0.7 m/z, fixed first mass 100 m/z, resolving power 60,000, AGC target 1e5, maximum IT 100 ms, (N)CE 32. <u>Data analysis:</u> Each dataset was independently searched in MaxQuant[413] (1.6.17.0 for whole tissues, 2.0.1.0 for co-IPs) against a *Mus musculus* fasta database downloaded from UniProtKB. Fixed modification was set to $C_6H_{11}NO$. Variable modifications were set to include Acetyl (protein N-term), Oxidation (M), Gln->pyroGlu and Deamidation (NQ) and, for whole tissue, Phospho (STY). Match-between-runs and second peptides were set to active. All FDRs were set to 5% (whole tissue) and 1% (co-IPs). Each MaxQuant output evidence.txt file was then re-processed separately in R using in-house scripts. Evidence reporter intensities were corrected using the relevant TMT lot's purity table, scaled to parent peptide MS1 intensity and then normalized using the Levenberg-Marquardt procedure. The long format evidence table was consolidated into a wide format peptidoforms table, adding up individual values where necessary. Peptidoform intensity values were log10 transformed. Values were re-normalized (Levenberg-Marquardt procedure). Protein groups were inferred from observed peptidoforms, and, for each group, the estimated expression values across samples were calculated by averaging individual peptidoform log10 intensity vectors, scaling the vector to reflect the intensity level of the most intense peptidoform according to the best flyer hypothesis (phospho-peptides and their unmodified counterpart peptide were excluded). Peptidoform and protein group log2 ratios were calculated: to the corresponding control sample (IP- performed on the same individual) for co-IPs, or to the average reference (WT) sample (whole lysate dataset). Statistical significance was tested with the limma package[414]Seurat v4.2, performing both a moderated t-test and an F-test. The Benjamini-Hochberg procedure was applied to compute significance thresholds at various pre-agreed FDR levels. Regardless of the test, protein groups with a significant p-value were deemed to be regulated if their absolute log2 fold change (= logFC) was greater than 95% of control to average control logFC. During the analysis phase, two out of five mutant samples from the cortical lysates dataset behaved as outliers and were excluded from further analysis. Protein groups were annotated with GO terms, applying a term if it, or one of its offspring terms, was found among the annotations of any protein accession which could explain all peptides in the group. GO enrichment analysis was performed using an in-house script built around the topGO package v2.50.0, comparing separately for each contrast all up- or down-regulated proteins, or both, against the background of all identified protein groups.

Bulk RNA-sequencing of cortical tissue

Sample preparation: P1-P2 pups were decapitated and the brains were dissected on ice under RNAse free conditions. Total RNA of one cortical hemisphere was extracted using TRIzol™ Reagent (Invitrogen™) and chloroform (Sigma Aldrich), followed by centrifugation at 12000 g for 15 min at 4°C. The upper phase was transferred to a fresh tube and 1.5 volumes of 100% EtOH were added. Total RNA was purified by using the RNA Clean&Concentrator-5 prep Kit (Zymo Research). The samples were further treated with RQ1 RNase-Free DNase (Promega) as described in the kit instructions manual. RNA concentration and quality was assessed by using the NanoDrop spectrophotometer (Thermo Fisher Scientific) and the Bioanalyzer 2100 with the RNA 6000 Nano kit (Agilent). cDNA libraries were generated with the SENSE mRNA-Seq Library Prep Kit V2 (Lexogen) using 1.5 µg total RNA. The quality of the generated libraries was monitored by using the High Sensitivity DNA Analysis Kit (Agilent) and the Bioanalyzer 2100. Libraries were sequenced on an Illumina HiSeq 2500 instrument. Analysis: De-multiplexed raw reads were trimmed before alignment using the FASTX toolkit v0.0.14. Trimmed reads were aligned to the mouse genome using STAR[415] v2.5.4 (genome: GrCm38, gene annotation: Gencode release M8). Read counts per gene were quantified using STAR. The aligned sequencing data were uploaded to *the public server at usegalaxy.org*[416]. Differential expression analysis was performed in usegalaxy.org using the Bioconductor package DESeq2[417] v1.34.0 using an FDR threshold of 0.05. Gene Ontology enrichment analysis was performed using the Bioconductor package GOstats[418] v2.36.0 with a p-value cutoff of 0.001 and conditional testing enabled.

Analysis of the untargeted metabolomics dataset

**performed by Daniel Malzl*

Combining hydrophilic interaction and reversed phase chromatography results and filtering: Measurement of metabolites was done by LC-MS using hydrophilic interaction liquid chromatography (HILIC) or reversed phase chromatography (RP). The two analyses returned overlapping metabolites. Assuming quantifications in RP would align with quantifications in HILIC, we combined HILIC and RP by adding to the HILIC data those metabolites that were detected by RP but not by HILIC. Subsequently, the combined data were filtered to retain only those metabolites that were mapped to a KEGG ID. Data visualization was performed using Seaborn v0.11.2[419] and Matplotlibs v3.5.2[420]. Principal component analysis: Principal component analysis was conducted in Python using scikit-learn v1.1.2[421]. Metabolite time course analysis: Time course analysis was conducted on the combined and filtered metabolomics data. In brief, the mean abundance of the metabolites in WT and KO at each time point was computed and resulting averages were normalized to values between 0 and 1 such that the maximum abundance over time is 1 and the minimum abundance over time is 0. This was done for each metabolite in each genotype separately. Differential dynamics of metabolites between the genotypes were assessed by computing the Pearson correlation coefficient r between normalized trajectories in WT and KO where metabolites with $r < 0.975$ were considered to show differing dynamics[422]. For visualization purposes metabolites were manually annotated to five main metabolic pathways. Grouping of metabolites based on trajectories: Normalized trajectories of WT and mutants were grouped using a gaussian mixture model (GMM) with six components (implemented in scikit-learn v1.1.2[421]). The optimal number of components was assessed with the Bayesian information criterion. Ternary plot generation: Raw time point values for each metabolite in the combined and filtered data were averaged over replicates and normalized to sum to 1. These values were then plotted using the python-ternary library v1.0.8. Metabolic pathway enrichment: For classical pathway enrichment analysis, list of pathway annotations of classes ‘metabolism’ and ‘information processing’ were retrieved from the Kyoto Encyclopedia of Genes and Genomes (KEGG). Enrichment analysis was conducted by assessing the significance of overlap between a given set of metabolites and a pathway with Fisher’s exact test and subsequent multiple testing adjustment using the Benjamini-Hochberg procedure using an FDR of 0.05.

Analysis of single-cell RNA sequencing data

**performed by Florian M. Pauler*

Raw data: DiBella et al.[423]: Raw data was obtained from GEO (developmental age given in brackets): GSM4635077 (E16), GSM4635080 (P1), GSM4635081 (P1), GSM4635078 (E18), GSM4635079 (E18), GSM5277845 (P4). Metadata was obtained from Broad Institute Single Cell Portal (https://singlecell.broadinstitute.org/single_cell on 03/2022). Cell types CThPN, SCPN were grouped with DL CPN. Yuan et al.[424]: Raw counts and meta data was obtained from GEO, accession number GSE204759. Analysis: All analyses were performed using R (v4.1.2) and Seurat[425] Neuron (v4.1.0). One Seurat object was created for each sample using function CreateSeuratObject with parameters: min.cells = 3, min.features = 200. Expression data was normalized using function NormalizeData with standard parameters. Where applicable (E18, P1 DiBella et al.[423]), replicates were combined prior to normalization. Expression of *Slc7a5* was identified as fraction of cells showing a normalized expression of Slc7a5 > 0, relative to the total number of cells in that cell type. Clopper-Pearson confidence intervals were calculated using function clopper.pearson.ci (package GenBinomApps v1.2) with parameters: alpha = 0.05, CI = "two.sided".

Electrophysiology

**performed by Bernadette Basilico*

Sample preparation: Acute brain slices were obtained from P6-7 and P25-P26 mice. Coronal sections (300 μm) were prepared from primary somatosensory cortex. Animals were decapitated under isoflurane anesthesia and whole brains were rapidly removed from the skull and sectioned using a VT 1200S vibratome (Leica) in ice-cold cutting solution, containing (mM): 87 NaCl, 25 $NaHCO_3$, 2.5 KCl, 1.25 NaH_2PO_4, 10 glucose, 75 sucrose, 7 $MgCl_2$, 0.5 $CaCl_2$ (320 mOsm, 7.2-7.4 pH). Slices were allowed to recover at room temperature for at least 1 h in regular artificial cerebrospinal fluid (ACSF), containing (mM): 125 NaCl, 2.5 KCl, 1.25 NaH_2PO_4, 25 $NaHCO_3$, 25 glucose, 1 $MgCl_2$ and 2 $CaCl_2$ (320 mOsm, 7.2–7.4 pH). The ACSF was continuously oxygenated with 95% O2 and 5% CO2 to maintain the physiological pH. When older mice were tested (P25-26), slices were sectioned in ice-cold cutting solution containing (mM): 93 NMDG, 2.5 KCl, 1.2 NaH_2PO_4, 30 $NaHCO_3$, 20 HEPES, 25 glucose, 5 sodium ascorbate, 2 thiourea, 3 sodium pyruvate, 10 $MgCl_2$, 0.5 $CaCl_2$ (320 mOsm, 7.2-7.4 pH). Slices from P25-26 mice were recovered at 32˚C for 10-12 minutes in the same solution and then allowed to recover at room temperature for at least 1 h in regular ACSF. Slices were visualized under infrared-differential interference contrast (IR-DIC) using a BX-51WI microscope (Olympus) with a QIClickTM charge-coupled device camera (Q Imaging Inc.). Recordings*:* Patch pipettes (4-6 MΩ; World Precision Instruments) were pulled on a P-1000 puller (Sutter Instruments) and filled with the intracellular recording solution, containing (mM): 128 K-gluconate, 10 HEPES, 10 Na_2-phosphocreatine, 1.1 EGTA, 5 MgATP, 0.4 NaGTP (osmolarity adjusted to 295 mOsm with sucrose, 7.3-7.4 pH). Current clamp recordings were performed at room temperature (24 ± 1 °C) from layer II/III pyramidal neurons. When experiments were performed in mosaic-MADM animals, patch clamp from layer II/III was visually guided by fluorescent labeling of neurons to recognize wild type (tdTomato+) and knock-out (GFP+) pyramidal neurons in the same brain slice. Analysis*:* Membrane capacitance and resting membrane potential were determined immediately after the establishment of whole-cell configuration. Neuronal membrane potential was held at approximately -60 mV (P6-7 mice) or -70 mV (P25-26 mice) by constant current injection. Current steps ranging in amplitude from -40 to +50 pA (10 pA increments; 600 ms duration) were applied to estimate the *f – I* relationship. In current clamp experiments from P25-26 mice, current steps ranging in amplitude from -300 to +400 pA (50 pA increments; 600 ms duration) were applied to estimate the *f – I* relationship. Properties of individual action potentials (APs) were determined from the first current step necessary to elicit at least one AP. Phase-plane plot analysis was performed to evaluate the dynamic changes of the membrane potential over time (dV/dt). The threshold was set as the voltage at which the first derivative of the voltage trace reached 20 V/s. Amplitude was calculated as the difference between the threshold and the peak. AP half-width was measured at half the difference between the firing threshold and the AP peak. The inter-spike interval (ISI) ratio was calculated as the ratio of the last ISI relative to the first. Current clamp recordings were filtered at 2 kHz, sampled at 20 kHz and acquired using a MultiClamp 700B amplifier and a Digidata 1550A. Recorded signals were analyzed off-line using the Clampfit 10 software (Molecular Devices).

Biocytin filling of neurons

**performed by Bernadette Basilico*

Sample preparation: Acute brain slices were obtained from P6-7 mice, as described in the previous section. To specifically label pyramidal neurons from layer II/III of the somatosensory cortex, patch pipettes (4-6 MΩ; World Precision Instruments) were pulled on a P-1000 puller (Sutter Instruments) and filled with the intracellular recording solution, containing (mM): 128 K-gluconate, 10 HEPES, 10 Na2-phosphocreatine, 1.1 EGTA, 5 MgATP, 0.4 NaGTP and 0.5% biocytin (osmolarity adjusted to 295 mOsm with sucrose, 7.3-7.4 pH). We dialyzed neurons for ~10-15 minutes by whole-cell patch clamp. After pipette removal, slices were immediately fixed in 4% PFA overnight at 4°C. For visualization of the biocytin filling, sections were blocked in 5% normal goat serum in 1X PBS for 45 min at room temperature, followed by incubation with Streptavidin Alexa Fluor™ 488 Conjugate overnight at 4°C. After the incubation step a nuclear counterstain was applied and the sections were mounted on SuperFrost Plus™ Adhesion slides (Epredia™) using Dako fluorescent mounting medium (Dako). Image acquisition: Fluorescently labeled neurons were imaged with a 40x objective at a Zeiss LSM800 inverted confocal microscope. Image analysis: Images were deconvoluted using Huygens Professional software in v15.0 (Scientific Volume Imaging). Quantification of spine density and morphology was performed in NeuronStudio[426]. Sholl analysis was performed after tracing the complete dendritic tree in Imaris software x64 v9.3.1.

Behavioral analysis

All behavioral tests were performed during the light period. Mice were habituated to the test room 24 h before each test. For all studies, sex-matched littermate pairs were employed. Equipment was cleaned between each trial with 70% EtOH. Mice were given 24 h to recover between different tests. All behavioral studies were performed starting with the least aversive task first and ending with the most aversive one.

Behavioral tests were carried out with P55 to P65 animals. Open field test: Exploratory behavior in a novel environment was assessed in an open field arena (45cm (L) x 45cm (W) x30cm (H)) made out of dark Plexiglas. The animal was placed in the center of the arena and videotaped for 20 min. Locomotor activity (distance traveled and velocity) in the center or periphery of the arena, as well as rearing, were tracked and analyzed using the EthoVision XT 11.5 software (Noldus). Three chamber sociability test*:* Mice were tested for social deficits as described previously[427]. Briefly, the behavior of the animals was monitored in a rectangular three chambers arena (60cm (L) x 40cm (W) x 20 cm (H)) made of clear Plexiglas. Age- and sex-matched littermate pairs were used for all tests. Sex- and age-matched C57BL/6J mice were used as "stranger" mice. Mice were habituated to the wire cage for 2x 10 min 24h before the test. During the first session (habituation), each subject was placed into the center chamber with open access to both left and right chambers, each chamber containing an empty wire cage. After ten minutes of habituation, mice were tested in the "social phase." An age-matched stranger was placed in the wire cage of the left chamber, while a novel object was placed into the right chamber's cage. The wire cage (12cm (H), 11cm diameter) allows nose contact between the test subject and the C57BL/6J strangers. The test animal was allowed to explore the arena for 10 min freely. Locomotor activity (distance traveled and velocity) and the number of nose contacts (< 5cm proximity) with the caged mouse/object were recorded and analyzed by EthoVision XT 11.5 software (Noldus). Vertical explorative behavior was assessed by manually quantifying the number of rearings during the habituation phase. Gait measurement test*:* Potential gait impairments were monitored using "the footprint test"[428]. In brief, the fore and hind paws were painted with dyes of contrasting colors. The mouse was placed in a narrow corridor on white paper. A darkened house was used as bait to encourage the mouse to walk in a straight line. The footprint patterns were then analyzed for stride length, sway length and stance length. Hind limb clasping test*:* To assess potential hind limb clasping behavior, mice were suspended by their tails for 10s. During this period, the hind limb position was monitored and scored according to the severity of the phenotype[429]. The test was repeated three times for each animal.

Quantification and statistical analysis

Statistical analyses were performed using Microsoft® Excel® 2013, GraphPad Prism 9.0 and Origin 2018 and Python. Shapiro–Wilk test was employed to evaluate normal distribution, means and standard deviations of the given data. Parametric data were analyzed for significance using unpaired two-tailed t-tests, 1-way or 2-way ANOVAs with Sidak's post-hoc test, using *p<0.05, **p<0.01, and ***p<0.001 for significance. Data were presented as a bar, box and whiskers, scatter dot plots and mean ± standard deviation, unless otherwise specified. Data sets with non-normal distributions were analyzed using the two-tailed Mann–Whitney U test. Enrichment analysis for metabolomics data was performed using Fisher's exact test. Where applicable, multiple testing corrections have been performed using the Benjamini-Hochberg procedure.

3.3 Illustrations and Figures

Illustrations were prepared using Adobe Illustrator and BioRender (BioRender.com). In case illustrations were adapted from previously published literature, the primary source was cited in the Figure legend titel.

3.4 Data and code availability

Raw data

Metabolomics and lipidomics data have been deposited at MetaboLights, proteomics data at iProX and RNA-sequencing data at GEO. All data are publicly available as of the date of publication. Accession numbers or unique identifiers are listed in Table S1. All original code has been deposited at Zenodo and is publicly available as of the date of publication. DOIs are listed in the Table S1.

Additional resources

All supplementary data is available in Knaus et al. 2023 (doi: https://doi.org/10.1016/j.cell.2023.02.037)

4 Discussion

Neurons are generated in large amounts early during embryonic brain development but a significant fraction of them are removed at subsequent developmental stages[71,75,430]. The removal of these cells must be highly selective and therefore regulated by tight mechanisms, possibly integrating both extrinsically- and intrinsically-driven processes. While a complete view of the factors directing this process is still missing, the literature suggests that neuronal activity might be used as a measure of neuronal integration in the circuitry, and therefore it is a determinant of the refinement of the perinatal network[29,75]. However, the potential upstream signaling and the pattern of neuronal activity determining this phenomenon remain unclear. Identifying extrinsic and intrinsic factors that can modulate neuronal properties at this developmental stage is critical since disrupting the refinement process can permanently affect brain circuits.

Here we focused on the metabolic state of neural cells of the murine cerebral cortex as a measure of the intrinsic fit of a neuron and a key-determinant of its integration in the developing cortical circuit. Importantly, although metabolism is a crucial element of cellular fitness, there is no detailed description of how metabolism reprograms and the levels of various metabolites change during different critical periods of forebrain formation. By obtaining a metabolomic profile of the murine cortex at various developmental stages, we provide a comprehensive view of the metabolites detected in this brain region and their changes over the course of development. As several metabolites are linked to neurodevelopmental conditions, our data can be utilized to evaluate potential critical time windows implicated in the onset of neurological disorders characterized by dysregulated brain-related metabolites. This is especially of interest, since recent studies suggest that timely interventions, such as dietary supplementation, administered during critical developmental periods have the capacity to redirect atypical developmental trajectories observed in patients of certain neurometabolic disorders[311,431–434].

For example, our analysis underscored a downward trajectory for essential LNAAs, with their levels decreasing significantly in the cerebral cortex at the perinatal period. By deleting *Slc7a5*, a LNAA transporter whose mutations cause autism and microcephaly, we tested the importance of regulating those AAs for the metabolic and physiological state of neural cells. We found that *Slc7a5* expression is a determinative factor in specifying cortical neurons' metabolic state at perinatal stages. At this developmental stage neurons gradually upscale their activity levels, which causes a significant augmentation of the neuronal net energy demand. Our findings suggest that while mature neurons depend on metabolic support provided by glial cells to sustain these massive bioenergetic requirements, maturing neurons, lacking this sustenance, need to transfer additional substrates into their bioenergetic pathways. Our results indicate that during the first two weeks after birth neurons use LNAAs, especially BCAAs, as one of the main substrates for ATP production. In this context, it is intriguing to observe that *Slc7a5* transcription in neurons is induced by hypoxia[435,436], a physiological state fetuses experience during and shortly after birth[437]. This would explain the surge in *Slc7a5* expression at this stage.

What are the consequences that may arise if the expected levels of substrates for Slc7a5 are insufficiently met during this period of development? Our findings indicate that a reduction in intracellular BCAAs during this perinatal period is associated with a deregulation of lipid metabolism in neurons. Notably, this timeframe of increased LNAA demand coincides with the phase of dendritogenesis[438] in forebrain development. This intricate process relies on large quantities of lipids and FAs as structural components of cellular membranes, and is vital for the intricate elaboration of complex neurite structures and, consequently, the establishment of a functional cortical network[439,440]. Previous studies have suggested a connection between BCAA and lipid metabolism in some cell types[185,441–443] and pathological conditions[444–446]. Now, we show a link between the catabolic processes of BCAAs and FAs in neurons. Specifically, the loss of Slc7a5 leads to a compensatory upregulation of BCAA catabolism, resulting in an inadvertent disruption of lipid metabolism affecting predominantly the GPL profile of these cells.

Further, *Slc7a5* deletion leads to a transient cell-autonomous change in neuronal excitability of pyramidal neurons *in vivo*, providing an elegant example of coupling the fitness of a cell with its integration in the neuronal network. Our MADM analysis further suggests that intrinsic excitability can directly affect neuronal survival probability of these neurons at this developmental stage. The exact mechanisms underlying the altered neuronal excitability remain unclear. Our transcriptomic analysis did not uncover changes in ion channel expression in *Slc7a5*-deficient neurons. However, our proteomics data indicate changes in membrane-associated palmitoylated proteins in perinatal mutant mice. Thus, the most plausible explanation is that the shift in lipid profile observed in *Slc7a5* deficient cells leads to a different clustering and modulation of ion channels involved in neuronal excitability. In addition, a shift in the ratio of specific GPL subclasses can affect membrane properties such as its fluidity and curvature[193], which can further modulate neuronal excitability[191,391,447].

Surprisingly, despite the ubiquitous expression of Slc7a5 in almost all neural cell populations of all cortical layers, the loss of this AA transporter affects primarily the survival of upper layer excitatory neurons. Possible explanations for this observed variation between cell types include (i) the metabolic flexibility of non-neuronal cell types and (ii) the comparatively low energy requirements of glial cells in contrast to neurons. Further, the layer-specific disparity in the survival rates of pyramidal neurons may arise from variations in the temporal availability of glial metabolic support across different cortical layers during corticogenesis. In the murine cortex, astrocytes begin to appear at birth and subsequently undergo periods of proliferation and maturation during the initial postnatal month[40,448,449]. Ge et al.[40] demonstrated that the first-born pioneering astrocytes, derived from RGs in the SVZ, primarily populate LV-VI. These astrocytes proliferate and gradually colonize the outer layers of the cortex. The subsequent phases of astrocytic maturation and diversification exhibit a layer-specific pattern[450] and are strongly influenced by differences in local neuronal activity[35,449]. Altogether, the sequential delay caused by the "inside-out" pattern of neuronal and glial colonization and maturation in the cortex may contribute to the heightened susceptibility of upper layer neurons to the absence of Slc7a5.

Our findings suggest that Slc7a5 plays a crucial role in determining the metabolic state of the postnatal developing brain. Notably, a proteomics analysis of a co-immunoprecipitation experiment of Slc7a5 from neural membranes provided additional evidence for the involvement of this AA transporter in the intricate metabolic dynamics of neural cells. This analysis did not only confirm the previously established interaction between Slc7a5 and Slc3a2 in neural membranes but also revealed a novel interaction between Slc7a5 and Ide, an enzyme responsible for insulin degradation[380–382]. This direct interaction suggests Slc7a5 as a key player in feedback loops associated with glucose and AA metabolism. Intriguingly, patients with insulin insensitivity, who experience impaired glucose uptake, demonstrate elevated serum levels of BCAAs[451], indicating a disruption of such feedback loops in individuals with type-2 diabetes. Moreover, recent findings demonstrate that insulin binding, specifically in the hypothalamus, induces elevated BCAA catabolism in the liver[452]. Altogether, this suggests that Slc7a5 functions as an integral component of a broader regulatory feedback loop system that modulates cellular responses to changes in glucose and AA availability through insulin signaling. Unfortunately, there is a minimal number of tools available to assess metabolic pathways with the needed temporal and spatial resolution. Consequently, our study describes tissue-wide metabolic states but does not uncover cell-type-specific or short-lasting changes. Gene knockouts represent a powerful tool for studying facets of metabolism in specific cell populations *in vivo*, as done here for *Slc7a5*. Yet, given the interconnection between different arms of metabolism, establishing causality remains challenging. In the future, it would be interesting to dissect the exact contribution of different signaling pathways and subsets of metabolites to the phenotype observed in *Slc7a5* mutant mice. Efforts to obtain metabolomic data under various conditions to implement exhaustive models of metabolism may also represent one way to address this challenge. Additionally, this study exclusively concentrates on the characterization of the metabolic profile of a specific brain region, namely the cortex. Conducting additional metabolomics analyses on subcortical brain regions would enable the identification of potential differences in the metabolic profiles across various brain regions during development. Finally, although by comparing mice and individuals with *SLC7A5* mutations, we inferred similarities between species, the described metabolic states presumably also include mouse-specific changes. Studying mechanisms regulating human-specific brain metabolism is still challenging since most of the available tools involve *in vitro* systems. This poses some problems since excessive amounts of micro- and macronutrients in cell culture media can drive metabolism to different programs than *in vivo*. Hence, to better understand human brain metabolism, combination of diverse model systems and additional developmental timepoints will be necessary.

Altogether, our findings highlight the importance of dietary-obtained factors, such as essential AAs, for neurodevelopment. The similar trajectory of the microcephaly onset observed in mice and humans with *SLC7A5* mutations suggests that although our metabolic profile describes changes in the murine brain, humans and mice may employ a similar metabolic program across time. Furthermore, the stage and cell-type specificity of the observed phenotypes point to the importance of performing longitudinal studies evaluating environmental, metabolically relevant factors that can influence specific stages of brain development and that may interact with genetic factors underlying human neurodevelopmental conditions.

5 Concluding remarks and perspectives

Metabolism is defined as “the chemical processes that occur within a living organism in order to maintain life”. It is a perpetuum mobile, constantly adapting and regulating itself through the intricate interplay of various bioenergetic and biosynthetic pathways. This equilibrium defines an organism’s physiology.

For a long period, brain function was considered to be a tightly regulated process, instructed by the genome, and controlled by transcriptional, translational and epigenetic mechanisms. Recently, this conventional dogma gets progressively challenged. Researchers have come to recognize the existence of another important conductor that governs many of these processes – the metabolism. However, despite its crucial role in determining cellular physiology and fate, our understanding of how the metabolism and nutrient demands of the cerebral cortex change during critical neurodevelopmental windows remains limited.

In this study, we tackled this question by performing metabolomic profiling of the developing murine cerebral cortex. Through monitoring the developmental trajectories of over 300 metabolites, we found that the forebrain undergoes a substantial metabolic reorganization during development. Further, our findings underscore the critical importance of adequate nutrient supply during neurodevelopment, and highlight the existence of critical time windows in which specific cell types are particularly sensitive to decreased levels of certain essential metabolites.

In the coming years, understanding the metabolic demands and trajectories unique to individual cell types will be of utmost importance. This knowledge will not only allow us to better comprehend brain physiology but also to potentially identify critical time windows and treatment options in the context of metabolic neurodevelopmental disorders. Especially, since early implementation of dietary interventions may allow to mitigate the severity of certain subsets of NDDs.

6 Supplementary Information

6.1 *Supplementary Figures*

Supplementary Figure 1

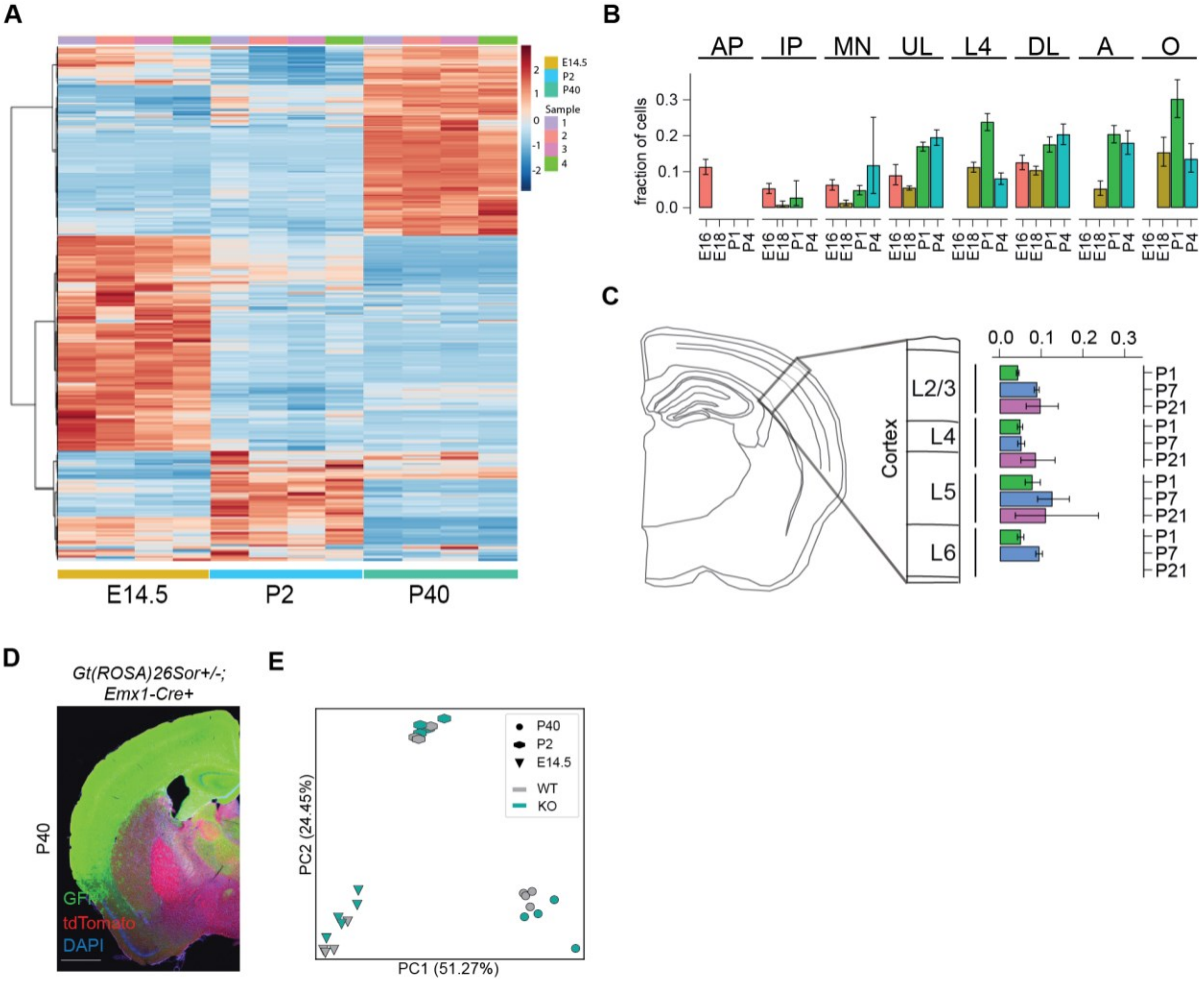

Figure S1. Untargeted metabolomic profiling of wild-type and *Slc7a5* deficient cortex, Related to Figure 12 & 13. (**A**) Heatmap visualizing changes in metabolite levels in the wild-type cortex obtained from multiple mice at three developmental time points (E14.5, P2, P40). (**B**) *Slc7a5* expression in the murine cortex during perinatal development (E16, E18, P1, P4); based on single-cell RNA sequencing data (DiBella et al.; AP: apical progenitors; IP: intermediate progenitors; MN: migrating neurons; UL: upper layer excitatory neurons; L4: layer IV excitatory neurons; DL: deeper layer excitatory neurons; A: astrocytes; O: oligodendrocytes). (**C**) *Slc7a5* expression in excitatory neurons of different cortical layers during postnatal neurodevelopment (P1, P7, P21); based on single-cell RNA sequencing data (Yuan et al.[72]; L2/3: layer II/III excitatory neurons; L4: layer IV excitatory neurons; L5: LV excitatory neurons; L6: layer VI excitatory neurons). (**D**) *Emx1*-driven Cre recombinase expression in neural cells of the neocortex was verified by utilizing the *Gt26Sor^{mtmG}* reporter mouse line. *Gt26Sor^{mtmG};Emx1-Cre+* mice express tdTomato in all cells prior to Cre recombinase exposure. After recombination, Cre recombinase expressing cells are labeled with cell membrane-localized green fluorescent protein (GFP) (scale bar: 1500µm). (**E**) PCA plot based on all detected metabolites of *Slc7a5* mutant and wild-type cortex at E14.5, P2, P40.

Supplementary Figure 2

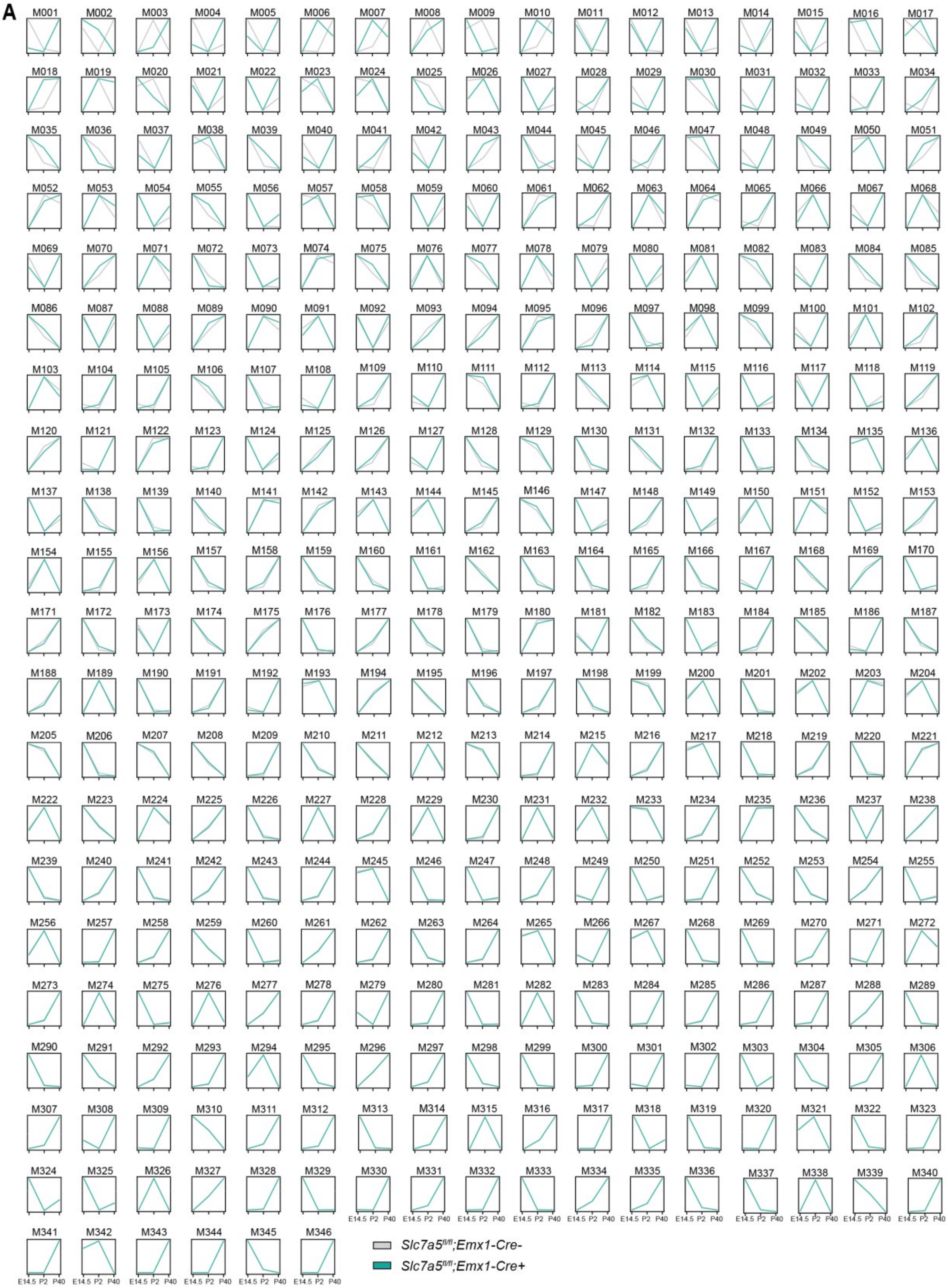

Figure S2. Developmental trajectories of metabolites detected in wild-type cortex and *Slc7a5* deficient cortex, Related to Figure 12 & 13. (**A**) Normalized and scaled trajectories of all metabolites detected in *Slc7a5*$^{fl/fl}$*;Emx1-Cre+* (cyan) and wild-type (grey) cortical tissue (x-axis: age; y-axis: scaled abundance; metabolites and Pearson's Coefficient: Supplementary data 1).

Supplementary Figure 3

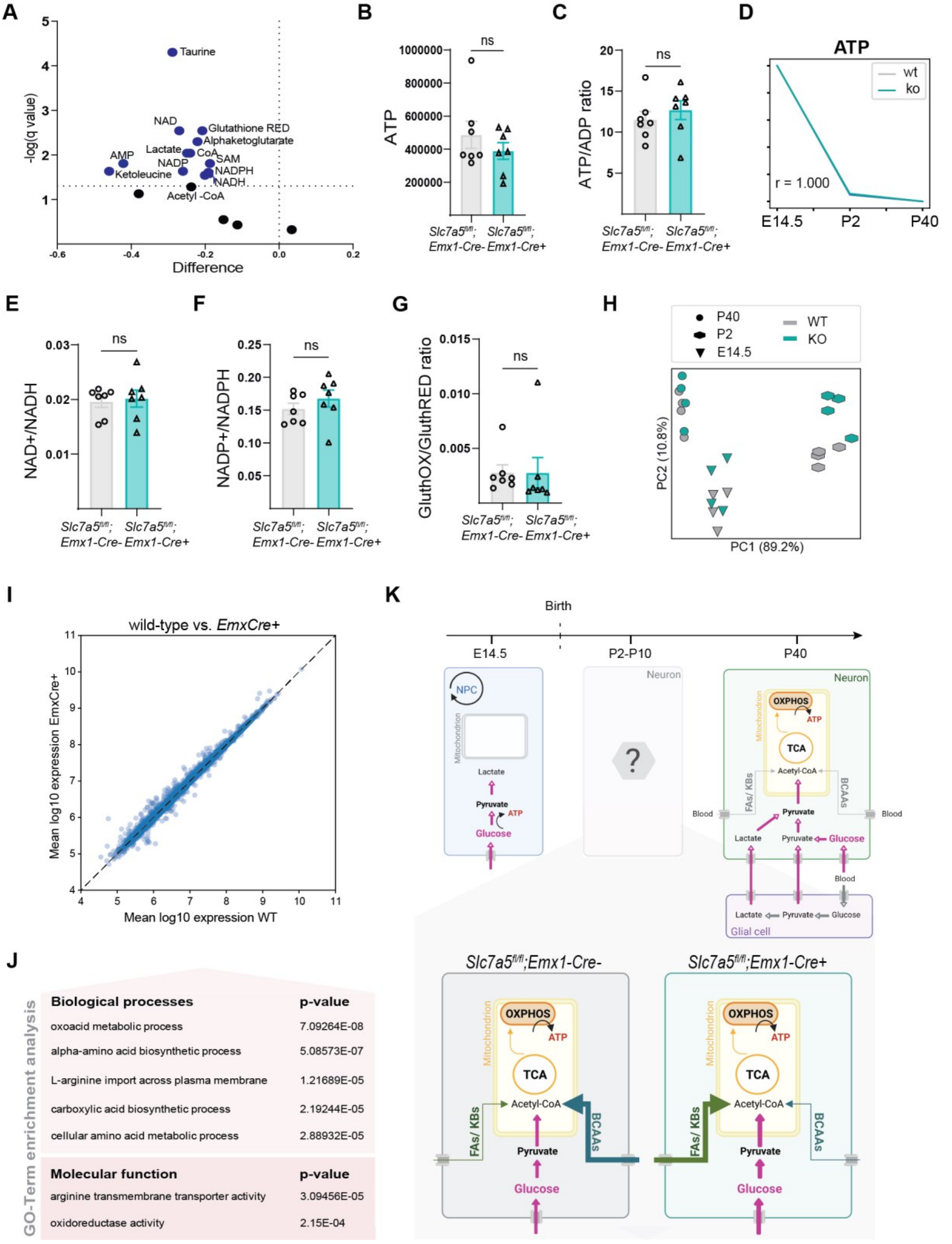

Biological processes	p-value
oxoacid metabolic process	7.09264E-08
alpha-amino acid biosynthetic process	5.08573E-07
L-arginine import across plasma membrane	1.21689E-05
carboxylic acid biosynthetic process	2.19244E-05
cellular amino acid metabolic process	2.88932E-05

Molecular function	p-value
arginine transmembrane transporter activity	3.09456E-05
oxidoreductase activity	2.15E-04

Figure S3. Cellular energy homeostasis is unaffected by the loss of *Slc7a5*, Related to Figure 14. (**A**) Volcano plot of intracellular levels of metabolic co-factors and key metabolites of ATP producing pathways (n=7 mice per genotype; $^{ns}p>0.05$; unpaired two-tailed *t*-test). Quantification of intracellular (**B**) ATP (means ± SD; n=7 mice per genotype; unpaired two-tailed *t*-test) (**C**) ATP/ADP ratio (means ± SD; n=7 mice per genotype; $^{ns}p>0.05$;

unpaired two-tailed *t*-test) and (**D**) ATP levels over the course of development in cortical tissue of *Slc7a5*$^{fl/fl}$*;Emx1-Cre+* and wild-type mice (n=5 mice per genotype and time point; Pearson's coefficient: r>0.9). (**E**) Intracellular NAD+/NADH and (**F**) NADP+/NADPH ratios are not changed in cortical cells of mutant mice (means ± SD; n=7 mice per genotype; ^{ns}*p>0.05;* unpaired two-tailed *t*-test). (**G**) The ratio of oxidized and reduced Glutathione is unaffected in cortical cells of mutant mice (means ± SD; n=7 mice per genotype; ^{ns}*p>0.05;* unpaired two-tailed *t*-test). (**H**) PCA plot of lipid-related metabolites detected in wild-type and mutant mice over time using an untargeted metabolomics approach (n=4 animals per genotype and time point). (**I**) Protein expression (mean log10 expression) levels in *Emx1-Cre+* vs. wild-type cortex (n=4 animals per genotype). (**J**) GO-term enrichment analysis of up-regulated genes of bulk RNA sequencing of *Slc7a5*$^{fl/fl}$*;Emx1-Cre+* cortex at P2 (Selected GO-terms: Supplementary data 5; n=3 mice per genotype). (**K**) Comparison of the perinatal metabolic states of *Slc7a5* mutant and wild-type neurons (FA: fatty acid; KB: ketone body; OXPHOS: oxidative phosphorylation).

Supplementary Figure 4

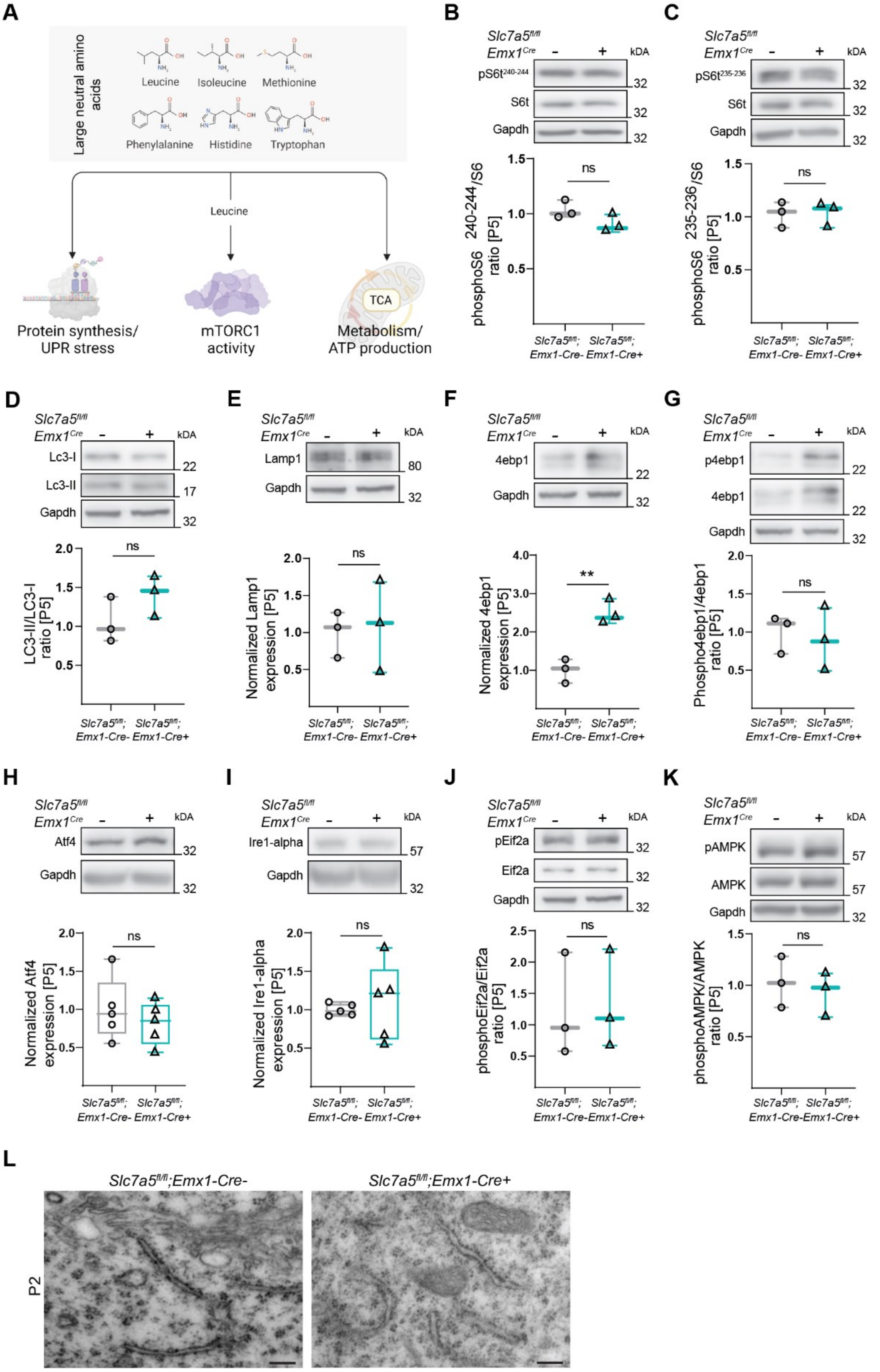

Figure S4. The mTOR, UPR and AMPK pathways are not affected in *Slc7a5* deficient mice, Related to Figure 14. (**A**) Scheme of the signaling pathways and cellular processes which are linked to LNAA levels. (**B-G**) Western blot analysis of markers used to quantify the state of the mTOR pathway and autophagy in P5 *Slc7a5*$^{fl/fl}$*;Emx1-Cre-*

and *Slc7a5$^{fl/fl}$;Emx1-Cre+* cortex. Ratio of normalized (**B**) phosphoS6$^{240\text{-}244}$/S6, (**C**) phosphoS6$^{235\text{-}236}$/S6, (**D**) LC3I/II protein levels and (**E**) normalized Lamp1. Normalized (**F**) 4ebp1 expression and (**G**) phospho4ebp1/4ebp1 ratio (n = 3 mice per genotype; ^{ns}*p>0.05; **p<0.01;* unpaired two-tailed *t*-test)**.** The state of the mTOR pathway is monitored by looking at the ratio between phosphorylated and non-phosphorylated 4ebp1, which is not changed in this case. (**H-J**) Western blot analysis of markers used to monitor the unfolded protein response (UPR) pathway. Quantification of (**H**) Atf4, (**I**) Ire-alpha expression levels and (**J**) phosphoEif2a/Eif2a ratio normalized to Gapdh (n=4 mice per genotype; ^{ns}*p>0.05*). (**K**) Normalized phosphoAMPK/AMPK ratio (n=3 mice per genotype; ^{ns}*p>0.05;* unpaired two-tailed *t*-test)**.** (**L**) Electron microscopy images of the endoplasmic reticulum (ER) showing unchanged ER morphology in mutant LII/III pyramidal neurons of P2 mutant mice (scale bar: 24000x).

Supplementary Figure 5

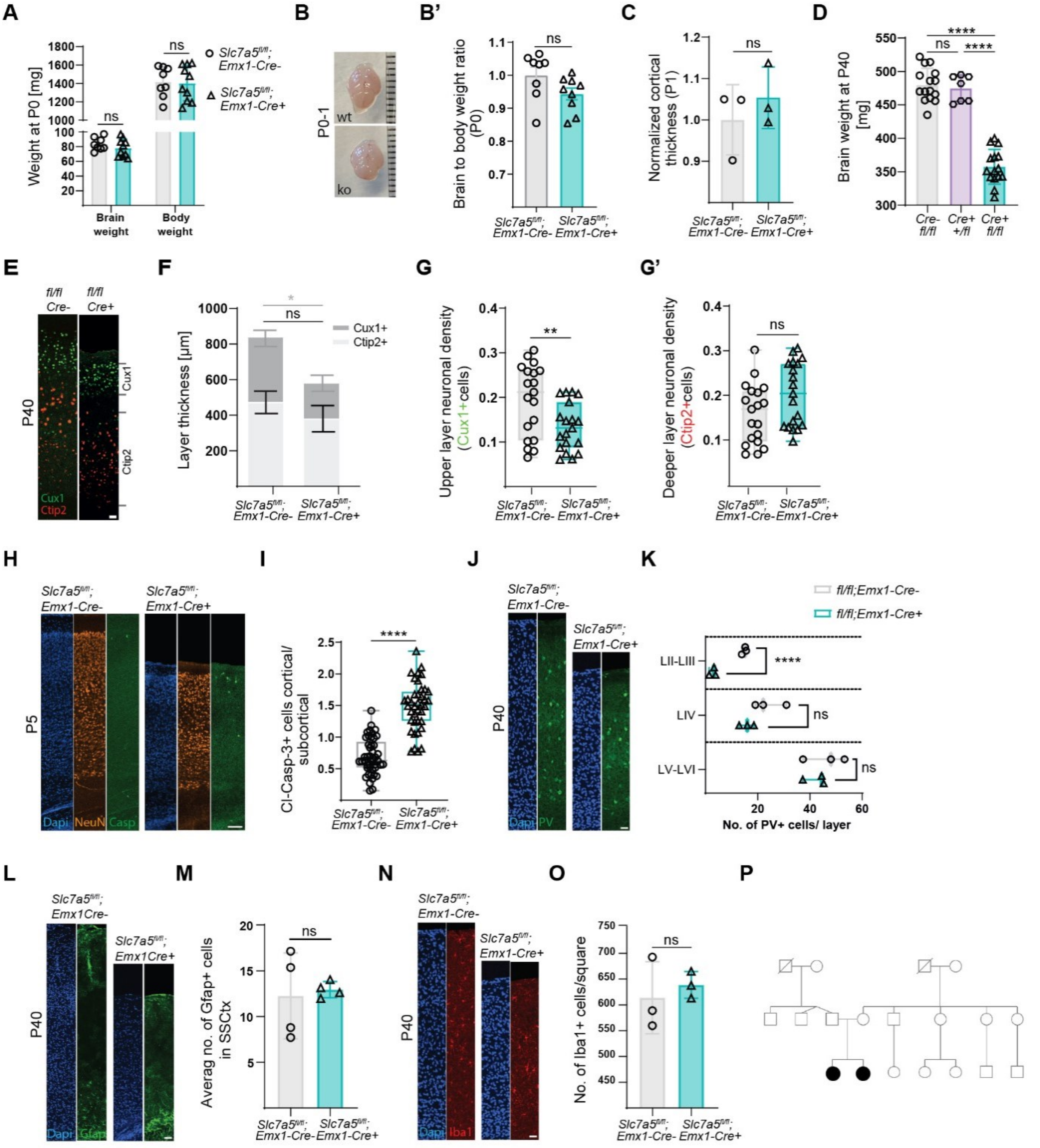

Figure S5. Characterization of the morphology and the cell-type composition of *Slc7a5*-deficient cortex, Related to Figure 15. (**A**) Brain and body weight of newborn *Slc7a5*$^{fl/fl}$*;Emx1-Cre+* and wild-type littermates (means ± SD; n=8 animals per genotype; $^{ns}p>0.05$, unpaired two-tailed *t*-test). (**B**) Images and (**B'**) quantification of brain to body weight ratio of newborn (P0-P1) *Slc7a5*$^{fl/fl}$*;Emx1-Cre+* and wild-type mice (means ± SD; n=9 animals per genotype; $^{ns}p>0.05$; unpaired two-tailed *t*-test; scale: 1mm). (**C**) Quantification of cortical thickness in newborn mutant and wild-type mice (means ± SD; n=3 animals per genotype; $^{ns}p>0.05$; unpaired two-tailed *t*-test). (**D**) Brain weight of adult (P40) *Slc7a5*$^{fl/fl}$*;Emx1-Cre+*, *Slc7a5*$^{fl/+}$*;Emx1-Cre+* and wild-type littermates (means ± SD; n>7 animals per genotype; $^{ns}p>0.05$; $^{****}p<0.0001$; unpaired two-tailed *t*-test). (**E**) Immunostaining for upper (Cux1) and lower (Ctip2) cortical layers in adult *Slc7a5*$^{fl/fl}$*;Emx1-Cre* mice (scale bar: 100μm). (**F-G'**) Quantification of layer thickness (**F**) and cell density (**G-G'**) in Cux1+ or Ctip2+ cell layers (means ± SD; n= 3 animals per genotype; n=19 quantification squares for the cell density; $^{**}p<0.01$; $^{ns}p>0.05$; unpaired two-tailed *t*-test). (**H**) Immunostaining and (**I**) quantification of the ratio of apoptotic cells in the cortex vs. subcortical regions of P5 mutant and wild-type mice (n=3 animals per genotype; $^{****}p<0.0001$; unpaired two-tailed *t*-test; scale bar: 100μm). (**J**) Immunostaining and (**K**) quantification of the number of inhibitory (parvalbumin+) neurons in the different layers of cortical columns of adult mutant and wild-type mice (n=3 animals per genotype; $^{****}p<0.0001$; $^{ns}p>0.05$; unpaired two-tailed *t*-test; scale bar: 100μm). (**L**) Immunostaining and (**M**) quantification of astrocytes (Gfap+) in cortical columns of adult mutant and wild-type mice (means ± SD; n=4 animals per genotype; $^{ns}p>0.05$; unpaired two-tailed *t*-test; scale bar: 100μm). (**N**) Immunostaining and (**O**) quantification of microglia (Iba1+) in cortical columns of adult mutant and wild-type mice (means ± SD; n=3 animals per genotype; $^{ns}p>0.05$; unpaired two-tailed *t*-test; scale bar: 100μm). (**P**) Pedigree displays a non-consanguineous background; two affected patients (solid symbols), and unaffected members (open symbols).

Supplementary Figure 6

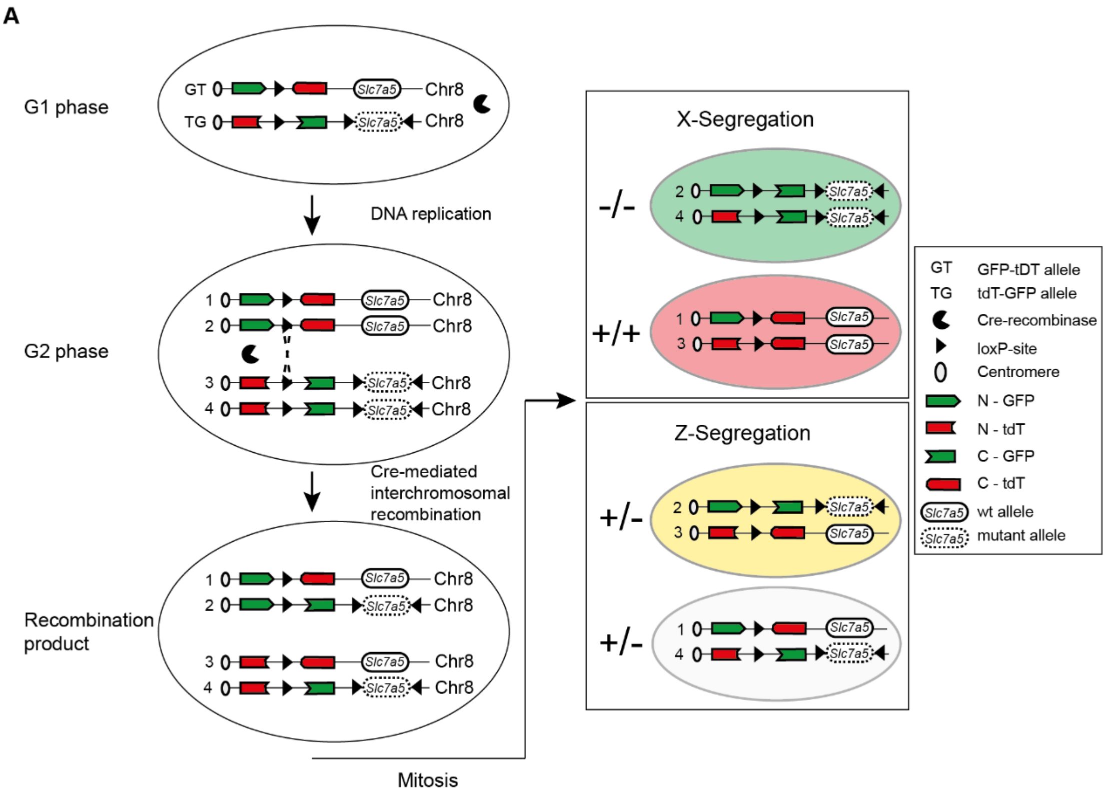

Figure S6. The mosaic analysis with double markers (MADM) principle, Related to Figure 16. (**A**) Schematic of the MADM technique. Two reciprocally chimeric marker genes (MADM-8-cassettes) are inserted at two identical loci close to the centromeres distal to the *Slc7a5* gene on chromosome 8. Each cassette consists of two split coding sequences of green fluorescent protein (eGFP) and red fluorescent protein (tdTomato; cassettes are referred to as GT and TG). The N- and C-terminals of each reporter gene are separated by an intron containing a loxP site. This ensures that the chimeric genes do not produce functional proteins in the absence of Cre recombinase. In the presence of Cre recombinase, cis-recombination induces the deletion of the *floxed* exon in the *Slc7a5* gene*,* thereby generating a *Slc7a5*-knock out. These recombination events can take place throughout all phases of the cell cycle. In G2, recombination in trans can mediate stochastic interchromosomal recombination events at the loxP sites of the MADM cassettes. This restores functional eGFP and tdTomato expression in sparse single cells. During mitosis, two potential types of chromosomal segregation can take place. X-segregation generates green daughter cells homozygous for the mutation (*Slc7a5*$^{-/-}$) and red cells homozygous for the wild-type allele (*Slc7a5*$^{+/+}$), thereby creating fluorescently labeled genetic mosaic mice. Z-segregation produces one daughter cell that resembles the parental cell (colorless) and a second daughter cell expressing both fluorescent proteins (double colored). Both cells are heterozygous for *Slc7a5* mutation.

Supplementary Figure 7

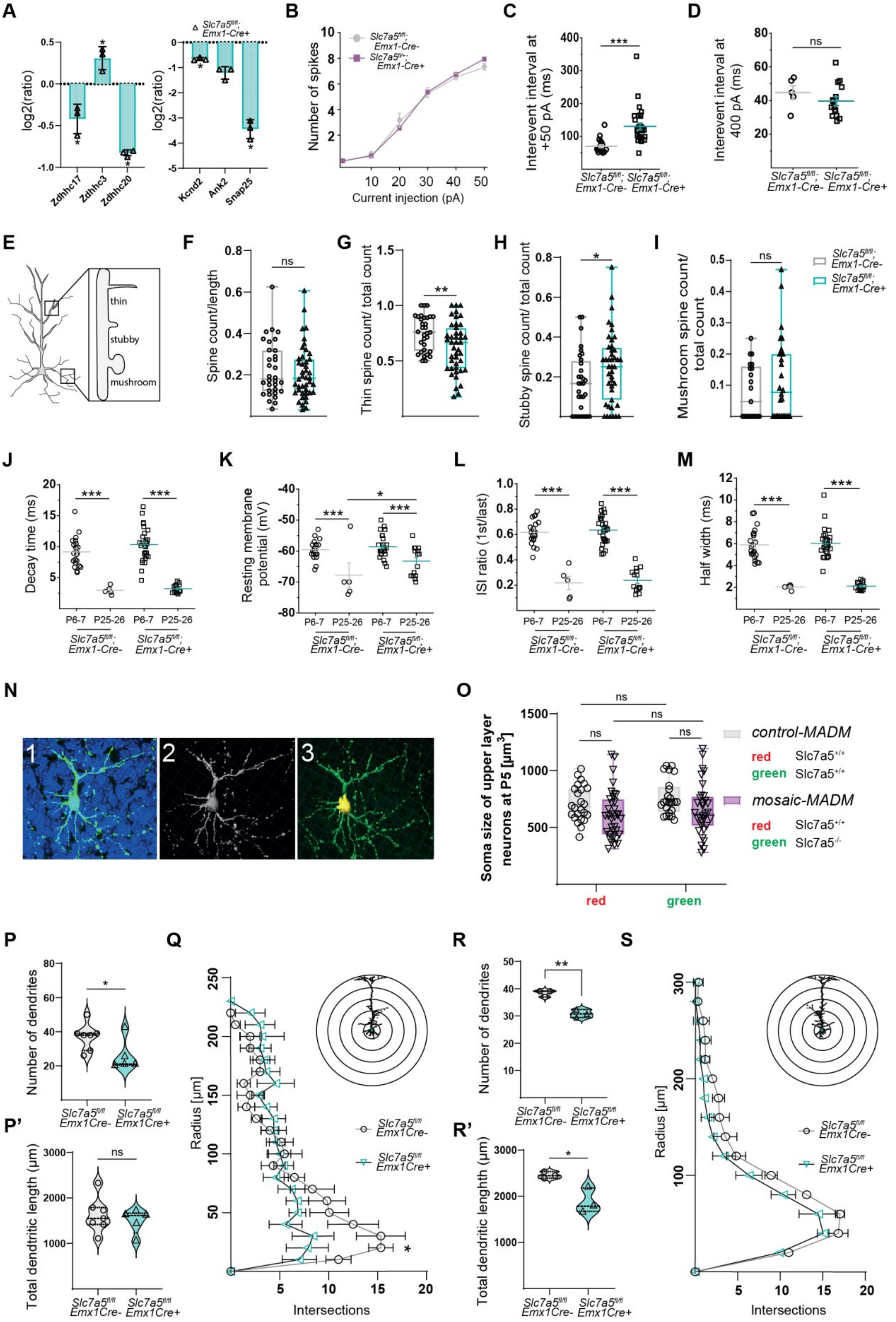

Figure S7. Electrophysiological properties of *Slc7a5*$^{fl/fl}$*;Emx1-Cre* mice, Related to Figure 17. (**A**) Fold change differences of proteins associated with the neuronal palmitoylation process of P5 *Slc7a5*$^{fl/fl}$*;Emx1-Cre+* compared to *Slc7a5*$^{fl/fl}$*;Emx1-Cre-* cortex (*significant; FDR threshold 1%, F-test). (**B**) Current clamp recordings from LII/III pyramidal neurons in *Slc7a5*$^{fl/+}$*;Emx1-Cre+* and *Slc7a5*$^{fl/fl}$*;Emx1-Cre-* SSCtx at P6-P7 (*Slc7a5*$^{fl/fl}$*;Emx1Cre-*: n = 12 cells / 2 mice; *Slc7a5*$^{fl/+}$*;Emx1-Cre+*: n = 16 cells / 2 mice; Two-way ANOVA: genotype F(1,167) = 0.004 ^{ns}p>0.5, current step F(5,167) = 162.11 ***p<0.001, interaction F(5,167) = 0.6 ^{ns}p>0.5. (**C-D**) Inter-spike interval measured in current clamp experiments from P6-P7 (**C**) and P25-P26 (**D**) LII/III pyramidal neurons of *Slc7a5*$^{fl/fl}$*;Emx1-Cre+* and *Emx1-Cre-* animals (*Slc7a5*$^{fl/fl}$*;Emx1-Cre-*: n = 22 cells / 3 mice; *Slc7a5*$^{fl/fl}$*;Emx1-Cre+*: n = 30 cells / 3 mice (P6-7); *Slc7a5*$^{fl/fl}$*;Emx1-Cre+*: n = 5 cells / 3 mice; *Slc7a5*$^{fl/fl}$*;Emx1-Cre-*: n = 15 cells / 3 mice (P25-26); ***p<0.001, unpaired two-tailed *t*-test). (**E**) Different dendritic spine classes represented on pyramidal neurons (thin, stubby, mushroom). (**F-I**) Analysis of the overall dendritic spine density (**F**) and the ratio of the different spine classes (**G-I**) of mutant and wild-type LII/III pyramidal neurons in the SSCtx at P6-7 (n= 3 mice per genotype, n>28 dendrites per mouse; ***p<0.01, *p<0.05, ^{ns}p>0.05*; unpaired two-tailed t-test). (**J**) Decay time, (**K**) resting membrane potential, (**L**) ISI ratio and (**M**) half width are not affected perinatally (*Slc7a5*$^{fl/fl}$*;Emx1-Cre-*: n = 22 cells / 3 mice; *Slc7a5*$^{fl/fl}$*;Emx1-Cre+*: n = 30 cells / 3 mice (P6-7); *Slc7a5*$^{fl/fl}$*;Emx1-Cre-*: n = 5 cells / 3 mice; *Slc7a5*$^{fl/fl}$*;Emx1-Cre+*: n = 15 cells / 3 mice (P25-26). Two-way ANOVA for AP decay time: genotype F(1,71) = 1.28 ^{ns}p>0.5, time point F(1,71) = 107.51 ***p<0.001, interaction F(1,71) = 0.5 ^{ns}p>0.5, Holm-Sidak post hoc ***p<0.001. Two-way ANOVA

6.2 Supplementary Tables

Supplementary Table S1.

Table S1. List of key resources.

REAGENT or RESOURCE	SOURCE	IDENTIFIER
Antibodies		
Rat monoclonal Anti-Ctip2	Abcam	Cat#ab18465
Rabbit polyclonal Anti-Cux1	Santa Cruz	Cat#sc-13024
Rabbit polyclonal Anti-Iba1	FUJIFILM Wako	Cat#019 19741
Rabbit monoclonal Anti-Gfap	Cell Signaling Technologies	Cat#12389
Mouse monoclonal Anti-Parvalbumin	Chemicon	Cat#MAB1572
Rabbit polyclonal Anti-Cleaved-Caspase-3	Cell Signaling Technologies	Cat#9661
Rabbit polyclonal Anti Human LAT1 (SLC7A5)	Transgenic Inc.	Cat#KE026
Rabbit polyclonal Anti-Gapdh	Millipore Merck	Cat#ABS16
Rabbit monoclonal Anti-S6 ribosomal protein	Cell Signaling Technologies	Cat#2217
Rabbit monoclonal Anti-phosphoS6 ribosomal protein$^{240-244}$	Cell Signaling Technologies	Cat#5364
Rabbit polyclonal Anti-phosphoS6 ribosomal protein$^{235-236}$	Cell Signaling Technologies	Cat#2211
Rabbit monoclonal Anti-4eibp1	Cell Signaling Technologies	Cat#9644
Rabbit monoclonal Anti-phospho4ebp1	Cell Signaling Technologies	Cat#2855
Rabbit polyclonal Anti-Atf4	Proteintech	Cat#10835-I-AP
Rabbit polyclonal Anti-Lamp1	Abcam	Cat#ab24170
Rabbit polyclonal Anti-Lc3-I/II	Millipore Merck	Cat#ABC929
Rabbit polyclonal Anti-Eif2a	Cell Signaling Technologies	Cat#9722
Rabbit polyclonal Anti-phosphoEif2a	Cell Signaling Technologies	Cat#9721
Rabbit polyclonal Anti-AMPK	Cell Signaling Technologies	Cat#2532
Rabbit monoclonal Anti-phosphoAMPK	Cell Signaling Technologies	Cat#2535
Rabbit normal IgG control	Cell Signaling Technologies	Cat#2729

Rabbit IgG HRP Linked Whole Ab	Cytiva	Cat#NA934
Donkey anti-Rabbit IgG (H+L) Highly Cross-Adsorbed Secondary Antibody, Alexa Fluor™ 488	Invitrogen™	Cat#A-21206
Goat anti-Rabbit IgG (H+L) Highly Cross-Adsorbed Secondary Antibody, Alexa Fluor™ 594	Invitrogen™	Cat#A-11037
Donkey anti-Rat IgG (H+L) Highly Cross-Adsorbed Secondary Antibody, Alexa Fluor™ 594	Invitrogen™	Cat#A-21209
Goat anti-Mouse IgG (H+L) Highly Cross-Adsorbed Secondary Antibody, Alexa Fluor™ Plus 488	Invitrogen™	Cat#A-32723
Streptavidin, Alexa Fluor™ 488 Conjugate	Invitrogen™	Cat#S32354
Chemicals, peptides, and recombinant proteins		
DAPI (4',6-Diamidino-2-Phenylindole, Dihydrochloride)	Invitrogen™	D1306
Cresyl Violet acetate	Sigma Aldrich	C5042
ROTI®Histol	Carl Roth	6640.1
Osmium tetroxide EM	Science Services	E19110
Uranyl acetate EM	AL-Labortechnik	77870.02
Propylene oxide EM	Sigma Aldrich	82320
Durucupan Component A	Sigma Aldrich	44611
Durucupan Component B	Sigma Aldrich	44611
Durucupan Component C	Sigma Aldrich	44611
Durucupan Component D	Sigma Aldrich	44611
IGEPAL® CA-630 (NP-40)	Sigma Aldrich	I3021
PPi (Sodium pyrophosphate dibasic)	Sigma Aldrich	71501
Sodium orthovanadate (Na3VO4)	Sigma Aldrich	S6508
Bromophenol Blue	Sigma Aldrich	B0126
Pierce™ DTT	Thermo Scientific™	20290
Methanol (hypergrade for LC-MS LiChrosolv®)	Supelco	1.06035
Acetonitrile (hypergrade for LC-MS LiChrosolv®)	Supelco	1.00029
Water (hypergrade for LC-MS LiChrosolv®)	Supelco	1.15333
Isopropanol (hypergrade for LC-MS)	EMD Millipore	1.02781
Formic acid (LC-MS LiChropur®)	Supelco	533002
Acetic acid (HPLC LiChropur®)	Supelco	543808
Ammonium hydroxide (25 %, w:v)	Supelco	105432
EquiSPLASH™ LIPIDOMIX® Quantitative Mass Spec Internal Standard	Avanti Polar Lipids	330731-1EA
Metabolomics amino acid mix standard	Cambridge Isotope Laboratories	MSK-A2-1.2
EBSS, no calcium, no magnesium, no phenol red	Gibco™	14155063
Bovine Serum Albumin	Sigma Aldrich	A9647
TRIzol™ Reagent	Invitrogen™	15596026
cOmplete™, Mini, EDTA-free Protease Inhibitor Cocktail	Roche	4693159001
Sodium chloride	VWR (Merck)	1.06404.1000
Sodium bicarbonate	VWR (Merck)	1.06329.1000
Potassium chloride	VWR (Merck)	26764.232
D-glucose	VWR (Merck)	1.08342.1000
Sucrose	Sigma Aldrich	16104
Magnesium chloride	Honeywell	M9272-1KG
Calcium chloride	VWR (Merck)	1.02382.0250
N-Methyl-D-glucamine	Sigma Aldrich	M2004-500G
HEPES	Sigma Aldrich	M3375-100G
di-Sodium hydrogen phosphate dihydrate	VWR (Merck)	1.06580.0500
(+)-Sodium L-ascorbate	Sigma Aldrich	11140-250G

Thiourea	Sigma Aldrich	T8656-50G
Sodium pyruvate	Sigma Aldrich	P2256-25G
Adenosine 5'-triphosphate magnesium salt	Sigma Aldrich	A9187-1G
Guanosine 5'-triphosphate sodium salt hydrate	Sigma Aldrich	G8877-100MG
EGTA	Sigma Aldrich	EO396-100G
Potassium D-gluconate	Sigma Aldrich	G4500-100G
Phosphocreatine disodium salt hydrate	Sigma Aldrich	P7936-5G
Critical commercial assays		
TruSeq Exome Library Kit	Illumina	20020614
Pierce™ ECL Western Blotting Substrate	Thermo Scientific™	32106
SuperSignal™ West Pico PLUS Chemiluminescent Substrate	Thermo Scientific™	34577
Papain Dissociation Kit	Worthington Biochemical Corp.	LK003150
Pierce™ BCA Protein Assay Kit	Thermo Scientific™	23227
QuantSeq FWD 3’ mRNA-Seq Library Prep Kits – with unique dual indexing	Lexogen	113-115 & 129-131
Agilent RNA 6000 Nano Kit	Agilent	5067-1511
Agilent High Sensitivity DNA Kit	Agilent	5067-4626
TMT10plex™ Isobaric Label Reagent Set	Thermo Scientific™	90406
iST-NHS kit	PreOmics GmbH	P.O.00026
RNA Clean & Concentrator-5 kit	Zymo Research	R1013
FD Rapid GolgiStain™ Kit	FDNeurotechnologies Inc.	PK401
RNAscope® Intro Pack for Multiplex Fluorescent Reagent Kit v2- Mm	ACD	323136
Deposited data		
Metabolomics & Lipidomics data	Knaus et al. 2023	MetaboLights: MTBLS6578
Proteomics data	Knaus et al. 2023	iProX: PXD038454
Bulk RNA sequencing data	Knaus et al. 2023	GEO: GSE218713
Single cell RNA sequencing data	Di Bella et al. 2021[423]; Yuan et al. 2022[424]	GEO: GSM4635077, GSM4635080, GSM4635081, GSM4635078, GSM4635079, GSM5277845, GSE204759
Code	Knaus et al. 2023	zenodo: https://doi.org/10.5281/zenodo.7358062
Experimental models: Organisms/strains		
Mouse: B6.129P2-Slc7a5tm1.1Daca/J	The Jackson Laboratory	027252
Mouse: B6.Cg-Tg(Tek-cre)1Ywa/J	The Jackson Laboratory	008863
Mouse: B6.129S2-Emx1tm1(cre)Krj/J	The Jackson Laboratory	005628
Mouse: Gt(ROSA)26Sortm4(ACTB-tdTomato,-EGFP)Luo/J	The Jackson Laboratory	007576
Mouse: MADM-8-GT	Contreras et al. 2021[389]	NA
Mouse: MADM-8-TG	Contreras et al. 2021	NA
Oligonucleotides		
qPCR primer_human: Q_SLC7A5_In2-3F: CGCTCATCAGATAGCCAGGAAA	Knaus et al. 2023	NA
qPCR primer_human: Q_SLC7A5_In2-3R: TTGAAGCCAAACAGGAGACAGG	Knaus et al. 2023	NA
qPCR primer_human: Q_SLC7A5_In4-5F: GTGTGTCCTTGAGCACGGTTTC	Knaus et al. 2023	NA
qPCR primer_human: Q_SLC7A5_In4-5R: CCTGAGAAATGGGGATTCTTCG	Knaus et al. 2023	NA

qPCR primer_human: Q_SLC7A5_In5-6F: CAGAGGAAGTGTCTGGGGATCA	Knaus et al. 2023	NA
qPCR primer_human: Q_SLC7A5_In5-6R: CCACTCTGTGGCAGACTCCAAT	Knaus et al. 2023	NA
qPCR primer_human: Q_SLC7A5_In5-6F2: AGTCCAGGGCAGAGGTCATTTTA	Knaus et al. 2023	NA
qPCR primer_human: Q_SLC7A5_In5-6R2: GAGTCAGAGCTTGTTCAGTAGGAAGC	Knaus et al. 2023	NA
qPCR primer_human: Q_SLC7A5_In7-8F ACCACATTTGGGTTAAGGACAGG	Knaus et al. 2023	NA
qPCR primer_human: Q_SLC7A5_In7-8F AGGTCCTGGCCCTTGCTTACTA	Knaus et al. 2023	NA
qPCR primer_human: Q_SLC7A5_3UTR_F: CCAAGAAAGCAGGGCTTCCTAA	Knaus et al. 2023	NA
qPCR primer_human: Q_SLC7A5_3UTR_R: GGTTTAATGTGCGTCTCCATGC	Knaus et al. 2023	NA
qPCR primer_human: Q_KLHDC4_In1-2F: TGACCTTGGGGTTGAGTGTTCT	Knaus et al. 2023	NA
qPCR primer_human: Q_KLHDC4_In1-2R: AGGGACAAAGGACTGTGGTCAA	Knaus et al. 2023	NA
qPCR primer_human: Q_KLHDC4_In4-5F: AGTGAATGACCTGTGTGGTCAGTG	Knaus et al. 2023	NA
qPCR primer_human: Q_KLHDC4_In4-5R: CTATGGGAGAAAAAGCCCTGGA	Knaus et al. 2023	NA
qPCR primer_human: Q_KLHDC4_In5-6F: TGGAGTCTGTGGAACTGTGAAGTG	Knaus et al. 2023	NA
qPCR primer_human: Q_KLHDC4_In5-6R: CCATGGAATGTCAACCAGAAGC	Knaus et al. 2023	NA
qPCR primer_human: Q_KLHDC4_In7-8F: TGAGCAAGTAGAGGTGGCTTGG	Knaus et al. 2023	NA
qPCR primer_human: Q_KLHDC4_In7-8R: GGTGAGCAGAAGGACAAGGACA	Knaus et al. 2023	NA
Genotyping primer – Slc7a5^{fl}; forward CCA TCT CGG CAG TTC CAG GC	Sinclair et al. 2013[402]	NA
Genotyping primer – Slc7a5^{fl}; reverse GGT GCT TTG CTG AAG GCA GGG	Sinclair et al. 2013	NA
Genotyping primer – recombination of floxed-exon1 (Slc7a5); forward CAG CTC CTT TCT CCA GTT AAG C	Knaus et al. 2023	NA
Genotyping primer – recombination of floxed-exon1 (Slc7a5); reverse GAC AGC CTG AAG TAA AAT TCC C	Knaus et al. 2023	NA
Genotyping primer – Cre recombinase; forward GTC CAA TTT ACT GAC CGT ACA CC	Knaus et al. 2023	NA
Genotyping primer – Cre recombinase; reverse GTT ATT CGG ATC ATC AGC TAC ACC	Knaus et al. 2023	NA
RNAscope® Probe - Mm-Slc7a5-E1 - musculus solute carrier family 7 member 5 (Slc7a5) mRNA	ACD	472571
RNAscope® Probe - Mm-Slc7a5 - Mus musculus solute carrier family 7 member 5 (Slc7a5) mRNA	ACD	461031
TSA Vivid650	Tocris	7536
Software and algorithms		
VarSeq	Golden Helix Inc®	https://www.goldenhelix.com/products/VarSeq/
ZEN Digital Imaging for Light Microscopy	Zeiss	http://www.zeiss.com/microscopy/en_us/products/microscope-software/zen.html#introduction
ImageJ	Schneider et al. 2012[404]	https://imagej.nih.gov/ij/

Graphpad Prism 9.0	Graphpad	https://www.graphpad.com/scientific-software/prism/
Imaris Microscopy Image Analysis Software	Oxford Instruments	https://imaris.oxinst.com/
MS-DIAL	Tsugawa et al. 2015[410]	NA
TraceFinder	Thermo Scientific™	https://www.thermofisher.com/at/en/home/industrial/mass-spectrometry/liquid-chromatography-mass-spectrometry-lc-ms/lc-ms-software/lc-ms-data-acquisition-software/tracefinder-software.html
Compound Discoverer Software 3.0	Thermo Fisher Scientific™	https://www.thermofisher.com
MaxQuant (1.6.17.0)	Tyanova et al. 2016[413]	https://www.maxquant.org/
limma package v4.2	Ritchie et al. 2015[414]	http://www.bioconductor.org
topGO v2.50.0	NA	http://www.bioconductor.org
R v4.1.2	NA	https://www.r-project.org/
Seurat v4.1.0	Hao et al. 2021[425]	http://www.bioconductor.org
GenBinomApps v1.2	NA	https://cran.r-project.org/package=GenBinomApps
Origin 2018 (64 bit)	Origin Lab	https://www.originlab.com/
Clampfit v10.7	Molecular Devices	https://support.moleculardevices.com/s/article/Axon-pCLAMP-10-Electrophysiology-Data-Acquisition-Analysis-Software-Download-Page
Clampex v10.7	Molecular Devices	https://support.moleculardevices.com/s/article/Axon-pCLAMP-10-Electrophysiology-Data-Acquisition-Analysis-Software-Download-Page
NeuronStudio	Wearne et al. 2005[426]	NA
Galaxy web platform	Afgan et al. 2018[416]	https://usegalaxy.org/
STAR v2.5.4	Dobin et al. 2013[415]	https://github.com/alexdobin/STAR
DESeq2 v1.34.0	Love et al. 2014[417]	http://www.bioconductor.org
GOstats v2.36.0	Falcon et al. 2007[418]	http://www.bioconductor.org
FASTX toolkit v0.0.14	Hannon Lab	http://hannonlab.cshl.edu/fastx_toolkit/
Huygens Professional software v15.0	Scientific Volume Imaging	https://svi.nl/HomePage
EthoVision XT 11.5	Noldus	https://www.noldus.com/ethovision-xt

Python 3.9.4	conda	https://www.python.org/
Scikit-learn 1.1.2	Pedregosa et al. 2011[421]	https://scikit-learn.org/stable/index.html
Pandas 1.3.5	McKinney et al. 2010[407]	https://pandas.pydata.org/
numpy 1.22.4	Harris et al. 2020[408]	https://numpy.org/
statsmodels 0.13.1	Seabold et al. 2010[409]	https://www.statsmodels.org/stable/index.html
Scipy 1.7.3	Virtanen et al. 2020[422]	https://scipy.org/
Seaborn 0.11.2	Waskom et al. 2021[419]	https://seaborn.pydata.org/
Python-ternary 1.0.8	PyPI	https://github.com/marcharper/python-ternary
thefuzz 0.19.0	PyPI	https://github.com/seatgeek/thefuzz
Python-levenshtein 0.12.2	PyPI	https://github.com/ztane/python-Levenshtein/
Matplotlib 3.5.2	Hunter et al. 2007[420]	https://matplotlib.org/
Jupyterlab 3.5.0	PyPI	https://jupyter.org/
Other		
CFX Connect™ Real-Time PCR Detection System	Bio-Rad	1855201
Immobilon®-P PVDF Membrane	Millipore	IPVH00010
Tissue-Tek® O.C.T. Compound	Sakura® Finetek	4583
DAKO fluorescent mounting medium	Dako	S3023
DPX Mountant for histology	Sigma-Aldrich	06522
SuperFrost Plus™ Adhesion slides	Epredia™	10149870
ProLong™ Gold Antifade Mountant	Invitrogen™	P36930
Disposable pestles	Bel-Art®	BAF199230001
iHILIC®-(P) Classic, PEEK column, (100mm x 2.1mm, 5µm) with a precolumn	HILICON	160.102.0520
ACQUITY UPLC HSS T3 column (150 mm x 2.1 mm; 1.8 µm)	Waters Corporation	186009492
50-ml TPP® TubeSpin Bioreactor tubes	Merck	Z761028
TC20 Automated Cell Counter (Bio-Rad)	Bio-Rad	NA
Atlantis Premier BEH Z-HILIC column (2.1 mm x 100 mm, 1.7 µm)	Waters Corporation	186009979
ACQUITY Premier CSH C18 column (2.1 mm x 100 mm, 1.7 µm)	Waters Corporation	186009461
Protein A Magnetic Beads	Abcam	ab214286
DynaMag™-2 Magnet	Invitrogen™	12321D
Protein Extraction beads	Diagenode	C20000021
13.2ml Thinwall Ultra-Clear™ Tubes	Beckmann Coulter	344059
GEN1 uPAC column	Pharmafluidics	NA
BX-51WI microscope	Olympus	NA
QIClickTM charge-coupled device camera	Q Imaging Inc.	NA
Nikon Eclipse Ti2	Nikon	NA
LSM800 Confocal	Zeiss	NA
SlideScanner VS120	Olympus	NA
Sliding Microtome SM2010R	Leica	NA
Cryostat Cryostar NX70	Thermo Scientific™	NA
Vibratome Leica VT 1200S	Leica	NA

BioWave Pro+ microwave	Pelco	36700
Ultramicrotom UC7	Leica	NA
Amersham Imager 680	GE Healthcare	NA

Supplementary Table S2.

Table S2. Overview of previously published and novel patients with biallelic pathogenic variants in the *SLC7A5* gene, Related to Figure 15.

Patient-ID	**1426-5**	**1426-6**	**1426-8**	**1426-19**	**1465-3**	**1465-4**	**130-1**	**130-2**
Reference	Tărlungeanu et al., 2016						This study	
SLC7A5 pathogenic variant(s)	c.737C>T p.(Ala246Val)				c.1124C>T p.(Pro375Leu)		c.1124C>T, p.(Pro375Leu) Deletion exons 5-10	
Variant zygosity	Homozygous				Homozygous		Compound heterozygous	
Phenotypic characteristics								
Gender	F	M	F	M	M	M	F	F
Growth retardation	n/a	n/a	n/a	n/a	n/a	n/a	+	+
HC at birth (SD)	n/a	-2/-3	n/a	n/a	-3	-3	-3	-2.5
HC at latest examination (SD)	-5	-2.3	-5.5	-5	n/a	n/a	-7	-6
GDD (motor, speech, cognitive)	+	+	+	+	+	+	+	+
Seizures (onset)	-	-	-	n/a	+ (1y)	+ (6mo)	+ (3y)	+ (6y)
Autistic features	+	+	+	n/a	+	+	-	+
Brain MRI	n/a	Cortical atrophy	Normal	n/a	Thin CC		Pontocerebellar and CC hypoplasia	

HC: head circumference, SD: standard deviation, GDD: global developmental delay, n/a: not available, CC: corpus callosum

References

1. Azevedo, F.A.C., Carvalho, L.R.B., Grinberg, L.T., Farfel, J.M., Ferretti, R.E.L., Leite, R.E.P., Jacob Filho, W., Lent, R., and Herculano-Houzel, S. (2009). Equal numbers of neuronal and nonneuronal cells make the human brain an isometrically scaled-up primate brain. J Comp Neurol *513*, 532–541. 10.1002/cne.21974.

2. Herculano-Houzel, S. (2009). The Human Brain in Numbers: A Linearly Scaled-up Primate Brain. Front Hum Neurosci *3*, 31. 10.3389/neuro.09.031.2009.

3. Lui, J.H., Hansen, D.V., and Kriegstein, A.R. (2011). Development and Evolution of the Human Neocortex. Cell *146*, 18–36. 10.1016/j.cell.2011.06.030.

4. Lodato, S., and Arlotta, P. (2015). Generating Neuronal Diversity in the Mammalian Cerebral Cortex. Annu Rev Cell Dev Biol *31*, 699–720. 10.1146/annurev-cellbio-100814-125353.

5. Stiles, J., and Jernigan, T.L. (2010). The Basics of Brain Development. Neuropsychol Rev *20*, 327–348. 10.1007/s11065-010-9148-4.

6. Reemst, K., Noctor, S.C., Lucassen, P.J., and Hol, E.M. (2016). The Indispensable Roles of Microglia and Astrocytes during Brain Development. Frontiers in Human Neuroscience *10*.

7. Adnani, L., Han, S., Li, S., Mattar, P., and Schuurmans, C. (2018). Mechanisms of Cortical Differentiation. Int Rev Cell Mol Biol *336*, 223–320. 10.1016/bs.ircmb.2017.07.005.

8. Kwan, K.Y., Sestan, N., and Anton, E.S. (2012). Transcriptional co-regulation of neuronal migration and laminar identity in the neocortex. Development *139*, 1535–1546. 10.1242/dev.069963.

9. Campbell, K. (2005). Cortical Neuron Specification: It Has Its Time and Place. Neuron *46*, 373–376. 10.1016/j.neuron.2005.04.014.

10. Namba, T., and Huttner, W.B. (2017). Neural progenitor cells and their role in the development and evolutionary expansion of the neocortex. Wiley Interdiscip Rev Dev Biol *6*. 10.1002/wdev.256.

11. Hébert, J.M., and Fishell, G. (2008). The genetics of early telencephalon patterning: some assembly required. Nat Rev Neurosci *9*, 678–685. 10.1038/nrn2463.

12. Menassa, D.A., and Gomez-Nicola, D. (2018). Microglial Dynamics During Human Brain Development. Frontiers in Immunology *9*.

13. Taverna, E., Götz, M., and Huttner, W.B. (2014). The cell biology of neurogenesis: toward an understanding of the development and evolution of the neocortex. Annu Rev Cell Dev Biol *30*, 465–502. 10.1146/annurev-cellbio-101011-155801.

14. Matsuzaki, F., and Shitamukai, A. (2015). Cell Division Modes and Cleavage Planes of Neural Progenitors during Mammalian Cortical Development. Cold Spring Harb Perspect Biol *7*, a015719. 10.1101/cshperspect.a015719.

15. Borrell, V., and Götz, M. (2014). Role of radial glial cells in cerebral cortex folding. Curr Opin Neurobiol *27*, 39–46. 10.1016/j.conb.2014.02.007.

16. Jones, E.G. (1986). Neurotransmitters in the cerebral cortex. J Neurosurg *65*, 135–153. 10.3171/jns.1986.65.2.0135.

17. Lim, L., Mi, D., Llorca, A., and Marín, O. (2018). Development and Functional Diversification of Cortical Interneurons. Neuron *100*, 294–313. 10.1016/j.neuron.2018.10.009.

18. Chini, M., and Hanganu-Opatz, I.L. (2021). Prefrontal Cortex Development in Health and Disease: Lessons from Rodents and Humans. Trends in Neurosciences *44*, 227–240. 10.1016/j.tins.2020.10.017.

19. Tasic, B., Yao, Z., Graybuck, L.T., Smith, K.A., Nguyen, T.N., Bertagnolli, D., Goldy, J., Garren, E., Economo, M.N., Viswanathan, S., et al. (2018). Shared and distinct transcriptomic cell types across neocortical areas. Nature *563*, 72–78. 10.1038/s41586-018-0654-5.

20. Tasic, B., Menon, V., Nguyen, T.N., Kim, T.K., Jarsky, T., Yao, Z., Levi, B., Gray, L.T., Sorensen, S.A., Dolbeare, T., et al. (2016). Adult mouse cortical cell taxonomy revealed by single cell transcriptomics. Nat Neurosci *19*, 335–346. 10.1038/nn.4216.

21. Hodge, R.D., Bakken, T.E., Miller, J.A., Smith, K.A., Barkan, E.R., Graybuck, L.T., Close, J.L., Long, B., Johansen, N., Penn, O., et al. (2019). Conserved cell types with divergent features in human versus mouse cortex. Nature *573*, 61–68. 10.1038/s41586-019-1506-7.

22. Peng, H., Xie, P., Liu, L., Kuang, X., Wang, Y., Qu, L., Gong, H., Jiang, S., Li, A., Ruan, Z., et al. (2021). Morphological diversity of single neurons in molecularly defined cell types. Nature *598*, 174–181. 10.1038/s41586-021-03941-1.

23. Wong, F.K., and Marín, O. (2019). Developmental Cell Death in the Cerebral Cortex. Annu Rev Cell Dev Biol *35*, 523–542. 10.1146/annurev-cellbio-100818-125204.

24. Blanquie, O., Kilb, W., Sinning, A., and Luhmann, H.J. (2017). Homeostatic interplay between electrical activity and neuronal apoptosis in the developing neocortex. Neuroscience *358*, 190–200. 10.1016/j.neuroscience.2017.06.030.

25. Yeo, W., and Gautier, J. (2004). Early neural cell death: dying to become neurons. Dev Biol *274*, 233–244. 10.1016/j.ydbio.2004.07.026.

26. Blaschke, A.J., Weiner, J.A., and Chun, J. (1998). Programmed cell death is a universal feature of embryonic and postnatal neuroproliferative regions throughout the central nervous system. J Comp Neurol *396*, 39–50. 10.1002/(sici)1096-9861(19980622)396:1<39::aid-cne4>3.0.co;2-j.

27. Mihalas, A.B., and Hevner, R.F. (2018). Clonal analysis reveals laminar fate multipotency and daughter cell apoptosis of mouse cortical intermediate progenitors. Development *145*, dev164335. 10.1242/dev.164335.

28. Blanquie, O., Yang, J.-W., Kilb, W., Sharopov, S., Sinning, A., and Luhmann, H.J. (2017). Electrical activity controls area-specific expression of neuronal apoptosis in the mouse developing cerebral cortex. Elife *6*, e27696. 10.7554/eLife.27696.

29. Wong, F.K., Bercsenyi, K., Sreenivasan, V., Portalés, A., Fernández-Otero, M., and Marín, O. (2018). Pyramidal cell regulation of interneuron survival sculpts cortical networks. Nature *557*, 668–673. 10.1038/s41586-018-0139-6.

30. Hu, J.S., Vogt, D., Lindtner, S., Sandberg, M., Silberberg, S.N., and Rubenstein, J.L.R. (2017). Coup-TF1 and Coup-TF2 control subtype and laminar identity of MGE-derived neocortical interneurons. Development *144*, 2837–2851. 10.1242/dev.150664.

31. Pilaz, L.-J., McMahon, J.J., Miller, E.E., Lennox, A.L., Suzuki, A., Salmon, E., and Silver, D.L. (2016). Prolonged Mitosis of Neural Progenitors Alters Cell Fate in the Developing Brain. Neuron *89*, 83–99. 10.1016/j.neuron.2015.12.007.

32. Rehen, S.K., McConnell, M.J., Kaushal, D., Kingsbury, M.A., Yang, A.H., and Chun, J. (2001). Chromosomal variation in neurons of the developing and adult mammalian nervous system. Proc Natl Acad Sci U S A *98*, 13361–13366. 10.1073/pnas.231487398.

33. Peterson, S.E., Yang, A.H., Bushman, D.M., Westra, J.W., Yung, Y.C., Barral, S., Mutoh, T., Rehen, S.K., and Chun, J. (2012). Aneuploid cells are differentially susceptible to caspase-

mediated death during embryonic cerebral cortical development. J Neurosci *32*, 16213–16222. 10.1523/JNEUROSCI.3706-12.2012.

34. van Dyck, L.I., and Morrow, E.M. (2017). Genetic control of postnatal human brain growth. Curr Opin Neurol *30*, 114–124. 10.1097/WCO.0000000000000405.

35. Farhy-Tselnicker, I., and Allen, N.J. (2018). Astrocytes, neurons, synapses: a tripartite view on cortical circuit development. Neural Development *13*, 7. 10.1186/s13064-018-0104-y.

36. Nishiyama, A., Shimizu, T., Sherafat, A., and Richardson, W.D. (2021). Life-long oligodendrocyte development and plasticity. Seminars in Cell & Developmental Biology *116*, 25–37. 10.1016/j.semcdb.2021.02.004.

37. Miller, F.D., and Gauthier, A.S. (2007). Timing is everything: making neurons versus glia in the developing cortex. Neuron *54*, 357–369. 10.1016/j.neuron.2007.04.019.

38. Felix, L., Stephan, J., and Rose, C.R. (2021). Astrocytes of the early postnatal brain. European Journal of Neuroscience *54*, 5649–5672. 10.1111/ejn.14780.

39. Fu, Y., Yang, M., Yu, H., Wang, Y., Wu, X., Yong, J., Mao, Y., Cui, Y., Fan, X., Wen, L., et al. (2021). Heterogeneity of glial progenitor cells during the neurogenesis-to-gliogenesis switch in the developing human cerebral cortex. Cell Reports *34*. 10.1016/j.celrep.2021.108788.

40. Ge, W.-P., Miyawaki, A., Gage, F.H., Jan, Y.N., and Jan, L.Y. (2012). Local generation of glia is a major astrocyte source in postnatal cortex. Nature *484*, 376–380. 10.1038/nature10959.

41. Bandeira, F., Lent, R., and Herculano-Houzel, S. (2009). Changing numbers of neuronal and non-neuronal cells underlie postnatal brain growth in the rat. Proceedings of the National Academy of Sciences *106*, 14108–14113. 10.1073/pnas.0804650106.

42. Mason, S. (2017). Lactate Shuttles in Neuroenergetics-Homeostasis, Allostasis and Beyond. Front Neurosci *11*, 43. 10.3389/fnins.2017.00043.

43. Jha, M.K., and Morrison, B.M. (2018). Glia-neuron energy metabolism in health and diseases: New insights into the role of nervous system metabolic transporters. Exp Neurol *309*, 23–31. 10.1016/j.expneurol.2018.07.009.

44. Turner, D.A., and Adamson, D.C. (2011). Neuronal-Astrocyte Metabolic Interactions: Understanding the Transition into Abnormal Astrocytoma Metabolism. J Neuropathol Exp Neurol *70*, 167–176. 10.1097/NEN.0b013e31820e1152.

45. Chuquet, J., Quilichini, P., Nimchinsky, E.A., and Buzsáki, G. (2010). Predominant Enhancement of Glucose Uptake in Astrocytes versus Neurons during Activation of the Somatosensory Cortex. J. Neurosci. *30*, 15298–15303. 10.1523/JNEUROSCI.0762-10.2010.

46. Michalski, J.-P., and Kothary, R. (2015). Oligodendrocytes in a Nutshell. Frontiers in Cellular Neuroscience *9*.

47. Philips, T., and Rothstein, J.D. (2017). Oligodendroglia: metabolic supporters of neurons. J Clin Invest *127*, 3271–3280. 10.1172/JCI90610.

48. Harry, G.J. (2013). Microglia During Development and Aging. Pharmacol Ther *139*, 313–326. 10.1016/j.pharmthera.2013.04.013.

49. Südhof, T.C. (2018). Towards an Understanding of Synapse Formation. Neuron *100*, 276–293. 10.1016/j.neuron.2018.09.040.

50. Petzoldt, A.G., and Sigrist, S.J. (2014). Synaptogenesis. Curr Biol *24*, R1076-1080. 10.1016/j.cub.2014.10.024.

51. Blue, M.E., and Parnavelas, J.G. (1983). The formation and maturation of synapses in the visual cortex of the rat. I. Qualitative analysis. J Neurocytol *12*, 599–616. 10.1007/BF01181526.

52. Li, M., Cui, Z., Niu, Y., Liu, B., Fan, W., Yu, D., and Deng, J. (2010). Synaptogenesis in the developing mouse visual cortex. Brain Res Bull *81*, 107–113. 10.1016/j.brainresbull.2009.08.028.

53. Bourgeois, J.P., and Rakic, P. (1993). Changes of synaptic density in the primary visual cortex of the macaque monkey from fetal to adult stage. J Neurosci *13*, 2801–2820. 10.1523/JNEUROSCI.13-07-02801.1993.

54. O'Kusky, J., and Colonnier, M. (1982). Postnatal changes in the number of neurons and synapses in the visual cortex (area 17) of the macaque monkey: a stereological analysis in normal and monocularly deprived animals. J Comp Neurol *210*, 291–306. 10.1002/cne.902100308.

55. O'Kusky, J.R. (1985). Synapse elimination in the developing visual cortex: a morphometric analysis in normal and dark-reared cats. Brain Res *354*, 81–91. 10.1016/0165-3806(85)90071-9.

56. Winfield, D.A. (1981). The postnatal development of synapses in the visual cortex of the cat and the effects of eyelid closure. Brain Research *206*, 166–171. 10.1016/0006-8993(81)90110-4.

57. Aoki, C., and Erisir, A. (2014). Chapter Thirteen - Experience-Dependent Synaptic Plasticity in the Developing Cerebral Cortex. In The Synapse, V. Pickel and M. Segal, eds. (Academic Press), pp. 397–445. 10.1016/B978-0-12-418675-0.00013-4.

58. Aghajanian, G.K., and Bloom, F.E. (1967). The formation of synaptic junctions in developing rat brain: a quantitative electron microscopic study. Brain Res *6*, 716–727. 10.1016/0006-8993(67)90128-x.

59. Luhmann, H.J., Sinning, A., Yang, J.-W., Reyes-Puerta, V., Stüttgen, M.C., Kirischuk, S., and Kilb, W. (2016). Spontaneous Neuronal Activity in Developing Neocortical Networks: From Single Cells to Large-Scale Interactions. Frontiers in Neural Circuits *10*.

60. Crépel, V., Aronov, D., Jorquera, I., Represa, A., Ben-Ari, Y., and Cossart, R. (2007). A Parturition-Associated Nonsynaptic Coherent Activity Pattern in the Developing Hippocampus. Neuron *54*, 105–120. 10.1016/j.neuron.2007.03.007.

61. Yuste, R., Nelson, D.A., Rubin, W.W., and Katz, L.C. (1995). Neuronal domains in developing neocortex: Mechanisms of coactivation. Neuron *14*, 7–17. 10.1016/0896-6273(95)90236-8.

62. Dupont, E., Hanganu, I.L., Kilb, W., Hirsch, S., and Luhmann, H.J. (2006). Rapid developmental switch in the mechanisms driving early cortical columnar networks. Nature *439*, 79–83. 10.1038/nature04264.

63. Khazipov, R., and Luhmann, H.J. (2006). Early patterns of electrical activity in the developing cerebral cortex of humans and rodents. Trends Neurosci *29*, 414–418. 10.1016/j.tins.2006.05.007.

64. Egorov, A.V., and Draguhn, A. (2013). Development of coherent neuronal activity patterns in mammalian cortical networks: common principles and local hetereogeneity. Mech Dev *130*, 412–423. 10.1016/j.mod.2012.09.006.

65. Yang, J.-W., An, S., Sun, J.-J., Reyes-Puerta, V., Kindler, J., Berger, T., Kilb, W., and Luhmann, H.J. (2013). Thalamic network oscillations synchronize ontogenetic columns in the newborn rat barrel cortex. Cereb Cortex *23*, 1299–1316. 10.1093/cercor/bhs103.

66. An, S., Kilb, W., and Luhmann, H.J. (2014). Sensory-Evoked and Spontaneous Gamma and Spindle Bursts in Neonatal Rat Motor Cortex. J Neurosci *34*, 10870–10883. 10.1523/JNEUROSCI.4539-13.2014.

67. Golshani, P., Gonçalves, J.T., Khoshkhoo, S., Mostany, R., Smirnakis, S., and Portera-Cailliau, C. (2009). Internally Mediated Developmental Desynchronization of Neocortical Network Activity. J Neurosci *29*, 10890–10899. 10.1523/JNEUROSCI.2012-09.2009.

68. Luhmann, H.J., and Khazipov, R. (2018). Neuronal activity patterns in the developing barrel cortex. Neuroscience *368*, 256–267. 10.1016/j.neuroscience.2017.05.025.

69. Denaxa, M., Neves, G., Rabinowitz, A., Kemlo, S., Liodis, P., Burrone, J., and Pachnis, V. (2018). Modulation of Apoptosis Controls Inhibitory Interneuron Number in the Cortex. Cell Reports *22*, 1710. 10.1016/j.celrep.2018.01.064.

70. Priya, R., Paredes, M.F., Karayannis, T., Yusuf, N., Liu, X., Jaglin, X., Graef, I., Alvarez-Buylla, A., and Fishell, G. (2018). Activity Regulates Cell Death within Cortical Interneurons through a Calcineurin-Dependent Mechanism. Cell Rep *22*, 1695–1709. 10.1016/j.celrep.2018.01.007.

71. Southwell, D.G., Paredes, M.F., Galvao, R.P., Jones, D.L., Froemke, R.C., Sebe, J.Y., Alfaro-Cervello, C., Tang, Y., Garcia-Verdugo, J.M., Rubenstein, J.L., et al. (2012). Intrinsically determined cell death of developing cortical interneurons. Nature *491*, 109–113. 10.1038/nature11523.

72. Huang, E.J., and Reichardt, L.F. (2001). Neurotrophins: Roles in Neuronal Development and Function. Annual review of neuroscience *24*, 677. 10.1146/annurev.neuro.24.1.677.

73. Ikonomidou, C., Bosch, F., Miksa, M., Bittigau, P., Vöckler, J., Dikranian, K., Tenkova, T.I., Stefovska, V., Turski, L., and Olney, J.W. (1999). Blockade of NMDA Receptors and Apoptotic Neurodegeneration in the Developing Brain. Science *283*, 70–74. 10.1126/science.283.5398.70.

74. Wagner-Golbs, A., and Luhmann, H.J. (2012). Activity-dependent survival of developing neocortical neurons depends on PI3K signalling. Journal of Neurochemistry *120*, 495–501. 10.1111/j.1471-4159.2011.07591.x.

75. Dekkers, M.P.J., Nikoletopoulou, V., and Barde, Y.-A. (2013). Cell biology in neuroscience: Death of developing neurons: new insights and implications for connectivity. J Cell Biol *203*, 385–393. 10.1083/jcb.201306136.

76. Anastasiades, P.G., Marques-Smith, A., Lyngholm, D., Lickiss, T., Raffiq, S., Kätzel, D., Miesenböck, G., and Butt, S.J.B. (2016). GABAergic interneurons form transient layer-specific circuits in early postnatal neocortex. Nature Communications *7*. 10.1038/ncomms10584.

77. Oyarzabal, A., and Marin-Valencia, I. (2019). Synaptic energy metabolism and neuronal excitability, in sickness and health. Journal of Inherited Metabolic Disease *42*, 220–236. 10.1002/jimd.12071.

78. Jakkamsetti, V., Marin-Valencia, I., Ma, Q., Good, L.B., Terrill, T., Rajasekaran, K., Pichumani, K., Khemtong, C., Hooshyar, M.A., Sundarrajan, C., et al. (2019). Brain metabolism modulates neuronal excitability in a mouse model of pyruvate dehydrogenase deficiency. Science Translational Medicine *11*, eaan0457. 10.1126/scitranslmed.aan0457.

79. Lutas, A., and Yellen, G. (2013). The ketogenic diet: metabolic influences on brain excitability and epilepsy. Trends in Neurosciences *36*, 32–40. 10.1016/j.tins.2012.11.005.

80. Dehay, C., Kennedy, H., and Kosik, K.S. (2015). The Outer Subventricular Zone and Primate-Specific Cortical Complexification. Neuron *85*, 683–694. 10.1016/j.neuron.2014.12.060.

81. Raichle, M.E., and Gusnard, D.A. (2002). Appraising the brain's energy budget. Proceedings of the National Academy of Sciences *99*, 10237–10239. 10.1073/pnas.172399499.

82. Mergenthaler, P., Lindauer, U., Dienel, G.A., and Meisel, A. (2013). Sugar for the brain: the role of glucose in physiological and pathological brain function. Trends Neurosci *36*, 587–597. 10.1016/j.tins.2013.07.001.

83. Saltiel, A.R., and Kahn, C.R. (2001). Insulin signalling and the regulation of glucose and lipid metabolism. Nature *414*, 799–806. 10.1038/414799a.

84. Metallo, C.M., and Vander Heiden, M.G. (2013). Understanding Metabolic Regulation and Its Influence on Cell Physiology. Molecular Cell *49*, 388–398. 10.1016/j.molcel.2013.01.018.

85. Ashe, K., Kelso, W., Farrand, S., Panetta, J., Fazio, T., Jong, G.D., and Walterfang, M. (2019). Psychiatric and Cognitive Aspects of Phenylketonuria: The Limitations of Diet and Promise of New Treatments. Frontiers in Psychiatry *10*. 10.3389/fpsyt.2019.00561.

86. Lake, N.J., Bird, M.J., Isohanni, P., and Paetau, A. (2015). Leigh syndrome: neuropathology and pathogenesis. J Neuropathol Exp Neurol *74*, 482–492. 10.1097/NEN.0000000000000195.

87. Reid, M.A., Dai, Z., and Locasale, J.W. (2017). The impact of cellular metabolism on chromatin dynamics and epigenetics. Nat Cell Biol *19*, 1298–1306. 10.1038/ncb3629.

88. Traxler, L., Lagerwall, J., Eichhorner, S., Stefanoni, D., D'Alessandro, A., and Mertens, J. (2021). Metabolism navigates neural cell fate in development, aging and neurodegeneration. Dis Model Mech *14*, dmm048993. 10.1242/dmm.048993.

89. Bauernfeind, A.L., Barks, S.K., Duka, T., Grossman, L.I., Hof, P.R., and Sherwood, C.C. (2014). Aerobic glycolysis in the primate brain: reconsidering the implications for growth and maintenance. Brain Struct Funct *219*, 1149–1167. 10.1007/s00429-013-0662-z.

90. Houten, S.M., Violante, S., Ventura, F.V., and Wanders, R.J.A. (2016). The Biochemistry and Physiology of Mitochondrial Fatty Acid β-Oxidation and Its Genetic Disorders. Annual Review of Physiology *78*, 23–44. 10.1146/annurev-physiol-021115-105045.

91. Islinger, M., Voelkl, A., Fahimi, H.D., and Schrader, M. (2018). The peroxisome: an update on mysteries 2.0. Histochem Cell Biol *150*, 443–471. 10.1007/s00418-018-1722-5.

92. Jo, D.S., Park, N.Y., and Cho, D.-H. (2020). Peroxisome quality control and dysregulated lipid metabolism in neurodegenerative diseases. Exp Mol Med *52*, 1486–1495. 10.1038/s12276-020-00503-9.

93. Braverman, N.E., D'Agostino, M.D., and MacLean, G.E. (2013). Peroxisome biogenesis disorders: Biological, clinical and pathophysiological perspectives. Developmental Disabilities Research Reviews *17*, 187–196. 10.1002/ddrr.1113.

94. Jo, D.S., and Cho, D.-H. (2019). Peroxisomal dysfunction in neurodegenerative diseases. Arch. Pharm. Res. *42*, 393–406. 10.1007/s12272-019-01131-2.

95. Ferdinandusse, S., Denis, S., Faust, P.L., and Wanders, R.J.A. (2009). Bile acids: the role of peroxisomes. Journal of Lipid Research *50*, 2139–2147. 10.1194/jlr.R900009-JLR200.

96. Hensley, C.T., Wasti, A.T., and DeBerardinis, R.J. (2013). Glutamine and cancer: cell biology, physiology, and clinical opportunities. J Clin Invest *123*, 3678–3684. 10.1172/JCI69600.

97. Fernstrom, J.D. (2005). Branched-Chain Amino Acids and Brain Function. The Journal of Nutrition *135*, S1539–S1546. 10.1093/jn/135.6.1539S.

98. Fernstrom, J.D. (2013). Large neutral amino acids: dietary effects on brain neurochemistry and function. Amino Acids *45*, 419–430. 10.1007/s00726-012-1330-y.

99. Polis, B., and Samson, A.O. (2020). Role of the metabolism of branched-chain amino acids in the development of Alzheimer's disease and other metabolic disorders. Neural Regeneration Research *15*, 1460. 10.4103/1673-5374.274328.

100. Martínez-Reyes, I., and Chandel, N.S. (2020). Mitochondrial TCA cycle metabolites control physiology and disease. Nat Commun *11*, 102. 10.1038/s41467-019-13668-3.

101. Deshpande, O.A., and Mohiuddin, S.S. (2022). Biochemistry, Oxidative Phosphorylation (StatPearls Publishing).

102. Rice, A.C., Zsoldos, R., Chen, T., Wilson, M.S., Alessandri, B., Hamm, R.J., and Bullock, M.R. (2002). Lactate administration attenuates cognitive deficits following traumatic brain injury. Brain Res *928*, 156–159. 10.1016/s0006-8993(01)03299-1.

103. Hayashi, T., Saito, A., Okuno, S., Ferrand-Drake, M., Dodd, R.L., and Chan, P.H. (2004). Oxidative injury to the endoplasmic reticulum in mouse brains after transient focal ischemia. Neurobiol Dis *15*, 229–239. 10.1016/j.nbd.2003.10.005.

104. Singh, A., Kukreti, R., Saso, L., and Kukreti, S. (2019). Oxidative Stress: A Key Modulator in Neurodegenerative Diseases. Molecules *24*, 1583. 10.3390/molecules24081583.

105. He, L., He, T., Farrar, S., Ji, L., Liu, T., and Ma, X. (2017). Antioxidants Maintain Cellular Redox Homeostasis by Elimination of Reactive Oxygen Species. Cell Physiol Biochem *44*, 532–553. 10.1159/000485089.

106. Rifes, P., Isaksson, M., Rathore, G.S., Aldrin-Kirk, P., Møller, O.K., Barzaghi, G., Lee, J., Egerod, K.L., Rausch, D.M., Parmar, M., et al. (2020). Modeling neural tube development by differentiation of human embryonic stem cells in a microfluidic WNT gradient. Nat Biotechnol *38*, 1265–1273. 10.1038/s41587-020-0525-0.

107. Candelario, K.M., Shuttleworth, C.W., and Cunningham, L.A. (2013). Neural stem/progenitor cells display a low requirement for oxidative metabolism independent of hypoxia inducible factor-1alpha expression. J Neurochem *125*, 420–429. 10.1111/jnc.12204.

108. Fitzner, D., Bader, J.M., Penkert, H., Bergner, C.G., Su, M., Weil, M.-T., Surma, M.A., Mann, M., Klose, C., and Simons, M. (2020). Cell-Type- and Brain-Region-Resolved Mouse Brain Lipidome. Cell Reports *32*. 10.1016/j.celrep.2020.108132.

109. Zheng, X., Boyer, L., Jin, M., Mertens, J., Kim, Y., Ma, L., Ma, L., Hamm, M., Gage, F.H., and Hunter, T. (2016). Metabolic reprogramming during neuronal differentiation from aerobic glycolysis to neuronal oxidative phosphorylation. Elife *5*, e13374. 10.7554/eLife.13374.

110. Folmes, C.D.L., Dzeja, P.P., Nelson, T.J., and Terzic, A. (2012). Metabolic Plasticity in Stem Cell Homeostasis and Differentiation. Cell Stem Cell *11*, 596–606. 10.1016/j.stem.2012.10.002.

111. Sá, J.V., Kleiderman, S., Brito, C., Sonnewald, U., Leist, M., Teixeira, A.P., and Alves, P.M. (2017). Quantification of Metabolic Rearrangements During Neural Stem Cells Differentiation into Astrocytes by Metabolic Flux Analysis. Neurochem Res *42*, 244–253. 10.1007/s11064-016-1907-z.

112. Stincone, A., Prigione, A., Cramer, T., Wamelink, M.M.C., Campbell, K., Cheung, E., Olin-Sandoval, V., Grüning, N.-M., Krüger, A., Tauqeer Alam, M., et al. (2015). The return of metabolism: biochemistry and physiology of the pentose phosphate pathway. Biological Reviews *90*, 927–963. 10.1111/brv.12140.

113. Lorenz, C., and Prigione, A. (2017). Mitochondrial metabolism in early neural fate and its relevance for neuronal disease modeling. Current Opinion in Cell Biology *49*, 71–76. 10.1016/j.ceb.2017.12.004.

114. Luo, S., Zhang, X., Yu, M., Yan, H., Liu, H., Wilson, J.X., and Huang, G. (2013). Folic Acid Acts Through DNA Methyltransferases to Induce the Differentiation of Neural Stem Cells into Neurons. Cell Biochem Biophys *66*, 559–566. 10.1007/s12013-012-9503-6.

115. Bélanger, M., Allaman, I., and Magistretti, P.J. (2011). Brain Energy Metabolism: Focus on Astrocyte-Neuron Metabolic Cooperation. Cell Metabolism *14*, 724–738. 10.1016/j.cmet.2011.08.016.

116. Alexandrov, Y.I., and Pletnikov, M.V. (2022). Neuronal metabolism in learning and memory: The anticipatory activity perspective. Neuroscience & Biobehavioral Reviews *137*, 104664. 10.1016/j.neubiorev.2022.104664.

117. Bordone, M.P., Salman, M.M., Titus, H.E., Amini, E., Andersen, J.V., Chakraborti, B., Diuba, A.V., Dubouskaya, T.G., Ehrke, E., Espindola de Freitas, A., et al. (2019). The energetic brain – A review from students to students. Journal of Neurochemistry *151*, 139–165. 10.1111/jnc.14829.

118. Hyder, F., Rothman, D.L., and Bennett, M.R. (2013). Cortical energy demands of signaling and nonsignaling components in brain are conserved across mammalian species and activity levels. Proceedings of the National Academy of Sciences *110*, 3549–3554. 10.1073/pnas.1214912110.

119. Lin, M.T., and Beal, M.F. (2006). Mitochondrial dysfunction and oxidative stress in neurodegenerative diseases. Nature *443*, 787–795. 10.1038/nature05292.

120. Schon, E.A., and Przedborski, S. (2011). Mitochondria: The Next (Neurode)Generation. Neuron *70*, 1033–1053. 10.1016/j.neuron.2011.06.003.

121. Koopman, W.J.H., Distelmaier, F., Smeitink, J.A., and Willems, P.H. (2013). OXPHOS mutations and neurodegeneration. The EMBO Journal *32*, 9–29. 10.1038/emboj.2012.300.

122. Islimye, E., Girard, V., and Gould, A.P. (2022). Functions of Stress-Induced Lipid Droplets in the Nervous System. Frontiers in Cell and Developmental Biology *10*.

123. Duran, J., Gruart, A., López-Ramos, J.C., Delgado-García, J.M., and Guinovart, J.J. (2019). Glycogen in Astrocytes and Neurons: Physiological and Pathological Aspects. Adv Neurobiol *23*, 311–329. 10.1007/978-3-030-27480-1_10.

124. Vilchez, D., Ros, S., Cifuentes, D., Pujadas, L., Vallès, J., García-Fojeda, B., Criado-García, O., Fernández-Sánchez, E., Medraño-Fernández, I., Domínguez, J., et al. (2007). Mechanism suppressing glycogen synthesis in neurons and its demise in progressive myoclonus epilepsy. Nat Neurosci *10*, 1407–1413. 10.1038/nn1998.

125. Almeida, A., Moncada, S., and Bolaños, J.P. (2004). Nitric oxide switches on glycolysis through the AMP protein kinase and 6-phosphofructo-2-kinase pathway. Nat Cell Biol *6*, 45–51. 10.1038/ncb1080.

126. Weightman Potter, P.G., Vlachaki Walker, J.M., Robb, J.L., Chilton, J.K., Williamson, R., Randall, A.D., Ellacott, K.L.J., and Beall, C. (2019). Basal fatty acid oxidation increases after recurrent low glucose in human primary astrocytes. Diabetologia *62*, 187–198. 10.1007/s00125-018-4744-6.

127. Walls, A.B., Waagepetersen, H.S., Bak, L.K., Schousboe, A., and Sonnewald, U. (2015). The Glutamine–Glutamate/GABA Cycle: Function, Regional Differences in Glutamate and GABA Production and Effects of Interference with GABA Metabolism. Neurochem Res *40*, 402–409. 10.1007/s11064-014-1473-1.

128. Matsuo, M., Campenot, R.B., Vance, D.E., Ueda, K., and Vance, J.E. (2011). Involvement of low-density lipoprotein receptor-related protein and ABCG1 in stimulation of axonal extension by apoE-containing lipoproteins. Biochimica et Biophysica Acta (BBA) - Molecular and Cell Biology of Lipids *1811*, 31–38. 10.1016/j.bbalip.2010.10.004.

129. Hayashi, H. (2011). Lipid Metabolism and Glial Lipoproteins in the Central Nervous System. Biological and Pharmaceutical Bulletin *34*, 453–461. 10.1248/bpb.34.453.

130. Hu, X., Yu, G., Liao, X., and Xiao, L. (2022). Interactions Between Astrocytes and Oligodendroglia in Myelin Development and Related Brain Diseases. Neurosci. Bull. 10.1007/s12264-022-00981-z.

131. Dimas, P., Montani, L., Pereira, J.A., Moreno, D., Trötzmüller, M., Gerber, J., Semenkovich, C.F., Köfeler, H.C., and Suter, U. (2019). CNS myelination and remyelination depend on fatty acid synthesis by oligodendrocytes. eLife *8*, e44702. 10.7554/eLife.44702.

132. Fünfschilling, U., Supplie, L.M., Mahad, D., Boretius, S., Saab, A.S., Edgar, J., Brinkmann, B.G., Kassmann, C.M., Tzvetanova, I.D., Möbius, W., et al. (2012). Glycolytic oligodendrocytes maintain myelin and long-term axonal integrity. Nature *485*, 517–521. 10.1038/nature11007.

133. Bernier, L.-P., York, E.M., Kamyabi, A., Choi, H.B., Weilinger, N.L., and MacVicar, B.A. (2020). Microglial metabolic flexibility supports immune surveillance of the brain parenchyma. Nat Commun *11*, 1559. 10.1038/s41467-020-15267-z.

134. Lauro, C., and Limatola, C. (2020). Metabolic Reprograming of Microglia in the Regulation of the Innate Inflammatory Response. Frontiers in Immunology *11*.

135. Choi, B.-H., and Coloff, J.L. (2019). The Diverse Functions of Non-Essential Amino Acids in Cancer. Cancers *11*, 675. 10.3390/cancers11050675.

136. Su, X., Wellen, K.E., and Rabinowitz, J.D. (2016). Metabolic control of methylation and acetylation. Curr Opin Chem Biol *30*, 52–60. 10.1016/j.cbpa.2015.10.030.

137. Dalangin, R., Kim, A., and Campbell, R.E. (2020). The Role of Amino Acids in Neurotransmission and Fluorescent Tools for Their Detection. Int J Mol Sci *21*, 6197. 10.3390/ijms21176197.

138. Stine, Z.E., Altman, B.J., Hsieh, A.L., Gouw, A.M., and Dang, C.V. (2014). Deregulation of the Cellular Energetics of Cancer Cells. In Pathobiology of Human Disease, L. M. McManus and R. N. Mitchell, eds. (Academic Press), pp. 444–455. 10.1016/B978-0-12-386456-7.01912-2.

139. Zaragozá, R. (2020). Transport of Amino Acids Across the Blood-Brain Barrier. Front Physiol *11*, 973. 10.3389/fphys.2020.00973.

140. Lieu, E.L., Nguyen, T., Rhyne, S., and Kim, J. (2020). Amino acids in cancer. Exp Mol Med *52*, 15–30. 10.1038/s12276-020-0375-3.

141. Albrecht, J., Sidoryk-Węgrzynowicz, M., Zielińska, M., and Aschner, M. (2010). Roles of glutamine in neurotransmission. Neuron Glia Biology *6*, 263–276. 10.1017/S1740925X11000093.

142. Wiesinger, H. (2001). Arginine metabolism and the synthesis of nitric oxide in the nervous system. Progress in Neurobiology *64*, 365–391. 10.1016/S0301-0082(00)00056-3.

143. Errasti-Murugarren, E., and Palacín, M. (2022). Heteromeric Amino Acid Transporters in Brain: from Physiology to Pathology. Neurochem Res *47*, 23–36. 10.1007/s11064-021-03261-w.

144. Brand, K. (1981). Metabolism of 2-oxoacid analogues of leucine, valine and phenylalanine by heart muscle, brain and kidney of the rat. Biochimica et Biophysica Acta (BBA) - General Subjects *677*, 126–132. 10.1016/0304-4165(81)90153-7.

145. Lane, M., and Gardner, D.K. (2005). Mitochondrial Malate-Aspartate Shuttle Regulates Mouse Embryo Nutrient Consumption*. Journal of Biological Chemistry *280*, 18361–18367. 10.1074/jbc.M500174200.

146. Moffatt, B.A., and Ashihara, H. (2002). Purine and Pyrimidine Nucleotide Synthesis and Metabolism. Arabidopsis Book *1*, e0018. 10.1199/tab.0018.

147. Chung, W.J., Lyons, S.A., Nelson, G.M., Hamza, H., Gladson, C.L., Gillespie, G.Y., and Sontheimer, H. (2005). Inhibition of cystine uptake disrupts the growth of primary brain tumors. J Neurosci *25*, 7101–7110. 10.1523/JNEUROSCI.5258-04.2005.

148. Lo, M., Ling, V., Wang, Y.Z., and Gout, P.W. (2008). The xc- cystine/glutamate antiporter: a mediator of pancreatic cancer growth with a role in drug resistance. Br J Cancer *99*, 464–472. 10.1038/sj.bjc.6604485.

149. Castagne, V., Gautschi, M., Lefevre, K., Posada, A., and Clarke, P.G.H. (1999). Relationships between neuronal death and the cellular redox status. Focus on the developing nervous system. Progress in Neurobiology *59*, 397–423. 10.1016/S0301-0082(99)00012-X.

150. Zhang, N. (2018). Role of methionine on epigenetic modification of DNA methylation and gene expression in animals. Animal Nutrition *4*, 11–16. 10.1016/j.aninu.2017.08.009.

151. Main, P.A., Angley, M.T., Thomas, P., O'Doherty, C.E., and Fenech, M. (2010). Folate and methionine metabolism in autism: a systematic review. The American Journal of Clinical Nutrition *91*, 1598–1620. 10.3945/ajcn.2009.29002.

152. Martínez, Y., Li, X., Liu, G., Bin, P., Yan, W., Más, D., Valdivié, M., Hu, C.-A.A., Ren, W., and Yin, Y. (2017). The role of methionine on metabolism, oxidative stress, and diseases. Amino Acids *49*, 2091–2098. 10.1007/s00726-017-2494-2.

153. Amelio, I., Cutruzzolá, F., Antonov, A., Agostini, M., and Melino, G. (2014). Serine and glycine metabolism in cancer. Trends in Biochemical Sciences *39*, 191–198. 10.1016/j.tibs.2014.02.004.

154. Pietrocola, F., Galluzzi, L., Bravo-San Pedro, J.M., Madeo, F., and Kroemer, G. (2015). Acetyl coenzyme A: a central metabolite and second messenger. Cell Metab *21*, 805–821. 10.1016/j.cmet.2015.05.014.

155. Bröer, S., and Palacín, M. (2011). The role of amino acid transporters in inherited and acquired diseases. Biochemical Journal *436*, 193–211. 10.1042/BJ20101912.

156. Fotiadis, D., Kanai, Y., and Palacín, M. (2013). The SLC3 and SLC7 families of amino acid transporters. Molecular Aspects of Medicine *34*, 139–158. 10.1016/j.mam.2012.10.007.

157. Closs, E.I., Boissel, J.-P., Habermeier, A., and Rotmann, A. (2006). Structure and Function of Cationic Amino Acid Transporters (CATs). J Membrane Biol *213*, 67–77. 10.1007/s00232-006-0875-7.

158. Jeckelmann, J.-M., Lemmin, T., Schlapschy, M., Skerra, A., and Fotiadis, D. (2022). Structure of the human heterodimeric transporter 4F2hc-LAT2 in complex with Anticalin, an alternative binding protein for applications in single-particle cryo-EM. Sci Rep *12*, 18269. 10.1038/s41598-022-23270-1.

159. Yan, R., Zhao, X., Lei, J., and Zhou, Q. (2019). Structure of the human LAT1–4F2hc heteromeric amino acid transporter complex. Nature *568*, 127–130. 10.1038/s41586-019-1011-z.

160. Fukasawa, Y., Segawa, H., Kim, J.Y., Chairoungdua, A., Kim, D.K., Matsuo, H., Cha, S.H., Endou, H., and Kanai, Y. (2000). Identification and Characterization of a Na+-independent Neutral Amino Acid Transporter That Associates with the 4F2 Heavy Chain and Exhibits Substrate Selectivity for Small Neutral d- and l-Amino Acids *. Journal of Biological Chemistry *275*, 9690–9698. 10.1074/jbc.275.13.9690.

161. Mastroberardino, L., Spindler, B., Pfeiffer, R., Skelly, P.J., Loffing, J., Shoemaker, C.B., and Verrey, F. (1998). Amino-acid transport by heterodimers of 4F2hc/CD98 and members of a permease family. Nature *395*, 288–291. 10.1038/26246.

162. Pfeiffer, R., Rossier, G., Spindler, B., Meier, C., Kühn, L., and Verrey, F. (1999). Amino acid transport of y+L-type by heterodimers of 4F2hc/CD98 and members of the glycoprotein-associated amino acid transporter family. The EMBO Journal *18*, 49–57. 10.1093/emboj/18.1.49.

163. Pineda, M., Fernández, E., Torrents, D., Estévez, R., López, C., Camps, M., Lloberas, J., Zorzano, A., and Palacın, M. (1999). Identification of a Membrane Protein, LAT-2, That Co-expresses with 4F2 Heavy Chain, an L-type Amino Acid Transport Activity with Broad Specificity for Small and Large Zwitterionic Amino Acids *. Journal of Biological Chemistry *274*, 19738–19744. 10.1074/jbc.274.28.19738.

164. Sato, H., Tamba, M., Ishii, T., and Bannai, S. (1999). Cloning and Expression of a Plasma Membrane Cystine/Glutamate Exchange Transporter Composed of Two Distinct Proteins *. Journal of Biological Chemistry *274*, 11455–11458. 10.1074/jbc.274.17.11455.

165. Torrents, D., Estévez, R., Pineda, M., Fernández, E., Lloberas, J., Shi, Y.-B., Zorzano, A., and Palacın, M. (1998). Identification and Characterization of a Membrane Protein (y+L Amino Acid Transporter-1) That Associates with 4F2hc to Encode the Amino Acid Transport Activity y+L: A CANDIDATE GENE FOR LYSINURIC PROTEIN INTOLERANCE *. Journal of Biological Chemistry *273*, 32437–32445. 10.1074/jbc.273.49.32437.

166. Scalise, M., Galluccio, M., Console, L., Pochini, L., and Indiveri, C. (2018). The Human SLC7A5 (LAT1): The Intriguing Histidine/Large Neutral Amino Acid Transporter and Its Relevance to Human Health. Frontiers in Chemistry *6*.

167. Ohgaki, R., Ohmori, T., Hara, S., Nakagomi, S., Kanai-Azuma, M., Kaneda-Nakashima, K., Okuda, S., Nagamori, S., and Kanai, Y. (2017). Essential Roles of L-Type Amino Acid Transporter 1 in Syncytiotrophoblast Development by Presenting Fusogenic 4F2hc. Molecular and Cellular Biology *37*, e00427-16. 10.1128/MCB.00427-16.

168. Bröer, S., and Bröer, A. (2017). Amino acid homeostasis and signalling in mammalian cells and organisms. Biochemical Journal *474*, 1935–1963. 10.1042/BCJ20160822.

169. Prasad, P.D., Wang, H., Huang, W., Kekuda, R., Rajan, D.P., Leibach, F.H., and Ganapathy, V. (1999). Human LAT1, a Subunit of System L Amino Acid Transporter: Molecular Cloning and Transport Function. Biochemical and Biophysical Research Communications *255*, 283–288. 10.1006/bbrc.1999.0206.

170. Verrey, F., Closs, E.I., Wagner, C.A., Palacin, M., Endou, H., and Kanai, Y. (2004). CATs and HATs: the SLC7 family of amino acid transporters. Pflugers Arch - Eur J Physiol *447*, 532–542. 10.1007/s00424-003-1086-z.

171. Duelli, R., Enerson, B.E., Gerhart, D.Z., and Drewes, L.R. (2000). Expression of Large Amino Acid Transporter LAT1 in Rat Brain Endothelium. J Cereb Blood Flow Metab *20*, 1557–1562. 10.1097/00004647-200011000-00005.

172. Milkereit, R., Persaud, A., Vanoaica, L., Guetg, A., Verrey, F., and Rotin, D. (2015). LAPTM4b recruits the LAT1-4F2hc Leu transporter to lysosomes and promotes mTORC1 activation. Nat Commun *6*, 7250. 10.1038/ncomms8250.

173. Nagatsu, T. (1995). Tyrosine hydroxylase: human isoforms, structure and regulation in physiology and pathology. Essays Biochem *30*, 15–35.

174. Fernstrom, J.D., and Fernstrom, M.H. (2007). Tyrosine, Phenylalanine, and Catecholamine Synthesis and Function in the Brain. The Journal of Nutrition *137*, 1539S-1547S. 10.1093/jn/137.6.1539S.

175. Silber, B.Y., and Schmitt, J.A.J. (2010). Effects of tryptophan loading on human cognition, mood, and sleep. Neuroscience & Biobehavioral Reviews *34*, 387–407. 10.1016/j.neubiorev.2009.08.005.

176. Finkelstein, J.D., Martin, J.J., and Harris, B.J. (1988). Methionine metabolism in mammals. The methionine-sparing effect of cystine. J Biol Chem *263*, 11750–11754.

177. MacKay, D.S., Brophy, J.D., McBreairty, L.E., McGowan, R.A., and Bertolo, R.F. (2012). Intrauterine growth restriction leads to changes in sulfur amino acid metabolism, but not global DNA methylation, in Yucatan miniature piglets. J Nutr Biochem *23*, 1121–1127. 10.1016/j.jnutbio.2011.06.005.

178. Yoshimatsu, H., Chiba, S., Tajima, D., Akehi, Y., and Sakata, T. (2002). Histidine Suppresses Food Intake through Its Conversion into Neuronal Histamine. Exp Biol Med (Maywood) *227*, 63–68. 10.1177/153537020222700111.

179. Yoshikawa, T., Nakamura, T., Shibakusa, T., Sugita, M., Naganuma, F., Iida, T., Miura, Y., Mohsen, A., Harada, R., and Yanai, K. (2014). Insufficient Intake of L-Histidine Reduces Brain Histamine and Causes Anxiety-Like Behaviors in Male Mice. The Journal of Nutrition *144*, 1637–1641. 10.3945/jn.114.196105.

180. Nakamura, T., Naganuma, F., Kudomi, U., Roh, S., Yanai, K., and Yoshikawa, T. (2022). Oral histidine intake improves working memory through the activation of histaminergic nervous system in mice. Biochemical and Biophysical Research Communications *609*, 141–148. 10.1016/j.bbrc.2022.04.016.

181. Takahara, T., Amemiya, Y., Sugiyama, R., Maki, M., and Shibata, H. (2020). Amino acid-dependent control of mTORC1 signaling: a variety of regulatory modes. Journal of Biomedical Science *27*, 87. 10.1186/s12929-020-00679-2.

182. Zhang, S., Lin, X., Hou, Q., Hu, Z., Wang, Y., and Wang, Z. (2021). Regulation of mTORC1 by amino acids in mammalian cells: A general picture of recent advances. Animal Nutrition *7*, 1009–1023. 10.1016/j.aninu.2021.05.003.

183. Hagenfeldt, L., and Arvidsson, A. (1980). The distribution of amino acids between plasma and erythrocytes. Clin Chim Acta *100*, 133–141. 10.1016/0009-8981(80)90074-1.

184. Sperringer, J.E., Addington, A., and Hutson, S.M. (2017). Branched-Chain Amino Acids and Brain Metabolism. Neurochem Res *42*, 1697–1709. 10.1007/s11064-017-2261-5.

185. White, P.J., McGarrah, R.W., Grimsrud, P.A., Tso, S.-C., Yang, W.-H., Haldeman, J.M., Grenier-Larouche, T., An, J., Lapworth, A.L., Astapova, I., et al. (2018). The BCKDH Kinase and Phosphatase Integrate BCAA and Lipid Metabolism via Regulation of ATP-Citrate Lyase. Cell Metabolism *27*, 1281-1293.e7. 10.1016/j.cmet.2018.04.015.

186. Hamilton, J.A., Hillard, C.J., Spector, A.A., and Watkins, P.A. (2007). Brain uptake and utilization of fatty acids, lipids and lipoproteins: application to neurological disorders. J Mol Neurosci *33*, 2– 11. 10.1007/s12031-007-0060-1.

187. Bruce, K.D., Zsombok, A., and Eckel, R.H. (2017). Lipid Processing in the Brain: A Key Regulator of Systemic Metabolism. Frontiers in Endocrinology *8*.

188. Cermenati, G., Mitro, N., Audano, M., Melcangi, R.C., Crestani, M., De Fabiani, E., and Caruso, D. (2015). Lipids in the nervous system: from biochemistry and molecular biology to patho-physiology. Biochim Biophys Acta *1851*, 51–60. 10.1016/j.bbalip.2014.08.011.

189. Bhaduri, A., Neumann, E.K., Kriegstein, A.R., and Sweedler, J.V. (2021). Identification of Lipid Heterogeneity and Diversity in the Developing Human Brain. JACS Au *1*, 2261–2270. 10.1021/jacsau.1c00393.

190. Hussain, G., Wang, J., Rasul, A., Anwar, H., Imran, A., Qasim, M., Zafar, S., Kamran, S.K.S., Razzaq, A., Aziz, N., et al. (2019). Role of cholesterol and sphingolipids in brain development and neurological diseases. Lipids in Health and Disease *18*, 26. 10.1186/s12944-019-0965-z.

191. Tillman, T.S., and Cascio, M. (2003). Effects of membrane lipids on ion channel structure and function. Cell Biochem Biophys *38*, 161–190. 10.1385/CBB:38:2:161.

192. Shevchenko, A., and Simons, K. (2010). Lipidomics: coming to grips with lipid diversity. Nat Rev Mol Cell Biol *11*, 593–598. 10.1038/nrm2934.

193. Holthuis, J.C.M., and Menon, A.K. (2014). Lipid landscapes and pipelines in membrane homeostasis. Nature *510*, 48–57. 10.1038/nature13474.

194. Boland, L.M., and Drzewiecki, M.M. (2008). Polyunsaturated Fatty Acid Modulation of Voltage-Gated Ion Channels. Cell Biochem Biophys *52*, 59–84. 10.1007/s12013-008-9027-2.

195. Park, E., and Rapoport, T.A. (2012). Mechanisms of Sec61/SecY-Mediated Protein Translocation Across Membranes. Annual Review of Biophysics *41*, 21–40. 10.1146/annurev-biophys-050511-102312.

196. Levine, T. (2004). Short-range intracellular trafficking of small molecules across endoplasmic reticulum junctions. Trends in Cell Biology *14*, 483–490. 10.1016/j.tcb.2004.07.017.

197. Mesmin, B., Bigay, J., Moser von Filseck, J., Lacas-Gervais, S., Drin, G., and Antonny, B. (2013). A four-step cycle driven by PI(4)P hydrolysis directs sterol/PI(4)P exchange by the ER-Golgi tether OSBP. Cell *155*, 830–843. 10.1016/j.cell.2013.09.056.

198. Sharpe, H.J., Stevens, T.J., and Munro, S. (2010). A comprehensive comparison of transmembrane domains reveals organelle-specific properties. Cell *142*, 158–169. 10.1016/j.cell.2010.05.037.

199. Bigay, J., and Antonny, B. (2012). Curvature, lipid packing, and electrostatics of membrane organelles: defining cellular territories in determining specificity. Dev Cell *23*, 886–895. 10.1016/j.devcel.2012.10.009.

200. Kihara, A. (2012). Very long-chain fatty acids: elongation, physiology and related disorders. The Journal of Biochemistry *152*, 387–395. 10.1093/jb/mvs105.

201. FRANK, C.L., DIERENFELD, E.S., and STOREY, K.B. (1998). The Relationship Between Lipid Peroxidation, Hibernation, and Food Selection in Mammals1. American Zoologist *38*, 341–349. 10.1093/icb/38.2.341.

202. Jakobsson, A., Westerberg, R., and Jacobsson, A. (2006). Fatty acid elongases in mammals: their regulation and roles in metabolism. Prog Lipid Res *45*, 237–249. 10.1016/j.plipres.2006.01.004.

203. Sinclair, A.J. (1975). Long-chain polyunsaturated fatty acids in the mammalian brain. Proc Nutr Soc *34*, 287–291. 10.1079/pns19750051.

204. Breckenridge, W.C., Gombos, G., and Morgan, I.G. (1972). The lipid composition of adult rat brain synaptosomal plasma membranes. Biochimica et Biophysica Acta (BBA) - Biomembranes *266*, 695–707. 10.1016/0005-2736(72)90365-3.

205. Sinclair, A.J. (1975). Incorporation of radioactive polyunsaturated fatty acids into liver and brain of developing rat. Lipids *10*, 175. 10.1007/BF02534156.

206. Ziegler, A.B., and Tavosanis, G. (2019). Glycerophospholipids – Emerging players in neuronal dendrite branching and outgrowth. Developmental Biology *451*, 25–34. 10.1016/j.ydbio.2018.12.009.

207. Svennerholm, L., Boström, K., Jungbjer, B., and Olsson, L. (1994). Membrane Lipids of Adult Human Brain: Lipid Composition of Frontal and Temporal Lobe in Subjects of Age 20 to 100 Years. Journal of Neurochemistry *63*, 1802–1811. 10.1046/j.1471-4159.1994.63051802.x.

208. Müller, C.P., Reichel, M., Mühle, C., Rhein, C., Gulbins, E., and Kornhuber, J. (2015). Brain membrane lipids in major depression and anxiety disorders. Biochimica et Biophysica Acta (BBA) - Molecular and Cell Biology of Lipids *1851*, 1052–1065. 10.1016/j.bbalip.2014.12.014.

209. Frisardi, V., Panza, F., Seripa, D., Farooqui, T., and Farooqui, A.A. (2011). Glycerophospholipids and glycerophospholipid-derived lipid mediators: A complex meshwork in Alzheimer's disease pathology. Progress in Lipid Research *50*, 313–330. 10.1016/j.plipres.2011.06.001.

210. Farooqui, A.A., Horrocks, L.A., and Farooqui, T. (2000). Glycerophospholipids in brain: their metabolism, incorporation into membranes, functions, and involvement in neurological disorders. Chemistry and Physics of Lipids *106*, 1–29. 10.1016/S0009-3084(00)00128-6.

211. Chan, R.B., Oliveira, T.G., Cortes, E.P., Honig, L.S., Duff, K.E., Small, S.A., Wenk, M.R., Shui, G., and Di Paolo, G. (2012). Comparative Lipidomic Analysis of Mouse and Human Brain with Alzheimer Disease*. Journal of Biological Chemistry *287*, 2678–2688. 10.1074/jbc.M111.274142.

212. Lamari, F., Mochel, F., Sedel, F., and Saudubray, J.M. (2013). Disorders of phospholipids, sphingolipids and fatty acids biosynthesis: toward a new category of inherited metabolic diseases. Journal of Inherited Metabolic Disease *36*, 411–425. 10.1007/s10545-012-9509-7.

213. Devaux, P.F. (1992). Protein Involvement in Transmembrane Lipid Asymmetry. Annual Review of Biophysics and Biomolecular Structure *21*, 417–439. 10.1146/annurev.bb.21.060192.002221.

214. Palsdottir, H., and Hunte, C. (2004). Lipids in membrane protein structures. Biochim Biophys Acta *1666*, 2–18. 10.1016/j.bbamem.2004.06.012.

215. Zhang, J., and Liu, Q. (2015). Cholesterol metabolism and homeostasis in the brain. Protein & Cell *6*, 254–264. 10.1007/s13238-014-0131-3.

216. Saher, G., Quintes, S., and Nave, K.-A. (2011). Cholesterol: a novel regulatory role in myelin formation. Neuroscientist *17*, 79–93. 10.1177/1073858410373835.

217. Segatto, M., Di Giovanni, A., Marino, M., and Pallottini, V. (2013). Analysis of the protein network of cholesterol homeostasis in different brain regions: an age and sex dependent perspective. J Cell Physiol *228*, 1561–1567. 10.1002/jcp.24315.

218. Ralhan, I., Chang, C.-L., Lippincott-Schwartz, J., and Ioannou, M.S. (2021). Lipid droplets in the nervous system. Journal of Cell Biology *220*, e202102136. 10.1083/jcb.202102136.

219. Cohen, S. (2018). Chapter Three - Lipid Droplets as Organelles. In International Review of Cell and Molecular Biology, L. Galluzzi, ed. (Academic Press), pp. 83–110. 10.1016/bs.ircmb.2017.12.007.

220. Olzmann, J.A., and Carvalho, P. (2019). Dynamics and functions of lipid droplets. Nat Rev Mol Cell Biol *20*, 137–155. 10.1038/s41580-018-0085-z.

221. Unger, R.H., and Orci, L. (2002). Lipoapoptosis: its mechanism and its diseases. Biochimica et Biophysica Acta (BBA) - Molecular and Cell Biology of Lipids *1585*, 202–212. 10.1016/S1388-1981(02)00342-6.

222. Listenberger, L.L., Han, X., Lewis, S.E., Cases, S., Farese, R.V., Ory, D.S., and Schaffer, J.E. (2003). Triglyceride accumulation protects against fatty acid-induced lipotoxicity. Proceedings of the National Academy of Sciences *100*, 3077–3082. 10.1073/pnas.0630588100.

223. Hariri, H., Rogers, S., Ugrankar, R., Liu, Y.L., Feathers, J.R., and Henne, W.M. (2018). Lipid droplet biogenesis is spatially coordinated at ER–vacuole contacts under nutritional stress. EMBO reports *19*, 57–72. 10.15252/embr.201744815.

224. Rambold, A.S., Kostelecky, B., Elia, N., and Lippincott-Schwartz, J. (2011). Tubular network formation protects mitochondria from autophagosomal degradation during nutrient starvation. Proceedings of the National Academy of Sciences *108*, 10190–10195. 10.1073/pnas.1107402108.

225. Young, R.M., Ackerman, D., Quinn, Z.L., Mancuso, A., Gruber, M., Liu, L., Giannoukos, D.N., Bobrovnikova-Marjon, E., Diehl, J.A., Keith, B., et al. (2013). Dysregulated mTORC1 renders cells critically dependent on desaturated lipids for survival under tumor-like stress. Genes Dev. *27*, 1115–1131. 10.1101/gad.198630.112.

226. Ackerman, D., Tumanov, S., Qiu, B., Michalopoulou, E., Spata, M., Azzam, A., Xie, H., Simon, M.C., and Kamphorst, J.J. (2018). Triglycerides Promote Lipid Homeostasis during Hypoxic Stress by Balancing Fatty Acid Saturation. Cell Reports *24*, 2596-2605.e5. 10.1016/j.celrep.2018.08.015.

227. Farooqui, A.A. (2009). Neural Membranes: A Pandora’s Box of Lipid Mediators. In Hot Topics in Neural Membrane Lipidology, A. A. Farooqui, ed. (Springer US), pp. 1–36. 10.1007/978-0-387-09693-3_1.

228. Lundbaek, J.A., and Andersen, O.S. (1994). Lysophospholipids modulate channel function by altering the mechanical properties of lipid bilayers. J Gen Physiol *104*, 645–673. 10.1085/jgp.104.4.645.

229. Bruno, M.J., Koeppe, R.E., and Andersen, O.S. (2007). Docosahexaenoic acid alters bilayer elastic properties. Proc Natl Acad Sci U S A *104*, 9638–9643. 10.1073/pnas.0701015104.

230. Perozo, E., Kloda, A., Cortes, D.M., and Martinac, B. (2002). Physical principles underlying the transduction of bilayer deformation forces during mechanosensitive channel gating. Nat Struct Biol *9*, 696–703. 10.1038/nsb827.

231. Di Paolo, G., and De Camilli, P. (2006). Phosphoinositides in cell regulation and membrane dynamics. Nature *443*, 651–657. 10.1038/nature05185.

232. Berridge, M.J., and Irvine, R.F. (1984). Inositol trisphosphate, a novel second messenger in cellular signal transduction. Nature *312*, 315–321. 10.1038/312315a0.

233. Harraz, O.F., Hill-Eubanks, D., and Nelson, M.T. (2020). PIP2: A critical regulator of vascular ion channels hiding in plain sight. Proceedings of the National Academy of Sciences *117*, 20378–20389. 10.1073/pnas.2006737117.

234. Hilgemann, D.W., Feng, S., and Nasuhoglu, C. (2001). The complex and intriguing lives of PIP2 with ion channels and transporters. Sci STKE *2001*, re19. 10.1126/stke.2001.111.re19.

235. Fiume, R., Faenza, I., Sheth, B., Poli, A., Vidalle, M.C., Mazzetti, C., Abdul, S.H., Campagnoli, F., Fabbrini, M., Kimber, S.T., et al. (2019). Nuclear Phosphoinositides: Their Regulation and Roles in Nuclear Functions. Int J Mol Sci *20*, 2991. 10.3390/ijms20122991.

236. Zhang, L., Mao, Y.S., Janmey, P.A., and Yin, H.L. (2012). Phosphatidylinositol 4, 5 bisphosphate and the actin cytoskeleton. Subcell Biochem *59*, 177–215. 10.1007/978-94-007-3015-1_6.

237. Bazan, N.G., Stark, D.T., and Petasis, N.A. (2012). Chapter 36 - Lipid Mediators: Eicosanoids, Docosanoids and Platelet-Activating Factor. In Basic Neurochemistry (Eighth Edition), S. T. Brady, G. J. Siegel, R. W. Albers, and D. L. Price, eds. (Academic Press), pp. 643–662. 10.1016/B978-0-12-374947-5.00036-5.

238. Schmitt, H., and Meves, H. (1995). Modulation of neuronal calcium channels by arachidonic acid and related substances. J. Membarin Biol. *145*, 233–244. 10.1007/BF00232715.

239. Chemin, J., Monteil, A., Perez-Reyes, E., Nargeot, J., and Lory, P. (2001). Direct inhibition of T-type calcium channels by the endogenous cannabinoid anandamide. EMBO J *20*, 7033–7040. 10.1093/emboj/20.24.7033.

240. Danthi, S.J., Enyeart, J.A., and Enyeart, J.J. (2005). Modulation of native T-type calcium channels by omega-3 fatty acids. Biochem Biophys Res Commun *327*, 485–493. 10.1016/j.bbrc.2004.12.033.

241. Xiao, Y.-F., Sigg, D.C., and Leaf, A. (2005). The Antiarrhythmic Effect of n-3 Polyunsaturated Fatty Acids: Modulation of Cardiac Ion Channels as a Potential Mechanism. J Membrane Biol *206*, 141–154. 10.1007/s00232-005-0786-z.

242. Leifert, W.R., McMurchie, E.J., and Saint, D.A. (1999). Inhibition of cardiac sodium currents in adult rat myocytes by n-3 polyunsaturated fatty acids. J Physiol *520*, 671–679. 10.1111/j.1469-7793.1999.00671.x.

243. Kang, J.X., and Leaf, A. (1996). Evidence that free polyunsaturated fatty acids modify Na+ channels by directly binding to the channel proteins. Proc Natl Acad Sci U S A *93*, 3542–3546.

244. Kang, J.X., Xiao, Y.F., and Leaf, A. (1995). Free, long-chain, polyunsaturated fatty acids reduce membrane electrical excitability in neonatal rat cardiac myocytes. Proc Natl Acad Sci U S A *92*, 3997–4001.

245. Jo, T., Iida, H., Kishida, S., Imuta, H., Oonuma, H., Nagata, T., Hara, H., Iwasawa, K., Soma, M., Sato, Y., et al. (2005). Acute and chronic effects of eicosapentaenoic acid on voltage-gated sodium channel expressed in cultured human bronchial smooth muscle cells. Biochemical and Biophysical Research Communications *331*, 1452–1459. 10.1016/j.bbrc.2005.04.062.

246. Doolan, G.K., Panchal, R.G., Fonnes, E.L., Clarke, A.L., Williams, D.A., and Petrou, S. (2002). Fatty acid augmentation of the cardiac slowly activating delayed rectifier current (IKs) is conferred by hminK. FASEB J *16*, 1662–1664. 10.1096/fj.02-0084fje.

247. Sade, H., Muraki, K., Ohya, S., Hatano, N., and Imaizumi, Y. (2006). Activation of large-conductance, Ca2+-activated K+ channels by cannabinoids. Am J Physiol Cell Physiol *290*, C77-86. 10.1152/ajpcell.00482.2004.

248. Wang, R., and Chen, Y.Q. (2022). Protein Lipidation Types: Current Strategies for Enrichment and Characterization. International Journal of Molecular Sciences *23*, 2365. 10.3390/ijms23042365.

249. Fukata, Y., and Fukata, M. (2010). Protein palmitoylation in neuronal development and synaptic plasticity. Nat Rev Neurosci *11*, 161–175. 10.1038/nrn2788.

250. Greaves, J., and Chamberlain, L.H. (2014). New links between S-acylation and cancer. The Journal of Pathology *233*, 4–6. 10.1002/path.4339.

251. Peng, T., Thinon, E., and Hang, H.C. (2016). Proteomic analysis of fatty-acylated proteins. Current Opinion in Chemical Biology *30*, 77–86. 10.1016/j.cbpa.2015.11.008.

252. Hannoush, R.N., and Sun, J. (2010). The chemical toolbox for monitoring protein fatty acylation and prenylation. Nat Chem Biol *6*, 498–506. 10.1038/nchembio.388.

253. Resh, M.D. (1999). Fatty acylation of proteins: new insights into membrane targeting of myristoylated and palmitoylated proteins. Biochim Biophys Acta *1451*, 1–16. 10.1016/s0167-4889(99)00075-0.

254. McCabe, J.B., and Berthiaume, L.G. (1999). Functional Roles for Fatty Acylated Amino-terminal Domains in Subcellular Localization. Mol Biol Cell *10*, 3771–3786.

255. Yalovsky, S., Rodr Guez-Concepción M, null, and Gruissem, W. (1999). Lipid modifications of proteins - slipping in and out of membranes. Trends Plant Sci *4*, 439–445. 10.1016/s1360-1385(99)01492-2.

256. Ji, B., and Skup, M. (2021). Roles of palmitoylation in structural long-term synaptic plasticity. Molecular Brain *14*, 8. 10.1186/s13041-020-00717-y.

257. Hannoush, R.N. (2015). Synthetic protein lipidation. Curr Opin Chem Biol *28*, 39–46. 10.1016/j.cbpa.2015.05.025.

258. Mumby, S.M. (1997). Reversible palmitoylation of signaling proteins. Curr Opin Cell Biol *9*, 148–154. 10.1016/s0955-0674(97)80056-7.

259. Milligan, G., Parenti, M., and Magee, A.I. (1995). The dynamic role of palmitoylation in signal transduction. Trends Biochem Sci *20*, 181–187. 10.1016/s0968-0004(00)89004-0.

260. Thomas, G.M., and Hayashi, T. (2013). Smarter neuronal signaling complexes from existing components: how regulatory modifications were acquired during animal evolution: evolution of palmitoylation-dependent regulation of AMPA-type ionotropic glutamate receptors. Bioessays *35*, 929–939. 10.1002/bies.201300076.

261. Globa, A.K., and Bamji, S.X. (2017). Protein palmitoylation in the development and plasticity of neuronal connections. Curr Opin Neurobiol *45*, 210–220. 10.1016/j.conb.2017.02.016.

262. Cassinelli, S., Viñola-Renart, C., Benavente-Garcia, A., Navarro-Pérez, M., Capera, J., and Felipe, A. (2022). Palmitoylation of Voltage-Gated Ion Channels. International Journal of Molecular Sciences *23*, 9357. 10.3390/ijms23169357.

263. Maday, S., Twelvetrees, A.E., Moughamian, A.J., and Holzbaur, E.L.F. (2014). Axonal transport: cargo-specific mechanisms of motility and regulation. Neuron *84*, 292–309. 10.1016/j.neuron.2014.10.019.

264. Holland, S.M., and Thomas, G.M. (2017). Roles of palmitoylation in axon growth, degeneration and regeneration. J Neurosci Res *95*, 1528–1539. 10.1002/jnr.24003.

265. Harrington, A.W., and Ginty, D.D. (2013). Long-distance retrograde neurotrophic factor signalling in neurons. Nat Rev Neurosci *14*, 177–187. 10.1038/nrn3253.

266. El-Husseini, A.E.-D., and Bredt, D.S. (2002). Protein palmitoylation: a regulator of neuronal development and function. Nat Rev Neurosci *3*, 791–802. 10.1038/nrn940.

267. Boumann, H.A., Gubbens, J., Koorengevel, M.C., Oh, C.-S., Martin, C.E., Heck, A.J.R., Patton-Vogt, J., Henry, S.A., de Kruijff, B., and de Kroon, A.I.P.M. (2006). Depletion of Phosphatidylcholine in Yeast Induces Shortening and Increased Saturation of the Lipid Acyl Chains: Evidence for Regulation of Intrinsic Membrane Curvature in a Eukaryote. Mol Biol Cell *17*, 1006–1017. 10.1091/mbc.E05-04-0344.

268. Kelleher, R.J., and Bear, M.F. (2008). The Autistic Neuron: Troubled Translation? Cell *135*, 401–406. 10.1016/j.cell.2008.10.017.

269. Zoghbi, H.Y., and Bear, M.F. (2012). Synaptic Dysfunction in Neurodevelopmental Disorders Associated with Autism and Intellectual Disabilities. Cold Spring Harb Perspect Biol *4*, a009886. 10.1101/cshperspect.a009886.

270. Cristino, A.S., Williams, S.M., Hawi, Z., An, J.-Y., Bellgrove, M.A., Schwartz, C.E., Costa, L. da F., and Claudianos, C. (2014). Neurodevelopmental and neuropsychiatric disorders represent an interconnected molecular system. Mol Psychiatry *19*, 294–301. 10.1038/mp.2013.16.

271. Leibovitz, Z., Lerman-Sagie, T., and Haddad, L. (2022). Fetal Brain Development: Regulating Processes and Related Malformations. Life (Basel) *12*, 809. 10.3390/life12060809.

272. Pirozzi, F., Nelson, B., and Mirzaa, G. (2018). From microcephaly to megalencephaly: determinants of brain size. Dialogues Clin Neurosci *20*, 267–282.

273. Juric-Sekhar, G., and Hevner, R.F. (2019). Malformations of Cerebral Cortex Development: Molecules and Mechanisms. Annu Rev Pathol *14*, 293–318. 10.1146/annurev-pathmechdis-012418-012927.

274. De Felice, A., Ricceri, L., Venerosi, A., Chiarotti, F., and Calamandrei, G. (2015). Multifactorial Origin of Neurodevelopmental Disorders: Approaches to Understanding Complex Etiologies. Toxics *3*, 89–129. 10.3390/toxics3010089.

275. Guerrini, R., and Dobyns, W.B. (2014). Malformations of cortical development: clinical features and genetic causes. Lancet Neurol *13*, 710–726. 10.1016/S1474-4422(14)70040-7.

276. Passemard, S., Kaindl, A.M., and Verloes, A. (2013). Chapter 13 - Microcephaly. In Handbook of Clinical Neurology Pediatric Neurology Part I., O. Dulac, M. Lassonde, and H. B. Sarnat, eds. (Elsevier), pp. 129–141. 10.1016/B978-0-444-52891-9.00013-0.

277. Kempińska, W., Korta, K., Marchaj, M., and Paprocka, J. (2022). Microcephaly in Neurometabolic Diseases. Children (Basel) *9*, 97. 10.3390/children9010097.

278. Seltzer, L.E., and Paciorkowski, A.R. (2014). Genetic disorders associated with postnatal microcephaly. Am J Med Genet C Semin Med Genet *166C*, 140–155. 10.1002/ajmg.c.31400.

279. Vahia, V.N. (2013). Diagnostic and statistical manual of mental disorders 5: A quick glance. Indian Journal of Psychiatry *55*, 220. 10.4103/0019-5545.117131.

280. Kanner, L. (1968). Autistic disturbances of affective contact. Acta Paedopsychiatr *35*, 100–136.

281. Moldin, S.O., and Rubenstein, J.L.R. (2006). Understanding Autism: From Basic Neuroscience to Treatment (CRC Press).

282. Sauer, A.K., Stanton, J.E., Hans, S., and Grabrucker, A.M. (2021). Autism Spectrum Disorders: Etiology and Pathology (Exon Publications) 10.36255/exonpublications.autismspectrumdisorders.2021.etiology.

283. Maenner, M.J., Shaw, K.A., Bakian, A.V., Bilder, D.A., Durkin, M.S., Esler, A., Furnier, S.M., Hallas, L., Hall-Lande, J., Hudson, A., et al. (2021). Prevalence and Characteristics of Autism Spectrum Disorder Among Children Aged 8 Years - Autism and Developmental Disabilities Monitoring Network, 11 Sites, United States, 2018. MMWR Surveill Summ *70*, 1–16. 10.15585/mmwr.ss7011a1.

284. Matson, J.L., and Shoemaker, M. (2009). Intellectual disability and its relationship to autism spectrum disorders. Res Dev Disabil *30*, 1107–1114. 10.1016/j.ridd.2009.06.003.

285. Canitano, R. (2007). Epilepsy in autism spectrum disorders. Eur Child Adolesc Psychiatry *16*, 61–66. 10.1007/s00787-006-0563-2.

286. Sahin, M., and Sur, M. (2015). Genes, circuits, and precision therapies for autism and related neurodevelopmental disorders. Science *350*, aab3897. 10.1126/science.aab3897.

287. Chang, B.S., and Lowenstein, D.H. (2003). Epilepsy. N Engl J Med *349*, 1257–1266. 10.1056/NEJMra022308.

288. Fisher, R.S., Acevedo, C., Arzimanoglou, A., Bogacz, A., Cross, J.H., Elger, C.E., Engel, J., Forsgren, L., French, J.A., Glynn, M., et al. (2014). ILAE official report: a practical clinical definition of epilepsy. Epilepsia *55*, 475–482. 10.1111/epi.12550.

289. Symonds, J.D., Zuberi, S.M., and Johnson, M.R. (2017). Advances in epilepsy gene discovery and implications for epilepsy diagnosis and treatment. 199. 10.1097/WCO.0000000000000433.

290. Sarmast, S.T., Abdullahi, A.M., and Jahan, N. Current Classification of Seizures and Epilepsies: Scope, Limitations and Recommendations for Future Action. Cureus *12*, e10549. 10.7759/cureus.10549.

291. World Health Organization (2019). Epilepsy: a public health imperative. Summary.

292. Löscher, W., Potschka, H., Sisodiya, S.M., and Vezzani, A. (2020). Drug Resistance in Epilepsy: Clinical Impact, Potential Mechanisms, and New Innovative Treatment Options. Pharmacol Rev *72*, 606–638. 10.1124/pr.120.019539.

293. Georgieff, M.K., Tran, P.V., and Carlson, E.S. (2018). Atypical fetal development: Fetal alcohol syndrome, nutritional deprivation, teratogens, and risk for neurodevelopmental disorders and psychopathology. Dev Psychopathol *30*, 1063–1086. 10.1017/S0954579418000500.

294. Parenti, I., Rabaneda, L.G., Schoen, H., and Novarino, G. (2020). Neurodevelopmental Disorders: From Genetics to Functional Pathways. Trends in Neurosciences *43*, 608–621. 10.1016/j.tins.2020.05.004.

295. Meredith, R.M. (2015). Sensitive and critical periods during neurotypical and aberrant neurodevelopment: A framework for neurodevelopmental disorders. Neuroscience & Biobehavioral Reviews *50*, 180–188. 10.1016/j.neubiorev.2014.12.001.

296. Dolgin, E. (2009). Human mutation rate revealed. Nature. 10.1038/news.2009.864.

297. Iossifov, I., Levy, D., Allen, J., Ye, K., Ronemus, M., Lee, Y., Yamrom, B., and Wigler, M. (2015). Low load for disruptive mutations in autism genes and their biased transmission. Proc Natl Acad Sci U S A *112*, E5600–E5607. 10.1073/pnas.1516376112.

298. Casanova, E.L., Gerstner, Z., Sharp, J.L., Casanova, M.F., and Feltus, F.A. (2018). Widespread Genotype-Phenotype Correlations in Intellectual Disability. Front Psychiatry *9*, 535. 10.3389/fpsyt.2018.00535.

299. Li, Y., Jia, X., Wu, H., Xun, G., Ou, J., Zhang, Q., Li, H., Bai, T., Hu, Z., Zou, X., et al. (2018). Genotype and phenotype correlations for SHANK3 de novo mutations in neurodevelopmental disorders. Am J Med Genet A *176*, 2668–2676. 10.1002/ajmg.a.40666.

300. Mullins, C., Fishell, G., and Tsien, R.W. (2016). Unifying Views of Autism Spectrum Disorders: A Consideration of Autoregulatory Feedback Loops. Neuron *89*, 1131–1156. 10.1016/j.neuron.2016.02.017.

301. Niemi, M.E.K., Martin, H.C., Rice, D.L., Gallone, G., Gordon, S., Kelemen, M., McAloney, K., McRae, J., Radford, E.J., Yu, S., et al. (2018). Common genetic variants contribute to risk of rare severe neurodevelopmental disorders. Nature *562*, 268–271. 10.1038/s41586-018-0566-4.

302. Mitra, I., Lavillaureix, A., Yeh, E., Traglia, M., Tsang, K., Bearden, C.E., Rauen, K.A., and Weiss, L.A. (2017). Reverse Pathway Genetic Approach Identifies Epistasis in Autism Spectrum Disorders. PLOS Genetics *13*, e1006516. 10.1371/journal.pgen.1006516.

303. El-Hattab, A.W., Adesina, A.M., Jones, J., and Scaglia, F. (2015). MELAS syndrome: Clinical manifestations, pathogenesis, and treatment options. Molecular Genetics and Metabolism *116*, 4–12. 10.1016/j.ymgme.2015.06.004.

304. Iannetti, E.F., Smeitink, J.A.M., Willems, P.H.G.M., Beyrath, J., and Koopman, W.J.H. (2018). Rescue from galactose-induced death of Leigh Syndrome patient cells by pyruvate and NAD. Cell Death Dis *9*, 1135. 10.1038/s41419-018-1179-4.

305. Galera-Monge, T., Zurita-Díaz, F., Canals, I., Hansen, M.G., Rufián-Vázquez, L., Ehinger, J.K., Elmér, E., Martin, M.A., Garesse, R., Ahlenius, H., et al. (2020). Mitochondrial Dysfunction and Calcium Dysregulation in Leigh Syndrome Induced Pluripotent Stem Cell Derived Neurons. Int J Mol Sci *21*, 3191. 10.3390/ijms21093191.

306. KARIMZADEH, P. (2015). Approach to Neurometabolic Diseases from a Pediatric Neurological Point of View. Iran J Child Neurol *9*, 1–16.

307. Strauss, K.A., Puffenberger, E.G., and Carson, V.J. (2020). Maple Syrup Urine Disease (University of Washington, Seattle).

308. Xu, J., Jakher, Y., and Ahrens-Nicklas, R.C. (2020). Brain Branched-Chain Amino Acids in Maple Syrup Urine Disease: Implications for Neurological Disorders. Int J Mol Sci *21*, 7490. 10.3390/ijms21207490.

309. Novarino, G., El-Fishawy, P., Kayserili, H., Meguid, N.A., Scott, E.M., Schroth, J., Silhavy, J.L., Kara, M., Khalil, R.O., Ben-Omran, T., et al. (2012). Mutations in BCKD-kinase Lead to a Potentially Treatable Form of Autism with Epilepsy. Science *338*, 394–397. 10.1126/science.1224631.

310. Tărlungeanu, D.C., Deliu, E., Dotter, C.P., Kara, M., Janiesch, P.C., Scalise, M., Galluccio, M., Tesulov, M., Morelli, E., Sonmez, F.M., et al. (2016). Impaired Amino Acid Transport at the Blood Brain Barrier Is a Cause of Autism Spectrum Disorder. Cell *167*, 1481-1494.e18. 10.1016/j.cell.2016.11.013.

311. Tangeraas, T., Constante, J.R., Backe, P.H., Oyarzábal, A., Neugebauer, J., Weinhold, N., Boemer, F., Debray, F.G., Ozturk-Hism, B., Evren, G., et al. (2023). BCKDK deficiency: a treatable neurodevelopmental disease amenable to newborn screening. Brain, awad010. 10.1093/brain/awad010.

312. MacDonald, A., Rocha, J.C., van Rijn, M., and Feillet, F. (2011). Nutrition in phenylketonuria. Molecular Genetics and Metabolism *104*, S10–S18. 10.1016/j.ymgme.2011.08.023.

313. Al Hafid, N., and Christodoulou, J. (2015). Phenylketonuria: a review of current and future treatments. Transl Pediatr *4*, 304–317. 10.3978/j.issn.2224-4336.2015.10.07.

314. van Vliet, D., van der Goot, E., Bruinenberg, V.M., van Faassen, M., de Blaauw, P., Kema, I.P., Heiner-Fokkema, M.R., van der Zee, E.A., and van Spronsen, F.J. (2018). Large neutral amino acid supplementation as an alternative to the phenylalanine-restricted diet in adults with phenylketonuria: evidence from adult Pah-enu2 mice. The Journal of Nutritional Biochemistry *53*, 20–27. 10.1016/j.jnutbio.2017.09.020.

315. Strauss, K.A., Carson, V.J., Soltys, K., Young, M.E., Bowser, L.E., Puffenberger, E.G., Brigatti, K.W., Williams, K.B., Robinson, D.L., Hendrickson, C., et al. (2020). Branched-chain α-ketoacid dehydrogenase deficiency (maple syrup urine disease): Treatment, biomarkers, and outcomes. Molecular Genetics and Metabolism *129*, 193–206. 10.1016/j.ymgme.2020.01.006.

316. Andersen, S.L. (2003). Trajectories of brain development: point of vulnerability or window of opportunity? Neurosci Biobehav Rev *27*, 3–18. 10.1016/s0149-7634(03)00005-8.

317. Jusko, T.A., Henderson, C.R., Lanphear, B.P., Cory-Slechta, D.A., Parsons, P.J., and Canfield, R.L. (2008). Blood Lead Concentrations < 10 μg/dL and Child Intelligence at 6 Years of Age. Environ Health Perspect *116*, 243–248. 10.1289/ehp.10424.

318. Oken, E., and Bellinger, D.C. (2008). Fish consumption, methylmercury and child neurodevelopment. Curr Opin Pediatr *20*, 178–183. 10.1097/MOP.0b013e3282f5614c.

319. Eskenazi, B., Marks, A.R., Bradman, A., Harley, K., Barr, D.B., Johnson, C., Morga, N., and Jewell, N.P. (2007). Organophosphate Pesticide Exposure and Neurodevelopment in Young Mexican-American Children. Environ Health Perspect *115*, 792–798. 10.1289/ehp.9828.

320. London, L., Beseler, C., Bouchard, M.F., Bellinger, D.C., Colosio, C., Grandjean, P., Harari, R., Kootbodien, T., Kromhout, H., Little, F., et al. (2012). Neurobehavioral and neurodevelopmental effects of pesticide exposures. Neurotoxicology *33*, 887–896. 10.1016/j.neuro.2012.01.004.

321. Perera, F.P., Li, Z., Whyatt, R., Hoepner, L., Wang, S., Camann, D., and Rauh, V. (2009). Prenatal airborne polycyclic aromatic hydrocarbon exposure and child IQ at age 5 years. Pediatrics *124*, e195-202. 10.1542/peds.2008-3506.

322. Whyatt, R.M., Liu, X., Rauh, V.A., Calafat, A.M., Just, A.C., Hoepner, L., Diaz, D., Quinn, J., Adibi, J., Perera, F.P., et al. (2012). Maternal prenatal urinary phthalate metabolite concentrations and child mental, psychomotor, and behavioral development at 3 years of age. Environ Health Perspect *120*, 290–295. 10.1289/ehp.1103705.

323. Rice, D.S., and Curran, T. (2001). Role of the reelin signaling pathway in central nervous system development. Annu Rev Neurosci *24*, 1005–1039. 10.1146/annurev.neuro.24.1.1005.

324. Maier, S.E., Miller, J.A., Blackwell, J.M., and West, J.R. (1999). Fetal alcohol exposure and temporal vulnerability: regional differences in cell loss as a function of the timing of binge-like alcohol exposure during brain development. Alcohol Clin Exp Res *23*, 726–734. 10.1111/j.1530-0277.1999.tb04176.x.

325. Portales-Casamar, E., Lussier, A.A., Jones, M.J., MacIsaac, J.L., Edgar, R.D., Mah, S.M., Barhdadi, A., Provost, S., Lemieux-Perreault, L.-P., Cynader, M.S., et al. (2016). DNA methylation signature of human fetal alcohol spectrum disorder. Epigenetics Chromatin *9*, 25. 10.1186/s13072-016-0074-4.

326. Chater-Diehl, E.J., Laufer, B.I., and Singh, S.M. (2017). Changes to histone modifications following prenatal alcohol exposure: An emerging picture. Alcohol *60*, 41–52. 10.1016/j.alcohol.2017.01.005.

327. Laufer, B.I., Mantha, K., Kleiber, M.L., Diehl, E.J., Addison, S.M.F., and Singh, S.M. (2013). Long-lasting alterations to DNA methylation and ncRNAs could underlie the effects of fetal alcohol exposure in mice. Dis Model Mech *6*, 977–992. 10.1242/dmm.010975.

328. Avchalumov, Y., and Mandyam, C.D. Synaptic Plasticity and its Modulation by Alcohol. Brain Plast *6*, 103–111. 10.3233/BPL-190089.

329. Davies, M. (2003). The role of GABAA receptors in mediating the effects of alcohol in the central nervous system. J Psychiatry Neurosci *28*, 263–274.

330. Lebedeva, J., Zakharov, A., Ogievetsky, E., Minlebaeva, A., Kurbanov, R., Gerasimova, E., Sitdikova, G., and Khazipov, R. (2017). Inhibition of Cortical Activity and Apoptosis Caused by Ethanol in Neonatal Rats In Vivo. Cerebral Cortex *27*, 1068–1082. 10.1093/cercor/bhv293.

331. Olney, J.W., Wozniak, D.F., Jevtovic-Todorovic, V., Farber, N.B., Bittigau, P., and Ikonomidou, C. (2002). Drug-induced Apoptotic Neurodegeneration in the Developing Brain. Brain Pathology *12*, 488–498. 10.1111/j.1750-3639.2002.tb00467.x.

332. Ikonomidou, C., and Turski, C. (2012). Neuropathological Sequelae of Developmental Exposure to Antiepileptic and Anesthetic Drugs. Frontiers in Neurology *3*.

333. Creeley, C.E. (2016). From Drug-Induced Developmental Neuroapoptosis to Pediatric Anesthetic Neurotoxicity-Where Are We Now? Brain Sci *6*, 32. 10.3390/brainsci6030032.

334. Bittigau, P., Sifringer, M., and Ikonomidou, C. (2003). Antiepileptic Drugs and Apoptosis in the Developing Brain. Annals of the New York Academy of Sciences *993*, 103–114. 10.1111/j.1749-6632.2003.tb07517.x.

335. Jevtovic-Todorovic, V., Hartman, R.E., Izumi, Y., Benshoff, N.D., Dikranian, K., Zorumski, C.F., Olney, J.W., and Wozniak, D.F. (2003). Early Exposure to Common Anesthetic Agents Causes Widespread Neurodegeneration in the Developing Rat Brain and Persistent Learning Deficits. J Neurosci *23*, 876–882. 10.1523/JNEUROSCI.23-03-00876.2003.

336. Weber-Stadlbauer, U. (2017). Epigenetic and transgenerational mechanisms in infection-mediated neurodevelopmental disorders. Transl Psychiatry *7*, e1113–e1113. 10.1038/tp.2017.78.

337. Ahlfors, K., Ivarsson, S.A., and Bjerre, I. (1986). Microcephaly and congenital cytomegalovirus infection: a combined prospective and retrospective study of a Swedish infant population. Pediatrics *78*, 1058–1063.

338. von der Hagen, M., Pivarcsi, M., Liebe, J., von Bernuth, H., Didonato, N., Hennermann, J.B., Bührer, C., Wieczorek, D., and Kaindl, A.M. (2014). Diagnostic approach to microcephaly in childhood: a two-center study and review of the literature. Dev Med Child Neurol *56*, 732–741. 10.1111/dmcn.12425.

339. Gérardin, P., Sampériz, S., Ramful, D., Boumahni, B., Bintner, M., Alessandri, J.-L., Carbonnier, M., Tiran-Rajaoefera, I., Beullier, G., Boya, I., et al. (2014). Neurocognitive Outcome of Children Exposed to Perinatal Mother-to-Child Chikungunya Virus Infection: The CHIMERE Cohort Study on Reunion Island. PLoS Negl Trop Dis *8*, e2996. 10.1371/journal.pntd.0002996.

340. O'Leary, D.R., Kuhn, S., Kniss, K.L., Hinckley, A.F., Rasmussen, S.A., Pape, W.J., Kightlinger, L.K., Beecham, B.D., Miller, T.K., Neitzel, D.F., et al. (2006). Birth outcomes following West Nile Virus infection of pregnant women in the United States: 2003-2004. Pediatrics *117*, e537-545. 10.1542/peds.2005-2024.

341. Faizan, M.I., Abdullah, M., Ali, S., Naqvi, I.H., Ahmed, A., and Parveen, S. (2016). Zika Virus-Induced Microcephaly and Its Possible Molecular Mechanism. Intervirology *59*, 152–158. 10.1159/000452950.

342. Cauchemez, S., Besnard, M., Bompard, P., Dub, T., Guillemette-Artur, P., Eyrolle-Guignot, D., Salje, H., Van Kerkhove, M.D., Abadie, V., Garel, C., et al. (2016). Association between Zika virus and microcephaly in French Polynesia, 2013-15: a retrospective study. Lancet *387*, 2125–2132. 10.1016/S0140-6736(16)00651-6.

343. Cortés-Albornoz, M.C., García-Guáqueta, D.P., Velez-van-Meerbeke, A., and Talero-Gutiérrez, C. (2021). Maternal Nutrition and Neurodevelopment: A Scoping Review. Nutrients *13*, 3530. 10.3390/nu13103530.

344. Galler, J.R., Bringas-Vega, M.L., Tang, Q., Rabinowitz, A.G., Musa, K.I., Chai, W.J., Omar, H., Abdul Rahman, M.R., Abd Hamid, A.I., Abdullah, J.M., et al. (2021). Neurodevelopmental effects of childhood malnutrition: A neuroimaging perspective. Neuroimage *231*, 117828. 10.1016/j.neuroimage.2021.117828.

345. Monk, C., Georgieff, M.K., and Osterholm, E.A. (2013). Research review: maternal prenatal distress and poor nutrition - mutually influencing risk factors affecting infant neurocognitive development. J Child Psychol Psychiatry *54*, 115–130. 10.1111/jcpp.12000.

346. Ho, A., Flynn, A.C., and Pasupathy, D. (2016). Nutrition in pregnancy. Obstetrics, Gynaecology and Reproductive Medicine *26*, 259–264. 10.1016/j.ogrm.2016.06.005.

347. DeCapo, M., Thompson, J.R., Dunn, G., and Sullivan, E.L. (2019). Perinatal Nutrition and Programmed Risk for Neuropsychiatric Disorders: A Focus on Animal Models. Biological Psychiatry *85*, 122–134. 10.1016/j.biopsych.2018.08.006.

348. Tarui, T., Rasool, A., and O'Tierney-Ginn, P. (2022). How the placenta-brain lipid axis impacts the nutritional origin of child neurodevelopmental disorders: Focus on attention deficit hyperactivity disorder and autism spectrum disorder. Experimental Neurology *347*, 113910. 10.1016/j.expneurol.2021.113910.

349. Richardson, A.J., and Ross, M.A. (2000). Fatty acid metabolism in neurodevelopmental disorder: a new perspective on associations between attention-deficit/hyperactivity disorder, dyslexia, dyspraxia and the autistic spectrum. Prostaglandins, Leukotrienes and Essential Fatty Acids (PLEFA) *63*, 1–9. 10.1054/plef.2000.0184.

350. Tamiji, J., and Crawford, D.A. (2010). The neurobiology of lipid metabolism in autism spectrum disorders. Neurosignals *18*, 98–112. 10.1159/000323189.

351. Li, M., Francis, E., Hinkle, S.N., Ajjarapu, A.S., and Zhang, C. (2019). Preconception and Prenatal Nutrition and Neurodevelopmental Disorders: A Systematic Review and Meta-Analysis. Nutrients *11*, 1628. 10.3390/nu11071628.

352. Hadders-Algra, M. (2011). Prenatal and early postnatal supplementation with long-chain polyunsaturated fatty acids: neurodevelopmental considerations. The American Journal of Clinical Nutrition *94*, S1874–S1879. 10.3945/ajcn.110.001065.

353. Martins, B.P., Bandarra, N.M., and Figueiredo-Braga, M. (2020). The role of marine omega-3 in human neurodevelopment, including Autism Spectrum Disorders and Attention-Deficit/Hyperactivity Disorder - a review. Crit Rev Food Sci Nutr *60*, 1431–1446. 10.1080/10408398.2019.1573800.

354. Simon, P., Dupuis, R., and Costentin, J. (1994). Thigmotaxis as an index of anxiety in mice. Influence of dopaminergic transmissions. Behavioural Brain Research *61*, 59–64. 10.1016/0166-4328(94)90008-6.

355. Caspi, A., and Moffitt, T.E. (2006). Gene–environment interactions in psychiatry: joining forces with neuroscience. Nat Rev Neurosci *7*, 583–590. 10.1038/nrn1925.

356. Uher, R. (2014). Gene–Environment Interactions in Severe Mental Illness. Frontiers in Psychiatry *5*.

357. Halldorsdottir, T., and Binder, E.B. (2017). Gene × Environment Interactions: From Molecular Mechanisms to Behavior. Annual Review of Psychology *68*, 215–241. 10.1146/annurev-psych-010416-044053.

358. Fries, G.R., and Walss-Bass, C. (2018). Chapter 4 - Gene-environment interactions in high-risk populations. In Bipolar Disorder Vulnerability, J. C. Soares, C. Walss-Bass, and P. Brambilla, eds. (Academic Press), pp. 49–68. 10.1016/B978-0-12-812347-8.00004-X.

359. Rock, K.D., and Patisaul, H.B. (2018). Environmental Mechanisms of Neurodevelopmental Toxicity. Curr Environ Health Rep *5*, 145–157. 10.1007/s40572-018-0185-0.

360. Ross, E.J., Graham, D.L., Money, K.M., and Stanwood, G.D. (2015). Developmental Consequences of Fetal Exposure to Drugs: What We Know and What We Still Must Learn. Neuropsychopharmacology *40*, 61–87. 10.1038/npp.2014.147.

361. Stankovic, I.N., and Colak, D. (2022). Prenatal Drugs and Their Effects on the Developing Brain: Insights From Three-Dimensional Human Organoids. Frontiers in Neuroscience *16*.

362. Bond, A.M., Ming, G.-L., and Song, H. (2015). Adult Mammalian Neural Stem Cells and Neurogenesis: Five Decades Later. Cell Stem Cell *17*, 385–395. 10.1016/j.stem.2015.09.003.

363. Gorski, J.A., Talley, T., Qiu, M., Puelles, L., Rubenstein, J.L.R., and Jones, K.R. (2002). Cortical excitatory neurons and glia, but not GABAergic neurons, are produced in the Emx1-expressing lineage. J Neurosci *22*, 6309–6314. 20026564.

364. Napolitano, L., Scalise, M., Galluccio, M., Pochini, L., Albanese, L.M., and Indiveri, C. (2015). LAT1 is the transport competent unit of the LAT1/CD98 heterodimeric amino acid transporter. Int J Biochem Cell Biol *67*, 25–33. 10.1016/j.biocel.2015.08.004.

365. Ye, Z., Wang, S., Zhang, C., and Zhao, Y. (2020). Coordinated Modulation of Energy Metabolism and Inflammation by Branched-Chain Amino Acids and Fatty Acids. Frontiers in Endocrinology *11*.

366. Aon, M.A., Cortassa, S., and O'Rourke, B. (2010). Redox-optimized ROS balance: a unifying hypothesis. Biochim Biophys Acta *1797*, 865–877. 10.1016/j.bbabio.2010.02.016.

367. Murphy, M.P. (2009). How mitochondria produce reactive oxygen species. Biochem J *417*, 1–13. 10.1042/BJ20081386.

368. Robb, E.L., Hall, A.R., Prime, T.A., Eaton, S., Szibor, M., Viscomi, C., James, A.M., and Murphy, M.P. (2018). Control of mitochondrial superoxide production by reverse electron transport at complex I. J Biol Chem *293*, 9869–9879. 10.1074/jbc.RA118.003647.

369. Iurlaro, R., and Muñoz-Pinedo, C. (2016). Cell death induced by endoplasmic reticulum stress. FEBS J *283*, 2640–2652. 10.1111/febs.13598.

370. Nwadike, C., Williamson, L.E., Gallagher, L.E., Guan, J.-L., and Chan, E.Y.W. (2018). AMPK Inhibits ULK1-Dependent Autophagosome Formation and Lysosomal Acidification via Distinct Mechanisms. Molecular and Cellular Biology *38*, e00023-18. 10.1128/MCB.00023-18.

371. Riggs, A.C., Bernal-Mizrachi, E., Ohsugi, M., Wasson, J., Fatrai, S., Welling, C., Murray, J., Schmidt, R.E., Herrera, P.L., and Permutt, M.A. (2005). Mice conditionally lacking the Wolfram gene in pancreatic islet beta cells exhibit diabetes as a result of enhanced endoplasmic reticulum stress and apoptosis. Diabetologia *48*, 2313–2321. 10.1007/s00125-005-1947-4.

372. Wortel, I.M.N., van der Meer, L.T., Kilberg, M.S., and van Leeuwen, F.N. (2017). Surviving Stress: Modulation of ATF4-Mediated Stress Responses in Normal and Malignant Cells. Trends Endocrinol Metab *28*, 794–806. 10.1016/j.tem.2017.07.003.

373. Felber, J.-P., and Golay, A. (1995). Regulation of nutrient metabolism and energy expenditure. Metabolism *44*, 4–9. 10.1016/0026-0495(95)90201-5.

374. Foufelle, F., and Ferré, P. (2013). Mechanism of Storage and Synthesis of Fatty Acids and Triglycerides in White Adipocytes. In Physiology and Physiopathology of Adipose Tissue, J.-P. Bastard and B. Fève, eds. (Springer), pp. 101–121. 10.1007/978-2-8178-0343-2_8.

375. Alves-Bezerra, M., and Cohen, D.E. (2017). Triglyceride metabolism in the liver. Compr Physiol *8*, 1–8. 10.1002/cphy.c170012.

376. Xu, X., Hu, J., McGrath, B.C., and Cavener, D.R. (2013). GCN2 in the Brain Programs PPARγ2 and Triglyceride Storage in the Liver during Perinatal Development in Response to Maternal Dietary Fat. PLOS ONE *8*, e75917. 10.1371/journal.pone.0075917.

377. Jin, N., Chow, C.Y., Liu, L., Zolov, S.N., Bronson, R., Davisson, M., Petersen, J.L., Zhang, Y., Park, S., Duex, J.E., et al. (2008). VAC14 nucleates a protein complex essential for the acute interconversion of PI3P and PI(3,5)P(2) in yeast and mouse. EMBO J *27*, 3221–3234. 10.1038/emboj.2008.248.

378. Schulze, U., Vollenbröker, B., Braun, D.A., Van Le, T., Granado, D., Kremerskothen, J., Fränzel, B., Klosowski, R., Barth, J., Fufezan, C., et al. (2014). The Vac14-interaction Network Is Linked to Regulators of the Endolysosomal and Autophagic Pathway. Mol Cell Proteomics *13*, 1397–1411. 10.1074/mcp.M113.034108.

379. Ho, C.Y., Alghamdi, T.A., and Botelho, R.J. (2012). Phosphatidylinositol-3,5-Bisphosphate: No Longer the Poor PIP2. Traffic *13*, 1–8. 10.1111/j.1600-0854.2011.01246.x.

380. González-Casimiro, C.M., Merino, B., Casanueva-Álvarez, E., Postigo-Casado, T., Cámara-Torres, P., Fernández-Díaz, C.M., Leissring, M.A., Cózar-Castellano, I., and Perdomo, G. (2021). Modulation of Insulin Sensitivity by Insulin-Degrading Enzyme. Biomedicines *9*, 86. 10.3390/biomedicines9010086.

381. Tundo, G.R., Sbardella, D., Ciaccio, C., Grasso, G., Gioia, M., Coletta, A., Polticelli, F., Di Pierro, D., Milardi, D., Van Endert, P., et al. (2017). Multiple functions of insulin-degrading enzyme: a metabolic crosslight? Critical Reviews in Biochemistry and Molecular Biology *52*, 554–582. 10.1080/10409238.2017.1337707.

382. Leissring, M.A. (2021). Insulin-Degrading Enzyme: Paradoxes and Possibilities. Cells *10*, 2445. 10.3390/cells10092445.

383. Feral, C.C., Nishiya, N., Fenczik, C.A., Stuhlmann, H., Slepak, M., and Ginsberg, M.H. (2005). CD98hc (SLC3A2) mediates integrin signaling. Proc Natl Acad Sci U S A *102*, 355–360. 10.1073/pnas.0404852102.

384. Castilho, B.A., Shanmugam, R., Silva, R.C., Ramesh, R., Himme, B.M., and Sattlegger, E. (2014). Keeping the eIF2 alpha kinase Gcn2 in check. Biochimica et Biophysica Acta (BBA) - Molecular Cell Research *1843*, 1948–1968. 10.1016/j.bbamcr.2014.04.006.

385. Gold, L.T., and Masson, G.R. (2022). GCN2: roles in tumour development and progression. Biochem Soc Trans *50*, 737–745. 10.1042/BST20211252.

386. Wei, C., Lin, M., Jinjun, B., Su, F., Dan, C., Yan, C., Jie, Y., Jin, Z., Zi-Chun, H., and Wu, Y. (2015). Involvement of general control nonderepressible kinase 2 in cancer cell apoptosis by posttranslational mechanisms. Mol Biol Cell *26*, 1044–1057. 10.1091/mbc.E14-10-1438.

387. She, P., Bunpo, P., Cundiff, J.K., Wek, R.C., Harris, R.A., and Anthony, T.G. (2013). General Control Nonderepressible 2 (GCN2) Kinase Protects Oligodendrocytes and White Matter during Branched-chain Amino Acid Deficiency in Mice *. Journal of Biological Chemistry *288*, 31250–31260. 10.1074/jbc.M113.498469.

388. Young, S.G. (1990). Recent progress in understanding apolipoprotein B. Circulation *82*, 1574–1594. 10.1161/01.CIR.82.5.1574.

389. Contreras, X., Amberg, N., Davaatseren, A., Hansen, A.H., Sonntag, J., Andersen, L., Bernthaler, T., Streicher, C., Heger, A., Johnson, R.L., et al. (2021). A genome-wide library of MADM mice for single-cell genetic mosaic analysis. Cell Rep *35*, 109274. 10.1016/j.celrep.2021.109274.

390. Zong, H., Espinosa, J.S., Su, H.H., Muzumdar, M.D., and Luo, L. (2005). Mosaic analysis with double markers in mice. Cell *121*, 479–492. 10.1016/j.cell.2005.02.012.

391. Zheng, H., Liu, W., Anderson, L.Y., and Jiang, Q.-X. (2011). Lipid-dependent gating of a voltage-gated potassium channel. Nat Commun *2*, 250. 10.1038/ncomms1254.

392. Duncan, A.L., Song, W., and Sansom, M.S.P. (2020). Lipid-Dependent Regulation of Ion Channels and G Protein–Coupled Receptors: Insights from Structures and Simulations. Annual Review of Pharmacology and Toxicology *60*, 31–50. 10.1146/annurev-pharmtox-010919-023411.

393. Curran, J., and Mohler, P.J. (2015). Alternative Paradigms for Ion Channelopathies: Disorders of Ion Channel Membrane Trafficking and Posttranslational Modification. Annual Review of Physiology *77*, 505–524. 10.1146/annurev-physiol-021014-071838.

394. Resh, M.D. (2013). Covalent Lipid Modifications of Proteins. Curr Biol *23*, R431–R435. 10.1016/j.cub.2013.04.024.

395. Chen, B., Sun, Y., Niu, J., Jarugumilli, G.K., and Wu, X. (2018). Protein lipidation in cell signaling and diseases: function, regulation and therapeutic opportunities. Cell Chem Biol *25*, 817–831. 10.1016/j.chembiol.2018.05.003.

396. Fujiwara, Y., Kondo, H.X., Shirota, M., Kobayashi, M., Takeshita, K., Nakagawa, A., Okamura, Y., and Kinoshita, K. (2016). Structural basis for the membrane association of ankyrinG via palmitoylation. Sci Rep *6*, 23981. 10.1038/srep23981.

397. Kim, J., Wei, D.-S., and Hoffman, D.A. (2005). Kv4 potassium channel subunits control action potential repolarization and frequency-dependent broadening in rat hippocampal CA1 pyramidal neurones. J Physiol *569*, 41–57. 10.1113/jphysiol.2005.095042.

398. Tomasoni, R., Repetto, D., Morini, R., Elia, C., Gardoni, F., Di Luca, M., Turco, E., Defilippi, P., and Matteoli, M. (2013). SNAP-25 regulates spine formation through postsynaptic binding to p140Cap. Nat Commun *4*, 2136. 10.1038/ncomms3136.

399. MacDonald, P.E., Wang, G., Tsuk, S., Dodo, C., Kang, Y., Tang, L., Wheeler, M.B., Cattral, M.S., Lakey, J.R.T., Salapatek, A.M.F., et al. (2002). Synaptosome-associated protein of 25 kilodaltons modulates Kv2.1 voltage-dependent K(+) channels in neuroendocrine islet beta-cells through an interaction with the channel N terminus. Mol Endocrinol *16*, 2452–2461. 10.1210/me.2002-0058.

400. Vetter, P., Roth, A., and Häusser, M. (2001). Propagation of Action Potentials in Dendrites Depends on Dendritic Morphology. Journal of Neurophysiology *85*, 926–937. 10.1152/jn.2001.85.2.926.

401. Kisanuki, Y.Y., Hammer, R.E., Miyazaki, J., Williams, S.C., Richardson, J.A., and Yanagisawa, M. (2001). Tie2-Cre transgenic mice: a new model for endothelial cell-lineage analysis in vivo. Dev Biol *230*, 230–242. 10.1006/dbio.2000.0106.

402. Sinclair, L.V., Rolf, J., Emslie, E., Shi, Y.-B., Taylor, P.M., and Cantrell, D.A. (2013). Control of amino-acid transport by antigen receptors coordinates the metabolic reprogramming essential for T cell differentiation. Nat Immunol *14*, 500–508. 10.1038/ni.2556.

403. Richards, S., Aziz, N., Bale, S., Bick, D., Das, S., Gastier-Foster, J., Grody, W.W., Hegde, M., Lyon, E., Spector, E., et al. (2015). Standards and guidelines for the interpretation of sequence variants: a joint consensus recommendation of the American College of Medical Genetics and Genomics and the Association for Molecular Pathology. Genet Med *17*, 405–423. 10.1038/gim.2015.30.

404. Schneider, C.A., Rasband, W.S., and Eliceiri, K.W. (2012). NIH Image to ImageJ: 25 years of image analysis. Nat Methods *9*, 671–675. 10.1038/nmeth.2089.

405. Wang, F., Flanagan, J., Su, N., Wang, L.-C., Bui, S., Nielson, A., Wu, X., Vo, H.-T., Ma, X.-J., and Luo, Y. (2012). RNAscope: a novel in situ RNA analysis platform for formalin-fixed, paraffin-embedded tissues. J Mol Diagn *14*, 22–29. 10.1016/j.jmoldx.2011.08.002.

406. Dieterle, F., Ross, A., Schlotterbeck, G., and Senn, H. (2006). Probabilistic Quotient Normalization as Robust Method to Account for Dilution of Complex Biological Mixtures. Application in 1H NMR Metabonomics. Anal. Chem. *78*, 4281–4290. 10.1021/ac051632c.

407. McKinney, W. (2010). Data Structures for Statistical Computing in Python. Proceedings of the 9th Python in Science Conference, 56–61. 10.25080/Majora-92bf1922-00a.

408. Harris, C.R., Millman, K.J., van der Walt, S.J., Gommers, R., Virtanen, P., Cournapeau, D., Wieser, E., Taylor, J., Berg, S., Smith, N.J., et al. (2020). Array programming with NumPy. Nature *585*, 357–362. 10.1038/s41586-020-2649-2.

409. Seabold, S., and Perktold, J. (2010). Statsmodels: Econometric and Statistical Modeling with Python. Proceedings of the 9th Python in Science Conference, 92–96. 10.25080/Majora-92bf1922-011.

410. Tsugawa, H., Cajka, T., Kind, T., Ma, Y., Higgins, B., Ikeda, K., Kanazawa, M., VanderGheynst, J., Fiehn, O., and Arita, M. (2015). MS-DIAL: data-independent MS/MS deconvolution for comprehensive metabolome analysis. Nat Methods *12*, 523–526. 10.1038/nmeth.3393.

411. Drotleff, B., and Lämmerhofer, M. (2019). Guidelines for Selection of Internal Standard-Based Normalization Strategies in Untargeted Lipidomic Profiling by LC-HR-MS/MS. Anal. Chem. *91*, 9836–9843. 10.1021/acs.analchem.9b01505.

412. Lee, S.H., Valtschanoff, J.G., Kharazia, V.N., Weinberg, R., and Sheng, M. (2001). Biochemical and morphological characterization of an intracellular membrane compartment containing AMPA receptors. Neuropharmacology *41*, 680–692. 10.1016/s0028-3908(01)00124-1.

413. Tyanova, S., Temu, T., and Cox, J. (2016). The MaxQuant computational platform for mass spectrometry-based shotgun proteomics. Nat Protoc *11*, 2301–2319. 10.1038/nprot.2016.136.

414. Ritchie, M.E., Phipson, B., Wu, D., Hu, Y., Law, C.W., Shi, W., and Smyth, G.K. (2015). limma powers differential expression analyses for RNA-sequencing and microarray studies. Nucleic Acids Research *43*, e47. 10.1093/nar/gkv007.

415. Dobin, A., Davis, C.A., Schlesinger, F., Drenkow, J., Zaleski, C., Jha, S., Batut, P., Chaisson, M., and Gingeras, T.R. (2013). STAR: ultrafast universal RNA-seq aligner. Bioinformatics *29*, 15–21. 10.1093/bioinformatics/bts635.

416. Afgan, E., Baker, D., Batut, B., van den Beek, M., Bouvier, D., Čech, M., Chilton, J., Clements, D., Coraor, N., Grüning, B.A., et al. (2018). The Galaxy platform for accessible, reproducible and collaborative biomedical analyses: 2018 update. Nucleic Acids Research *46*, W537–W544. 10.1093/nar/gky379.

417. Love, M.I., Huber, W., and Anders, S. (2014). Moderated estimation of fold change and dispersion for RNA-seq data with DESeq2. Genome Biology *15*, 550. 10.1186/s13059-014-0550-8.

418. Falcon, S., and Gentleman, R. (2007). Using GOstats to test gene lists for GO term association. Bioinformatics *23*, 257–258. 10.1093/bioinformatics/btl567.

419. Waskom, M.L. (2021). seaborn: statistical data visualization. Journal of Open Source Software *6*, 3021. 10.21105/joss.03021.

420. Hunter, J.D. (2007). Matplotlib: A 2D Graphics Environment. Computing in Science & Engineering *9*, 90–95. 10.1109/MCSE.2007.55.

421. Pedregosa, F., Varoquaux, G., Gramfort, A., Michel, V., Thirion, B., Grisel, O., Blondel, M., Prettenhofer, P., Weiss, R., Dubourg, V., et al. (2011). Scikit-learn: Machine Learning in Python. J. Mach. Learn. Res. *12*, 2825–2830.

422. Virtanen, P., Gommers, R., Oliphant, T.E., Haberland, M., Reddy, T., Cournapeau, D., Burovski, E., Peterson, P., Weckesser, W., Bright, J., et al. (2020). SciPy 1.0: fundamental algorithms for scientific computing in Python. Nat Methods *17*, 261–272. 10.1038/s41592-019-0686-2.

423. Di Bella, D.J., Habibi, E., Stickels, R.R., Scalia, G., Brown, J., Yadollahpour, P., Yang, S.M., Abbate, C., Biancalani, T., Macosko, E.Z., et al. (2021). Molecular logic of cellular diversification in the mouse cerebral cortex. Nature *595*, 554–559. 10.1038/s41586-021-03670-5.

424. Yuan, W., Ma, S., Brown, J.R., Kim, K., Murek, V., Trastulla, L., Meissner, A., Lodato, S., Shetty, A.S., Levin, J.Z., et al. (2022). Temporally divergent regulatory mechanisms govern neuronal diversification and maturation in the mouse and marmoset neocortex. Nat Neurosci *25*, 1049–1058. 10.1038/s41593-022-01123-4.

425. Hao, Y., Hao, S., Andersen-Nissen, E., Mauck, W.M., Zheng, S., Butler, A., Lee, M.J., Wilk, A.J., Darby, C., Zager, M., et al. (2021). Integrated analysis of multimodal single-cell data. Cell *184*, 3573-3587.e29. 10.1016/j.cell.2021.04.048.

426. Wearne, S.L., Rodriguez, A., Ehlenberger, D.B., Rocher, A.B., Henderson, S.C., and Hof, P.R. (2005). New techniques for imaging, digitization and analysis of three-dimensional neural

morphology on multiple scales. Neuroscience *136*, 661–680. 10.1016/j.neuroscience.2005.05.053.

427. Moy, S.S., Nadler, J.J., Young, N.B., Perez, A., Holloway, L.P., Barbaro, R.P., Barbaro, J.R., Wilson, L.M., Threadgill, D.W., Lauder, J.M., et al. (2007). Mouse behavioral tasks relevant to autism: phenotypes of 10 inbred strains. Behav Brain Res *176*, 4–20. 10.1016/j.bbr.2006.07.030.

428. Carter, R.J., Morton, J., and Dunnett, S.B. (2001). Motor coordination and balance in rodents. Curr Protoc Neurosci *Chapter 8*, Unit 8.12. 10.1002/0471142301.ns0812s15.

429. Guyenet, S.J., Furrer, S.A., Damian, V.M., Baughan, T.D., La Spada, A.R., and Garden, G.A. (2010). A simple composite phenotype scoring system for evaluating mouse models of cerebellar ataxia. J Vis Exp, 1787. 10.3791/1787.

430. Nikolić, M., Gardner, H. a. R., and Tucker, K.L. (2013). Postnatal neuronal apoptosis in the cerebral cortex: physiological and pathophysiological mechanisms. Neuroscience *254*, 369–378. 10.1016/j.neuroscience.2013.09.035.

431. Schwahn, B.C., Van Spronsen, F.J., Belaidi, A.A., Bowhay, S., Christodoulou, J., Derks, T.G., Hennermann, J.B., Jameson, E., König, K., McGregor, T.L., et al. (2015). Efficacy and safety of cyclic pyranopterin monophosphate substitution in severe molybdenum cofactor deficiency type A: a prospective cohort study. The Lancet *386*, 1955–1963. 10.1016/S0140-6736(15)00124-5.

432. Frye, R.E., Sequeira, J.M., Quadros, E.V., James, S.J., and Rossignol, D.A. (2013). Cerebral folate receptor autoantibodies in autism spectrum disorder. Mol Psychiatry *18*, 369–381. 10.1038/mp.2011.175.

433. Tümer, Z., and Møller, L.B. (2010). Menkes disease. Eur J Hum Genet *18*, 511–518. 10.1038/ejhg.2009.187.

434. Klepper, J., Akman, C., Armeno, M., Auvin, S., Cervenka, M., Cross, H.J., De Giorgis, V., Della Marina, A., Engelstad, K., Heussinger, N., et al. (2020). Glut1 Deficiency Syndrome (Glut1DS): State of the art in 2020 and recommendations of the international Glut1DS study group. Epilepsia Open *5*, 354–365. 10.1002/epi4.12414.

435. Fitzgerald, E., Roberts, J., Tennant, D.A., Boardman, J.P., and Drake, A.J. (2021). Metabolic adaptations to hypoxia in the neonatal mouse forebrain can occur independently of the transporters SLC7A5 and SLC3A2. Sci Rep *11*, 9092. 10.1038/s41598-021-88757-9.

436. Onishi, Y., Hiraiwa, M., Kamada, H., Iezaki, T., Yamada, T., Kaneda, K., and Hinoi, E. (2019). Hypoxia affects Slc7a5 expression through HIF-2α in differentiated neuronal cells. FEBS Open Bio *9*, 241–247. 10.1002/2211-5463.12559.

437. Huch, A., Huch, R., Schneider, H., and Rooth, G. (1977). Continuous transcutaneous monitoring of fetal oxygen tension during labour. Br J Obstet Gynaecol *84 Suppl 1*, 1–39. 10.1111/j.1471-0528.1977.tb16231.x.

438. Forrest, M.P., Parnell, E., and Penzes, P. (2018). Dendritic structural plasticity and neuropsychiatric disease. Nat Rev Neurosci *19*, 215–234. 10.1038/nrn.2018.16.

439. Rangaraju, V., Lewis, T.L., Hirabayashi, Y., Bergami, M., Motori, E., Cartoni, R., Kwon, S.-K., and Courchet, J. (2019). Pleiotropic Mitochondria: The Influence of Mitochondria on Neuronal Development and Disease. J. Neurosci. *39*, 8200–8208. 10.1523/JNEUROSCI.1157-19.2019.

440. Oury, F., and Pierani, A. (2023). Transient perinatal metabolic shifts determine neuronal survival and functional circuit formation. Cell *186*, 1819–1821. 10.1016/j.cell.2023.03.027.

441. Bishop, C.A., Schulze, M.B., Klaus, S., and Weitkunat, K. (2020). The branched-chain amino acids valine and leucine have differential effects on hepatic lipid metabolism. FASEB J *34*, 9727–9739. 10.1096/fj.202000195R.

442. Wallace, M., Green, C.R., Roberts, L.S., Lee, Y.M., McCarville, J.L., Sanchez-Gurmaches, J., Meurs, N., Gengatharan, J.M., Hover, J.D., Phillips, S.A., et al. (2018). Enzyme promiscuity drives branched-chain fatty acid synthesis in adipose tissues. Nat Chem Biol *14*, 1021–1031. 10.1038/s41589-018-0132-2.

443. Crown, S.B., Marze, N., and Antoniewicz, M.R. (2015). Catabolism of Branched Chain Amino Acids Contributes Significantly to Synthesis of Odd-Chain and Even-Chain Fatty Acids in 3T3-L1 Adipocytes. PLOS ONE *10*, e0145850. 10.1371/journal.pone.0145850.

444. Rossmeislová, L., Gojda, J., and Smolková, K. (2021). Pancreatic cancer: branched-chain amino acids as putative key metabolic regulators? Cancer Metastasis Rev *40*, 1115–1139. 10.1007/s10555-021-10016-0.

445. Newgard, C.B. (2012). Interplay between Lipids and Branched-Chain Amino Acids in Development of Insulin Resistance. Cell Metabolism *15*, 606–614. 10.1016/j.cmet.2012.01.024.

446. Lerin, C., Goldfine, A.B., Boes, T., Liu, M., Kasif, S., Dreyfuss, J.M., De Sousa-Coelho, A.L., Daher, G., Manoli, I., Sysol, J.R., et al. (2016). Defects in muscle branched-chain amino acid oxidation contribute to impaired lipid metabolism. Molecular Metabolism *5*, 926–936. 10.1016/j.molmet.2016.08.001.

447. Schmidt, D., Jiang, Q.-X., and MacKinnon, R. (2006). Phospholipids and the origin of cationic gating charges in voltage sensors. Nature *444*, 775–779. 10.1038/nature05416.

448. Rowitch, D.H., and Kriegstein, A.R. (2010). Developmental genetics of vertebrate glial-cell specification. Nature *468*, 214–222. 10.1038/nature09611.

449. Stogsdill, J.A., Ramirez, J., Liu, D., Kim, Y.H., Baldwin, K.T., Enustun, E., Ejikeme, T., Ji, R.-R., and Eroglu, C. (2017). Astrocytic neuroligins control astrocyte morphogenesis and synaptogenesis. Nature *551*, 192–197. 10.1038/nature24638.

450. Bayraktar, O.A., Bartels, T., Holmqvist, S., Kleshchevnikov, V., Martirosyan, A., Polioudakis, D., Ben Haim, L., Young, A.M.H., Batiuk, M.Y., Prakash, K., et al. (2020). Astrocyte layers in the mammalian cerebral cortex revealed by a single-cell in situ transcriptomic map. Nat Neurosci *23*, 500–509. 10.1038/s41593-020-0602-1.

451. Vanweert, F., Schrauwen, P., and Phielix, E. (2022). Role of branched-chain amino acid metabolism in the pathogenesis of obesity and type 2 diabetes-related metabolic disturbances BCAA metabolism in type 2 diabetes. Nutr. Diabetes *12*, 1–13. 10.1038/s41387-022-00213-3.

452. Shin, A.C., Fasshauer, M., Filatova, N., Grundell, L.A., Zielinski, E., Zhou, J.-Y., Scherer, T., Lindtner, C., White, P.J., Lapworth, A.L., et al. (2014). Brain Insulin Lowers Circulating BCAA Levels by Inducing Hepatic BCAA Catabolism. Cell Metabolism *20*, 898–909. 10.1016/j.cmet.2014.09.003.